

Diese Dissertation haben begutachtet:

.....



DISSERTATION

Magnetic and Magnetoelastic Properties of Cobalt Ferrite

ausgeführt zum Zwecke der Erlangung des akademischen Grades eines
Doktors der technischen Wissenschaften unter der Leitung von

**Ao.Univ.Prof.i.R. Projektass. Univ.Prof. Dipl.-Ing. Dr.techn.
Roland Grössinger**

E138

Institut für Festkörperphysik

eingereicht an der Technischen Universität Wien

Fakultät für Physik

von

Dipl.-Ing. Martin Kriegisch

Matrikelnummer: 0027638

Schulstraße 9, 2103 Langenzersdorf

Wien, am 18. September 2012

Kurzfassung

Kobaltferrit (CoFe_2O_4) ist ein interessantes Material als Sensor und Aktuator aufgrund seiner hohen Korrosionsbeständigkeit, hohen Magnetostriktion (λ) und - im Vergleich zu auf seltenen Erden basierenden Sensoren - niedrigen Herstellungskosten. Darüber hinaus machen die hohe Magnetfeld-Sensitivität der Magnetostriktion ($d\lambda/dH$) und die hohe Empfindlichkeit der Magnetisierung auf externen Druck ($dB/d\sigma$) Kobaltferrit zu einem idealen Kandidaten für die industrielle Anwendung als Sensor und Aktuator.

Obwohl Kobaltferrit seit über sechzig Jahren untersucht wird, gibt es noch immer viele offene Fragen und Probleme. Eine sehr fundamentale Fragestellung, die in dieser Arbeit diskutiert wird, ist die Bestimmung der "echten" Magnetostriktionswerte bei Proben mit nicht vernachlässigbarer Remanenz. Zusätzlich hat Guillot (CNRS, Grenoble) 1988 einen Sprung in der magnetfeldabhängigen Magnetisierung entlang harten Magnetisierungsachse bei Kobaltferrit und Cadmium substituiertem Kobaltferrit gefunden. Dieser Sprung wurde durch "Spin-Flip" Verhalten erklärt, was aufgrund der geringen Feldstärke nicht überzeugend ist.

Daher wurde im Rahmen dieser Arbeit dieser Übergang mit Hilfe von Magnetisierungs- und Magnetostriktionsmessungen als Funktion von Temperatur und Magnetfeld untersucht. Wir haben herausgefunden, dass dieser Übergang als Magnetisierungsprozess erster Ordnung (FOMP) klassifiziert werden kann, der sehr oft in uniaxialen, hartmagnetischen Materialien wie $\text{Nd}_2\text{Fe}_{14}\text{B}$ oder PrCo_5 vorkommt. Hingegen wird in kubischen, auf $3d$ Elementen basierenden Materialien - wie Kobaltferrit - ein FOMP sehr selten beobachtet. Der dem FOMP zugrunde liegende Prozess ist ein Sprung des Magnetisierungsvektors über eine Energiebarriere, die durch magnetische Anisotropie verursacht wird. Dieser Sprung wird auch in der Magnetostriktion beobachtet, da diese von der Spin-Bahn-Kopplung verursacht wird. Daher wurde auch die magnetische Anisotropie als Funktion der Temperatur bestimmt und deren verschiedene Beiträge in Abhängigkeit der Temperatur analysiert. Zusammenfassend wurde eine sehr detaillierte und systematische Untersuchung der magnetischen und magnetostriktiven Eigenschaften von einkristallinem und vielkristallinem Kobaltferrit durchgeführt und diese Ergebnisse wurden mit Theorie und Literatur verglichen.

Abstract

Cobalt ferrite (CoFe_2O_4) is interesting as magnetostrictive sensor and actuator material because of a high corrosion resistance, a high value of magnetostriction (λ) and very low costs compared to rare-earth based magnetostrictive sensor materials. Moreover the large strain derivative ($d\lambda/dH$) and the high sensitivity of magnetization to applied stress ($dB/d\sigma$) make it a perfect candidate for industrial applications as sensor and actuator.

Although cobalt ferrite is under examination for more than sixty years, there are still quite a lot of open questions and problems. One very fundamental problem is the determination of the “true” magnetostriction value of a material with a non negligible remanence which will be discussed here. Additionally in 1988 Guillot (CNRS, Grenoble) observed a jump in the field dependence of the magnetization along the magnetic hard axis in pure cobalt ferrite and also cadmium substituted cobalt ferrite. This jump was explained as a spin-flip. Because of the rather low critical field this explanation was not conclusive.

Therefore within this work this transition was studied by measuring the magnetization as well as the magnetostriction as function of temperature and applied magnetic field. We found out that this transition can be classified as a first order magnetization process (FOMP), which is quite often observed for uniaxial, hard magnetic materials like compounds for permanent magnets $\text{Nd}_2\text{Fe}_{14}\text{B}$ or PrCo_5 . Whereas in cubic $3d$ based materials - as cobalt ferrite - a FOMP is not very often seen. The underlying process of a FOMP is a jump of the magnetization vector over an energy barrier caused by the magnetic anisotropy energy. This jump is also clearly visible in the magnetic field dependence of the magnetostriction due to spin orbit coupling. In the case of cobalt ferrite we measured the change of the magnetic anisotropy as function of temperature and analyzed the effect of different anisotropy contributions with respect to their temperature dependence.

Summarizing, a very concise study of the magnetic and magnetostrictive properties of single- as well as polycrystalline cobalt ferrites was performed and compared with theory and literature.

Acknowledgement

I would like to give my most sincere thanks to my advisors Prof. Dr. Roland Grössinger and Dr. Reiko Sato-Turtelli for their guidance and support in preparing and executing this work. Without their inspiring advice and constant encouragement, this work would not have been possible.

I am indebted to Prof. Dr. Michael Zehetbauer for his support and help as FWF-NFN project leader.

I want to thank the whole Institute of Solid State Physics E138 for their continuous help and assistance.

I am indebted to Amtsdirektor Andreas Lahner and his workshop team of the institute E138 for their quick help and technical assistance.

I am thankful to Prof. Dr. Frank Kubel and Dipl.-Ing. Mariana Pantazi for their support and help in measuring and evaluating our XRD data.

The TEM study was performed with the help of Dr. Inga Ennen, Dr. Michael Stöger-Pollach and Dipl.-Ing. Andreas Steiger-Thirsfeld from USTEM at the Vienna University of Technology.

The financial support of the FWF-projects S10406 and S10401 are gratefully acknowledged.

Finally, I want to thank my whole family and especially my wife for their constant support and help.

Contents

1	Introduction and State of the Art	1
1.1	Introduction	1
1.2	State of the Art	2
2	Magnetism	4
2.1	Measurement Methods	4
2.2	The Law of Approach to Saturation	5
2.3	Magnetism of Spinel Ferrites	12
3	Magnetic Anisotropy	17
3.1	Types of Anisotropy	17
3.2	Magnetocrystalline Anisotropy for the Cubic Case	18
3.3	First Order Magnetization Process in the Cubic Case	23
3.4	Anisotropy Measurement Techniques	32
4	Magnetostriction	35
4.1	Definition - the Cubic Case	35
4.2	Measurement Methods	39
4.3	Modelling	40

5	Sample Preparation and Analytics	45
5.1	Sample Preparation: $\text{Co}_{0.8}\text{Fe}_{2.2}\text{O}_4$ Single Crystal	45
5.2	Analytics of the $\text{Co}_{0.8}\text{Fe}_{2.2}\text{O}_4$ Single Crystal	46
5.3	Sample Preparation: $\text{Co}_{0.88}\text{Fe}_{2.12}\text{O}_4$ Polycrystalline Samples . .	52
5.4	Analytics of the $\text{Co}_{0.88}\text{Fe}_{2.12}\text{O}_4$ Polycrystalline Samples	52
6	Magnetic Properties of Cobalt Ferrite	55
6.1	Magnetic Properties	55
6.2	Magnetic Anisotropy	76
6.3	Magnetostriction	97
7	Conclusion	120
	Bibliography	123

Chapter 1

Introduction and State of the Art

1.1 Introduction

Ferrites like magnetite (Fe_3O_4) exist in nature as “magnetic” minerals. So they have already been used as a compass for a long time in history: from ancient China to ancient Greece and Rome until the present day¹, where a lot of ferrites are still used. Depending on the elements involved, the magnetic properties are altered from soft to hard magnetic. The general chemical sum formula for spinel ferrites is: MeFe_2O_4 , where Me stands for a (divalent or trivalent) metal ion of the group of the transition elements like Mn, Fe, Co, Ni, Cu, Zn, Mg or Cd [2]. When mixing the transition elements, the magnetic properties can be varied from soft to hard magnetic.

Among the group of spinel ferrites, cobalt ferrite (CoFe_2O_4) exhibits outstanding magnetic and magnetoelastic properties. Due to the presence of the Co^{2+} ions in the spinel lattice, magnetostriction increases together with magnetic anisotropy [2]. The increased magnetostriction favours cobalt ferrite as a sensor and actuator material, as the coupling of the magnetization to the magnetostriction leads to interesting physical effects: For example the Villari effect, which denotes the change of magnetization of the material when external stress is applied. For a more concise overview on the different magnetostriction effects see [2, 3, 4]. Cobalt ferrite is

¹For a more detailed historic introduction on magnetism see among others [1].

very interesting for modern research and technology because it is excellent material for sensors and actuators. Among all known magnetostrictive materials it has outstanding magneto-elastic properties, although it has no rare-earth elements in the sum formula. Its magneto-elastic properties rise mainly due to the presence of the Co^{2+} -ions, which are held responsible not only for the increased magnetostriction, but also for increased anisotropy.

1.2 State of the Art

This thesis mainly concentrates on cobalt ferrite and its magnetic and magnetoelastic properties. Although the first spinel ferrites were artificially synthesized quite early in 1909 [5], the magnetic measurement techniques and theories were not fully developed. Néel finally developed the theoretical hypothesis for describing the ferrimagnetism [6] in the end of the 1940ies, which was later confirmed by neutron diffraction [7]. With the theory of ferrimagnetism a proper magnetic description of the spinels was achieved, as all spinels are ordering ferrimagnetically.

The magnetic and magnetoelastic properties of cobalt ferrite were investigated in the 1950ies more precisely [8, 9]. Bozorth and coworkers investigated the magnetostriction and magnetic anisotropy of cobalt ferrite in 1955 [10]. This is probably the most cited paper on magnetostriction of cobalt ferrite. With the development of the vibrating sample magnetometer by S. Foner [11], the magnetization of cobalt ferrite was investigated more accurately [12].

The effect of field annealing in cobalt ferrite was found and investigated by various groups not only in polycrystalline [13, 14], but also in single crystalline cobalt ferrite [15, 16, 17]. When cobalt ferrite is heated a few hundred degrees Centigrade below the Curie-Temperature and a magnetic field is applied for some time, the sample exhibits a thermally stable, permanent, additional uniaxial anisotropy along the field annealing direction.

The magnetic anisotropy of cobalt ferrite was measured with various methods, like ferromagnetic resonance [18] or torque [10, 19, 20]. It was concluded

that the first order anisotropy constant K_1 plays the most important role, while higher order anisotropy constants were neglected.

The magnetostriction of single crystalline [9, 10, 21] and polycrystalline [22, 14] cobalt ferrite has been investigated by many groups. In fact magnetostriction of various doped cobalt ferrites is still being investigated today, as this kind of material is suitable as sensor and actuator material [23, 24, 25]. Besides its resistance to corrosion, cobalt ferrite is inexpensive and easy to produce, as no rare-earth elements are involved. By doping with different elements, one tries to reduce magnetic anisotropy while magnetostriction should stay constant.

The aim of this thesis is to understand the magneto-elastic behavior of cobalt ferrite. Therefore it presents magnetization, magnetic anisotropy and magnetostriction measurements on a set of polycrystalline samples and one single crystal over a broad temperature range. The key to understand the magnetostrictive behavior of cobalt ferrite lies in the second order magnetic anisotropy constant K_2 . As all samples exhibit a huge anisotropy, a large magnetic field is needed for magnetic saturation.

Looking at the problem from an historical view, large magnetic fields were not easy to produce. From the 1970ies on, cryostats with superconducting coils were found more often in research laboratories. Most of the magnetic properties of cobalt ferrite had already been investigated before that time and later nobody thought a re-investigation was necessary. In 1988 Guillot measured pure and Cd-doped cobalt-ferrite and found out that very high magnetic fields at low temperatures were necessary in order to saturate the samples [26]. No suitable explanation was supplied, which made it necessary to re-investigate and re-evaluate the theoretical description of the magnetic properties of cobalt ferrite. This thesis attempts to fill the gaps of previous research in the field.

Chapter 2

Magnetism

2.1 Measurement Methods

The magnetization measurements were performed in a vibrating sample magnetometer (VSM) commercially available from Quantum Design Inc. The design is based on the work of Simon Foner [11], although it was improved over the years [27]. The used VSM is built in an ^4He -cryostat with a high temperature option, yielding an extended temperature range of 1.9 to 1100 K with a maximum magnetic field H of ± 90 kOe. A set of reference samples (Ni, Fe, $\text{Co}_{0.8}\text{Fe}_{2.2}\text{O}_4$ and Fe_3O_4) was measured to test the thermometry in the high temperature range and to check the calibration of the pick-up system. The absolute error in temperature was found to be within the expected 2% error interval provided by Quantum Design Inc. No systematic deviations from the calibration of the pick-up system were found. The error in magnetization was found to be much smaller than 1%. For all evaluated magnetization data the (applied) external magnetic field was used. The (calculated) internal magnetic field was only used where it is explicitly noted. For evaluating the magnetization data the law of approach to saturation (LAS) was employed.

2.2 The Law of Approach to Saturation

The law of approach to saturation (LAS) describes the magnetization curve near saturation of a ferro-, ferri- or antiferromagnetic sample as function of the magnetic field. It is widely employed because of the simplicity of use and the easy gain of information on magnetic anisotropy and other internal material parameters like stress or structural defects. The LAS is mainly used for polycrystalline or amorphous materials, but under special circumstances it can be applied as well for single crystals (see chapter 6.1.1).

2.2.1 Definition

The law of approach to saturation is generally defined [3, 28] as a power series of the magnetic field H :

$$M(H) = M_{Sat} \left(1 + \frac{a}{H} + \frac{b}{H^2} + \frac{c}{H^3} + \frac{d}{\sqrt{H}} + e\sqrt{H} + fH + gH^2 \right) \quad (2.1)$$

where M_{Sat} and $a - g$ are all constants with different physical meanings. Generally spoken, the terms with positive exponent of the magnetic field H are related to the so-called paraprocess as the magnetization increases with increasing field [29]. Whereas the terms with negative exponent are referred to misalignment of the collective magnetization vector, as their contribution to the magnetization is getting smaller with increasing field. The origin of the effects are depending on the power of the term: magnetic anisotropy, structural defects, internal stress, boundary or surface effects and many more can be accounted for the deviation of the saturation magnetization value [30, 6]. A recent article [31] and the references therein provide an overview on the various parameters.

In this work the number of fit parameters is reduced in order to make the description of the magnetization $M(H)$ more facile. Therefore we restrict ourselves to the three most important variables. The law of approach to

saturation is then defined as [28]:

$$M(H) = M_{Sat} \left(1 - \frac{b}{H^2} \right) + \kappa H \quad (2.2)$$

where M_{Sat} is the saturation magnetization, b is a field independent magnetic anisotropy related constant and κ is the high-field susceptibility.

2.2.2 Physical Explanation of Variables

M_{Sat} - Saturation Magnetization

The saturation magnetization M_{Sat} denotes the maximum value of the magnetic moment the sample has at a certain temperature for $H = \infty$. The magnetization M can be seen as projection of the saturation magnetization vector to the direction of the applied field $M = M_{Sat} \cos \theta$, with θ as the angle between the applied magnetic field and the saturation magnetization vector (see figure 2.1). Many physical origins exist which prevent the magnetization from full saturation. For example the magnetic anisotropy or the thermal fluctuations hinder the magnetization value from reaching full saturation M_{Sat} .

$\frac{b}{H^2}$ - the anisotropy term

Akulov has published the derivation for relating the magnetocrystalline anisotropy with the constant b [32], as well as Becker and Döring [3]. Alternatively, a very elegant way of deriving the LAS is shown by [28]. When θ is denoting the angle between the magnetization vector M and the magnetic field H (see figure 2.1), the projection of the magnetization vector in the direction of the field is:

$$M = M_{Sat} \cos \theta = M_{Sat} \left(1 - \frac{\theta^2}{2} + \dots \right). \quad (2.3)$$

The exerted torque of the magnetic field L_H is counterbalanced by the torque created from the magnetic anisotropy L_A :

$$M_{Sat}H \sin \theta = -\frac{\partial E_A}{\partial \theta}, \quad (2.4)$$

where E_A is the magnetic anisotropy energy (for exact definition see chapter 3). When the material is near saturation, θ is very small and the sine function of formula 2.4 can be approximated with its argument:

$$\theta = -\frac{\left(\frac{\partial E_A}{\partial \theta}\right)_{\theta \ll}}{M_{Sat}H} = \frac{C}{M_{Sat}H}, \quad (2.5)$$

with $C = -\left(\frac{\partial E_A}{\partial \theta}\right)_{\theta \ll}$. By putting formula 2.5 into formula 2.3 we obtain:

$$M = M_{Sat} \left(1 - \frac{b}{H^2} - \dots\right), \quad (2.6)$$

where $b = \frac{C^2}{2M_{Sat}}$. As M is rotating along the maximum gradient of the anisotropy energy, C^2 can be written as:

$$C^2 = |\nabla E_A|^2 = \left(\frac{\partial E_A}{\partial \theta}\right)^2 + \frac{1}{\sin^2 \theta} \left(\frac{\partial E_A}{\partial \phi}\right)^2, \quad (2.7)$$

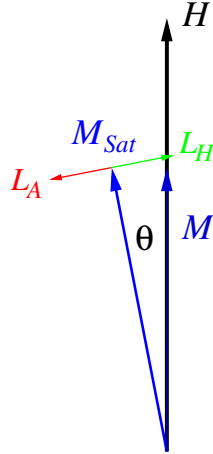


Figure 2.1: Rotation of the magnetization vector against the magnetic anisotropy (adapted from [28])

with θ and ϕ as the polar coordinates of the magnetization. For solving C for the cubic case, we have to define the cubic magnetic anisotropy energy (see formula 3.4) for the most simplest case:

$$E_A = K_1(\alpha_1\alpha_2 + \alpha_2\alpha_3 + \alpha_1\alpha_3), \quad (2.8)$$

where the α_i are the direction cosines of the magnetization:

$$\begin{aligned} \alpha_1 &= \sin \theta \cos \phi \\ \alpha_2 &= \sin \theta \sin \phi \\ \alpha_3 &= \cos \theta \end{aligned}$$

By putting E_A into formula 2.7 and averaging over all possible directions of the polycrystal, we finally obtain:

$$b = \frac{8}{105} \frac{K_1^2}{M_{Sat}^2}, \quad (2.9)$$

In the averaging process it was assumed that the polycrystalline sample is isotropic with no kind of any texture. This yields to the law of approach to saturation in its final form:

$$M(H) = M_{Sat} \left(1 - \frac{8}{105} \frac{K_1^2}{M_{Sat}^2 H^2} \right) + \kappa H. \quad (2.10)$$

κH - the high field susceptibility term

Although most softmagnetic samples seem to be fully saturated at a few hundreds of Oersted (see for example the magnetization of nickel in figure 4.3), the magnetization vector is slightly rotated out of the field direction at finite temperatures T due to magnetocrystalline anisotropy, magnetoelastic contributions, thermal excitation and the formation of spin waves [33]. As a consequence the magnetization value for finite fields is below the saturation value. Holstein and Primakoff specified the theoretical description in 1941 [29]. They discussed this “intrinsic susceptibility” on the basis of the exchange interaction model and described it with a linear relation of the

susceptibility at temperatures below the ordering temperature T_C :

$$\kappa = dM/dH = Ak_B T \quad (2.11)$$

with A as a temperature independent constant at a given field. This linear behaviour in temperature was verified for example by Polley for Nickel in the temperature range of 150 - 320 K [34]. Akulov is also describing this behaviour for ferromagnetic substances [32] and adds an important observation around the Curie-Temperature T_C : While the high field susceptibility κ is growing with temperature, it reaches a maximum around T_C and decreases with increasing temperature according to the Curie-Weiss law:

$$\chi(T - \theta) = \text{const.} \quad (2.12)$$

Similar characteristic was found in many ferromagnetic materials in the initial susceptibility $\chi(T)$ by Hopkinson in 1889 [35]. The main argumentation for this effect is the derived relation for the initial susceptibility $\chi \sim \frac{M_{Sat}}{\sqrt{K}}$, where K denotes the anisotropy. For the derivation of this formula considerations and approximations for the wall energy of magnetic domains were used [28]. The description works quite well for a lot of substances in the low-field region, as the value for anisotropy will approach zero around the Curie-Temperature, which creates a mathematical unsteadiness leading to a peak in the susceptibility $\chi(T)$ for $T \rightarrow T_C$.

While the peak in the low field or initial susceptibility χ can be described by domain wall energy effects, this explanation does not hold for the peak in the high field susceptibility κ . At sufficiently high fields no domain walls can be observed. With the help of the Langevin theory and the Weiss molecular field theory [36] the (high field) susceptibility is given by the Langevin function $L(\alpha) = \coth(\alpha - \frac{1}{\alpha})$ [28]:

$$\kappa = \frac{NM_{Sat}^2 L'(\alpha)}{k_B(T - 3\Theta_f L'(\alpha))}. \quad (2.13)$$

With $\alpha = \frac{M_{Sat}(H+wM)}{k_B T}$, where w is the molecular field coefficient, Θ_f the ordering (Curie) temperature and N the number of spins. As the temperature

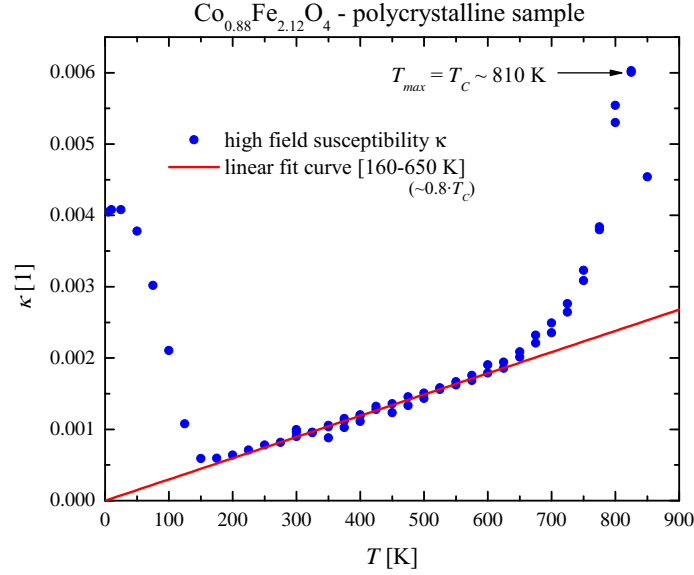


Figure 2.2: High field susceptibility κ of polycrystalline cobalt ferrite with the two typical features: the linearity below T_C and the peak around T_C (Own measurement, the increase below $T = 150$ K is discussed in chapter 6).

T is approaching the ordering temperature Θ_f (or T_C), the denominator of formula 2.13 is vanishing and the high field susceptibility κ approaches infinity. Above θ_f , formula 2.13 becomes the well known Curie-Weiss law (formula 2.12). In figure 2.2 the high field susceptibility κ of a polycrystalline cobalt ferrite sample is plotted. Below $T = 150$ K the sample can no longer be saturated due to the high anisotropy, which results in a bad fit (see chapter 6 for a more detailed discussion on this sample). Whereas from 160 to 650 K the high field susceptibility is in excellent agreement with formula 2.11 where A was determined to 34.53 meV^{-1} .

Finally, it is important to note that it has been observed that κ is independent of the metallurgical history of the sample [34, 37, 29]. This shows that κ is indeed an intrinsic material parameter.

2.2.3 General remarks on the LAS

When using the LAS it is important to keep in mind that this phenomenological method has its limits. One limitation is clearly that it can be mainly used for polycrystalline materials without texture. Another limitation can be seen when changing the borders for the fitting procedure: the result can vary within certain limits. The anisotropy related constant b can change easily within one order of magnitude, just like the high field susceptibility. At least this effect does not affect the saturation magnetization in such a strong way. In figure 2.3 the contributions to the LAS are plotted as function of field for a Fe_3O_4 reference sample. While the anisotropy related contribution $\frac{bM_{\text{Sat}}}{H^2}$ is decreasing with increasing field, the high field susceptibility κH is constantly increasing and giving the main contribution at 80 kOe. The green line represents the best fit to the experimental curve.

The LAS is not the sharpest tool for analyzing magnetization data. The

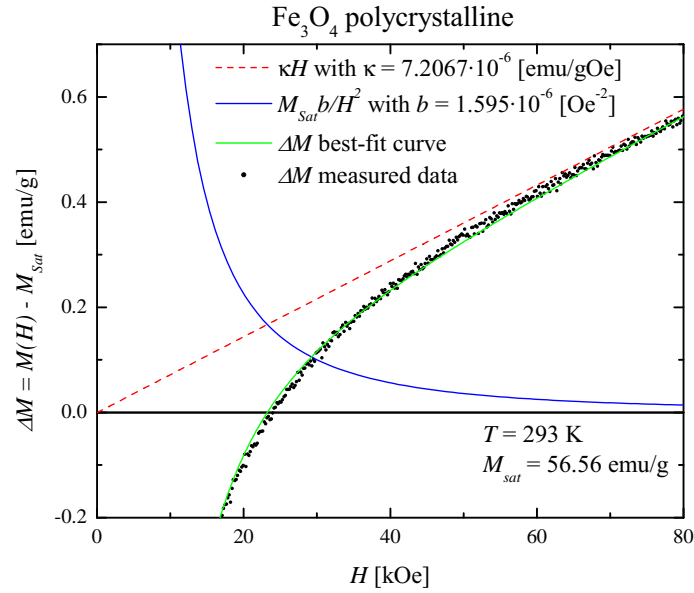


Figure 2.3: Contribution of the main two terms of the law of approach to saturation and the comparison with the room temperature measurement of a polycrystalline Fe_3O_4 reference sample.

results are always dependent on the user defined borders of the magnetic field for the fitting procedure and the number of terms which are used for the fit. Accordingly all obtained variables are (linearly) dependent on each other and so an absolute result can never be obtained. The formula of the LAS contains not a set of orthogonal functions, therefore the obtained fit parameters change with the number of used parameters. As long as one keeps these limitations in mind, it is still possible to gather a lot of information and intrinsic material parameters from the magnetization measurement of a polycrystalline sample.

2.3 Magnetism of Spinel Ferrites

2.3.1 Structural Properties

One of the most important and by humans longest known magnetic materials is magnetite Fe_3O_4 which belongs to the group of the spinel ferrites. A spinel ferrite is formed by metal cations sitting on two distinct crystallographic positions with oxygen as anion, usually in the chemical sum formula $(\text{A})[\text{B}_2]\text{O}_4$. The unit cell consists of eight formula units, with eight tetrahedral places (A), 16 octahedral (B) sites and 32 oxygens [2, 4].

The spinels or spinel ferrites are a very large group of oxides which possess cubic crystal structure. If the $3d$ shell of the metallic cations exhibit a magnetic moment, the overall magnetic structure is ferrimagnetic due to the indirect magnetic coupling through the oxygen ions. The two distinct crystallographic sites (tetrahedral & octahedral) are antiferromagnetically coupled via superexchange. Depending on the type of magnetic ion sitting on one of these two sites, all magnetic properties (T_C , M_{Sat} , K_1 , K_2 , ...) of the spinel vary. The valence state of the metal ions can vary between one up to six, depending on the kind of cation, however in total an electric neutral state has to be achieved. In principle many configurations are known, but in this thesis we restrict ourselves to the combination of a divalent ion (D^{2+}) with two trivalent ions (T^{3+}), as it is found in Fe_3O_4 , NiFe_2O_4 or CoFe_2O_4 .

2.3.2 Degree of inversion

The degree of inversion i is a value between zero and one and denotes the occupancy of one type of divalent cations in the tetrahedral site. If D is a divalent ion and T is a trivalent ion, the spinel can be written as:

$$(D_{1-i}T_i)[D_iT_{2-i}]O_4, \quad (2.14)$$

where the round brackets indicate the tetrahedral and the square brackets indicate the octahedral sites. If for example all divalent ions are placed in the tetrahedral site ($i = 0$), the spinel is called *normal spinel* $(D)[T_2]O_4$ (like $ZnFe_2O_4$: $(Zn^{2+})[Fe_2^{3+}]O_4$). Another extreme is the *inverse spinel* ($i = 1$), where all divalent ions are sitting in the octahedral site $(T)[DT]O_4$ (like $NiFe_2O_4$: $(Fe^{3+})[Ni^{2+}Fe^{3+}]O_4$).

The most common type is however the *mixed spinel*, where i is in between zero and one. Very often the degree of inversion can be changed by the preparation technique or by the heat treatment. At high temperatures (for example, near the melting point) a statistical distribution of the cations in the crystal occurs, leading to $i = \frac{2}{3}$. Assuming a very high cooling rate (quenching) and a slow cation redistribution, this state can be frozen in and remains stable at room temperature. In many cases a simple modified Boltzmann $\frac{i(1+i)}{(1-i)^2} = e^{\frac{-E_{ex}}{k_B T}}$ distribution agrees well with experimental values [4, 38], where E_{ex} denotes the exchange energy between a trivalent and a divalent cation (usually around 0.14 eV [2]).

2.3.3 Crystal electric field

In spinels the crystal electric field (CEF) interaction is much stronger than the spin orbit interaction and therefore the orbital momentum is quenched. This leads to a ground state where $L = 0$, $g = 2$ and $J = S$ with the magnetic moment of the ion $\mu_{eff} = g\mu_B\sqrt{S(S+1)}$. In table 2.1 the magnetic ground states of all three kinds of magnetic ions, which can be found in cobalt ferrite, are listed up. The experimentally obtained value of

Table 2.1: Magnetic ground states for various 3d ions [39].

ion	shell	S	L	J	term	$\mu_{eff} [\mu_B]$	$\mu_{exp} [\mu_B]$
Fe ³⁺	3d ⁵	$\frac{5}{2}$	0	$\frac{5}{2}$	⁶ S _{5/2}	5.91	5.82
Fe ²⁺ (Co ³⁺)	3d ⁶	2	2	4	⁵ D ₄	4.89	5.36
Co ²⁺	3d ⁷	$\frac{3}{2}$	3	$\frac{9}{2}$	⁴ F _{9/2}	3.87	4.90

the effective magnetic moment μ_{exp} is in good agreement with the calculated effective moment μ_{eff} for Fe²⁺ and Fe³⁺, which proves the quenched orbital momentum. For Co²⁺ the spin-orbit coupling can not be fully neglected and therefore the Co²⁺ ions are considered as partly quenched. This is shown in table 2.1. So the theoretical calculation ($\mu_{eff} = g\mu_B\sqrt{S(S+1)}$) does not work for Co²⁺ ions.

With the experimental magnetic moment μ_{exp} of these ions it is possible to determine the degree of inversion i at $T = 0$ K with $\mu = \mu_{B-Sites} - \mu_{A-Sites}$, where the magnetic moments of the A and B sites are calculated according to formula 2.14.

2.3.4 Tetrahedral environment

In figure 2.4a the relative position of the nearest neighbor atoms of the tetrahedral site is shown. The cation is surrounded by four oxygen atoms forming a tetrahedron. The resulting crystal electric field splitting is drawn in figure 2.5a. The 3d-electrons of the free ion are split up into an energetically lower doublet e_g and a triplet t_{2g} . The e_g orbitals point along the crystal axes, while the t_{2g} point in between. The CEF splitting $\Delta = 10Dq$ in the tetrahedral environment is much smaller than in the octahedral environment, because the electrostatic field of the surrounding oxygen ions is smaller. While the tetragonal cation has four oxygen neighbouring atoms, the octahedral cation has six oxygen neighbours.

As the tetrahedral site is crystallographically smaller than the octahedral, the smaller ion usually tends to go to that site. For example in cobalt ferrite (CoFe₂O₄), the ionic radius of a Fe²⁺ ion is 0.92 Å, for a Fe³⁺ it is

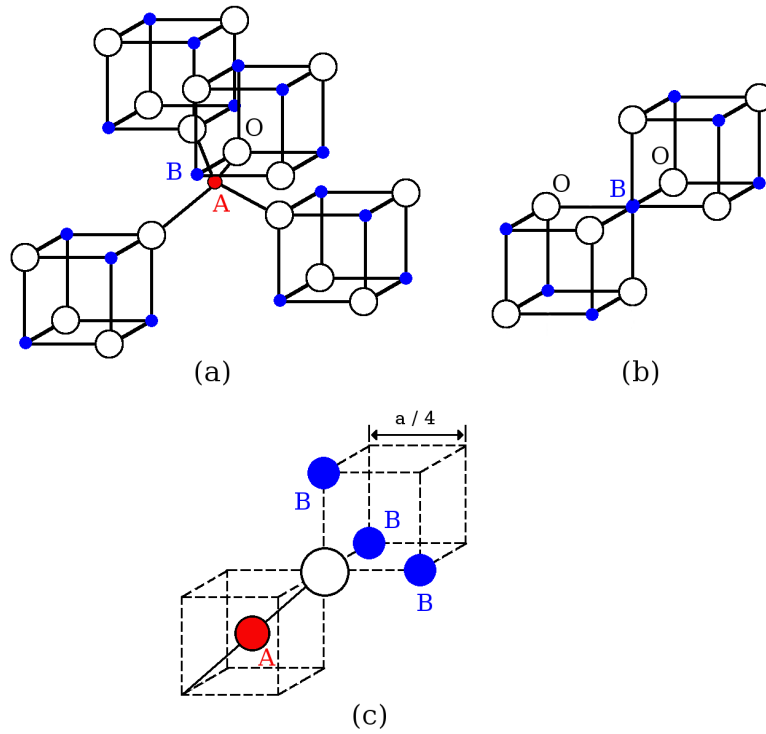


Figure 2.4: Relative position of the nearest neighbour atoms of (a) the tetrahedral (A) site, (b) the octahedral (B) site and (c) the oxygen anion site in spinels (adapted from [2])

0.785 \AA and for a Co^{2+} ion the radius is 0.885 \AA [2, 40]. The smaller Fe^{3+} ion will tend to go on the tetrahedral site, which favors the inverse or mixed spinel structure. Experimental results have shown that the mixed spinel structure is found very often. Generally spoken the degree of inversion can be altered by changing the heat treatment, as mentioned above [41].

2.3.5 Octahedral environment

The energy levels of the $3d$ -electrons in the octahedral sites are split up like shown in figure 2.5b. This is opposite to the tetrahedral sites, because the energy of the triplet t_{2g} lies lower than the doublet e_g . The reason for this behavior is the spatial extension of the triplet and doublet states and their

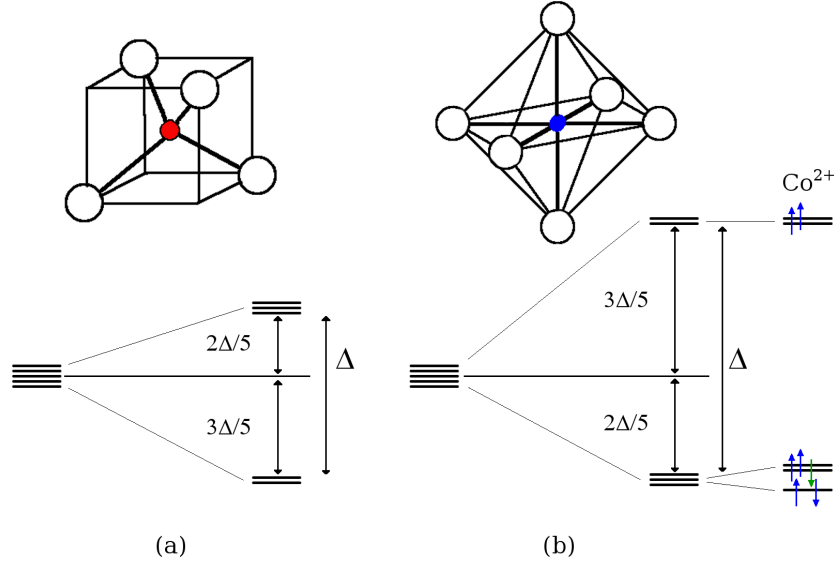


Figure 2.5: Crystal electric field splitting $\Delta = 10 Dq$ in the tetrahedral (a) and octahedral (b) site in spinels (adapted from [39, 28])

local symmetry: the t_{2g} orbitals point in between the crystal axes they are energetically more favorable, while the e_g point along the crystal axes.

In figure 2.4b the octahedral environment is shown. When looking from the $[111]$ axis, a trigonal field from the other octahedral ions is superimposed, but as there are eight equivalent $[111]$ axes the cubic symmetry is not broken. This trigonal field splits the triply degenerated t_{2g} orbitals into a single lower level pointing along the $[111]$ axis and two doubly degenerated higher levels pointing both perpendicular to the $[111]$ axis.

When a Co^{2+} ion is sitting on such an octahedral position, the electrons are filling up the orbitals according to Hund's rule (five spin up and two spin down) as shown in figure 2.5b on the right side. The last electron is marked in green, as it occupies the doubly degenerated level pointing perpendicular to the trigonal axis. This certain electron can switch between these two levels, yielding in a circulating orbit around the $[111]$ axis. In that case the orbital magnetic moment of $L = 1$ is parallel to the trigonal axis with a resulting spin-orbit coupling $\lambda \mathbf{L} \cdot \mathbf{S}$. The result is a large magnetocrystalline anisotropy along the $[111]$ axes, arising due to the presence of a Co^{2+} ion in the octahedral site [17, 2].

Chapter 3

Magnetic Anisotropy

3.1 Types of Anisotropy

Generally spoken, anisotropy describes the dependence of the internal energy on the crystallographic direction of the spontaneous magnetization vector [28] below a magnetic ordering temperature T_C . In the following we will discuss magnetic anisotropy for ferri- and ferromagnetic materials. However quite a lot of different origins can account for magnetic anisotropy:

1. magnetic crystalline anisotropy or magnetocrystalline anisotropy
2. exchange anisotropy
3. shape anisotropy
4. surface anisotropy
5. strain induced magnetic anisotropy
6. texture anisotropy

The first and most important kind of anisotropy is the magnetic crystalline anisotropy or magnetocrystalline anisotropy which will be discussed in the following chapter.

3.2 Magnetocrystalline Anisotropy for the Cubic Case

The magnetic anisotropy describes the dependence of the internal energy on the direction of the magnetization [28]. As the magnetic anisotropy usually has the same symmetry as the crystal structure of the investigated material, the magnetic anisotropy is often also called magnetocrystalline anisotropy. In this thesis we restrict ourselves to the description of the cubic magnetocrystalline anisotropy energy E_A , as cobalt ferrite crystallizes in a cubic crystal structure.

3.2.1 Anisotropy Constants

For describing the cubic symmetry the use of the direction cosines α_1 , α_2 , and α_3 is very common, as they represent the spherical coordinate system (with radius of 1):

$$\alpha_1 = \sin \theta \cos \phi \quad (3.1)$$

$$\alpha_2 = \sin \theta \sin \phi \quad (3.2)$$

$$\alpha_3 = \cos \theta, \quad (3.3)$$

with the inclination angle θ and azimuth angle ϕ . The anisotropy energy is expanded in a polynomial series of the α_i . One should keep in mind that due to the fact that the energy has to be positive, the odd powers of the α_i are zero. The expansion is also invariant to an exchange of any of the α_i , as the cubic symmetry of the crystal can not be broken. With the help of these considerations the magnetocrystalline anisotropy energy E_A is defined as:

$$E_A = K_0 + K_1(\alpha_1^2\alpha_2^2 + \alpha_2^2\alpha_3^2 + \alpha_1^2\alpha_3^2) + K_2(\alpha_1^2\alpha_2^2\alpha_3^2) + K_3(\alpha_1^4\alpha_2^4 + \alpha_2^4\alpha_3^4 + \alpha_1^4\alpha_3^4) + \dots \quad (3.4)$$

with the field independent anisotropy constants K_i . For most magnetic systems the first and the second order anisotropy constant K_1 and K_2 are sufficient to describe E_A . Therefore we neglect the higher order anisotropy

constants K_3 and K_4 because their contribution is usually very small as compared to K_1 and K_2 .

3.2.2 K_0 - a crystal quality measure

In figure 3.1 the simple contribution of $K_0 = 1$ to the anisotropy energy is plotted. It describes the direction independent energy of the magnetization process of a sample. A quarter of the sphere is cut out for better visibility. This direction independent contribution is very important as it is not reflecting the work against the magnetocrystalline anisotropy [3]. Strictly spoken K_0 is not a part of the magnetocrystalline anisotropy, nevertheless it is an important part for describing the measured anisotropy as it reflects the quality of the single crystal. In a perfect single crystal without any dislocations, K_0 should be zero, as no work should be carried out when applying a magnetic field. While an actual single crystal has some imperfections, like impurities, small concentration variations or dislocations, the value of K_0 can be taken as measure for the quality of the single crystals.

When magnetizing a sample along the easy axis, say for example the [100] axis (as it is for iron or cobalt ferrite), no contribution from the K_1 and K_2 term is given to the anisotropy energy E_A (see formula 3.4). The only term remaining is K_0 , as $\alpha_2 = \alpha_3 = 0$ and $\alpha_1 = 1$. It is clear that the magnetization vector should point along the easy axis when no field is applied, as this is the definition of the easy axis. However the internal strains and dislocations of a sample can create a small difference in the energy of the ground state between the 6 different easy axis of a cubic system, leading to a small tilting of the magnetization vector away from the easy axis. Moreover due to the formation of magnetic domains, the stored domain energy has to be overcome when magnetizing the sample. This additional energy is reflected in K_0 .

When we name the averaged internal strains of the sample with σ_{int} , the magnetization work along the easy axis can be approximated with $W_{100} \sim \lambda_{100}\sigma_{int}$, where λ_{100} is the magnetostriction value along the [100] axis. In [3] an example for iron is given: After measurements from [42] $W_{100} \sim 10^4 \frac{\text{erg}}{\text{cm}^3} = 10^3 \frac{\text{J}}{\text{m}^3}$ with $\lambda_{100} \sim 2 \cdot 10^{-5}$ at room temperature this leads

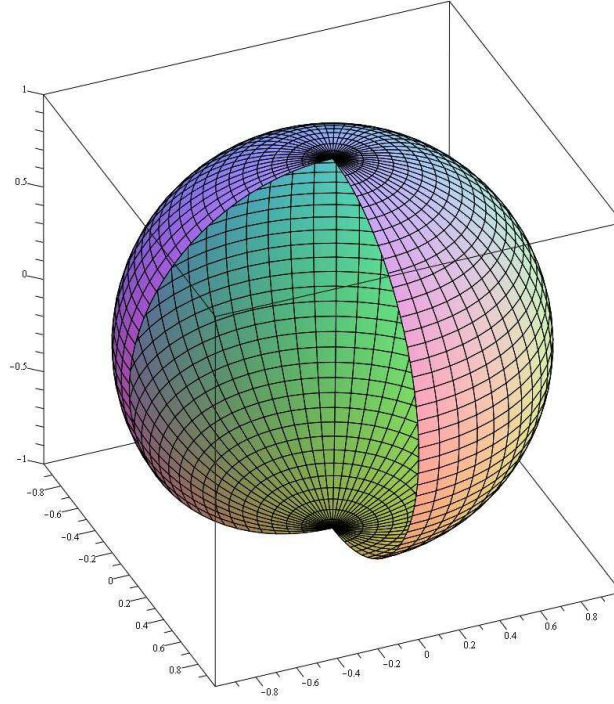


Figure 3.1: K_0 , the isotropic, angular independent contribution to $E_A(\theta, \phi)$. A quarter is cut out for better visibility.

to $\sigma_{int} \sim 5 \cdot 10^7 \frac{\text{N}}{\text{m}^2} = 50 \text{ MPa}$. This value for the internal stress is quite reasonable for pure, mechanically soft iron.

3.2.3 K_1 - an indication for the easy and hard axis

In figure 3.2a the anisotropy energy with a positive K_1 is plotted. It can be clearly seen in the cut out quarter of the graph that the minimum of the anisotropy energy function, which is the magnetic easy axis, lies in the main crystallographic axis $[100]$, while the maximum (hard axis) lies in the $[111]$ axis. Quite opposite is the case for a negative K_1 , as can be seen in figure 3.2b, where the magnetic easy axis is the $[111]$ and the magnetic hard axis is the $[100]$. An additional positive contribution $K_0 = 1$ was added in order to avoid negative lobes of E_A .

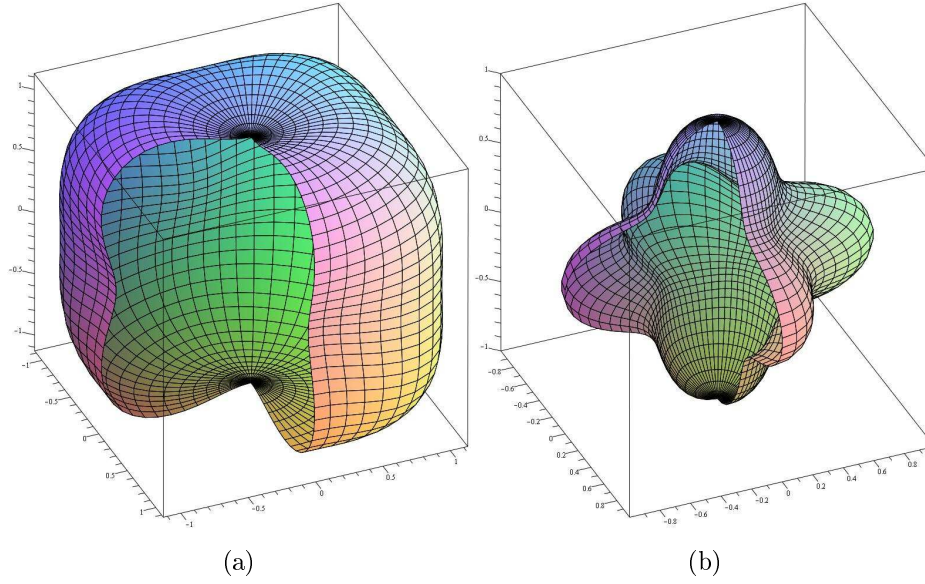


Figure 3.2: The first magneto-crystalline anisotropy constant K_1 : (a) $K_0 = 1$ and $K_1 = 1.5$ (b) $K_0 = 1$ and $K_1 = -1.5$. A quarter is cut out for better visibility.

3.2.4 K_2 - defining the intermediate axis

The second order anisotropy constant K_2 makes the whole anisotropy energy function a bit more complicated. The main contribution of K_2 is a negative or positive lobe to the anisotropy energy along the $[111]$ axis as can be seen in figure 3.3, yielding in a change of the magnetic easy, intermediate and hard axis. Figure 3.4 shows the parameter space of K_1 versus K_2 , which makes the three main cases more evident [43]. When K_1 is positive and $K_2 > -9K_1$ then the $[100]$ axes are the easy axes, which is denoted by “P” in figure 3.4. The second case is characterized by a negative K_1 and $K_2 > -\frac{9}{4}K_1$, which is named “I”-type and prefers the $[110]$ directions. In all other relations of K_1 and K_2 the $[111]$ directions are favoured and this case is named “N” in figure 3.4. However there exist three additional cases where the magnetic intermediate axis changes with respect to K_1 and K_2 . This is discussed elsewhere [44]. The degenerated cases, where for example $K_1 = 0$, are discussed in [43].

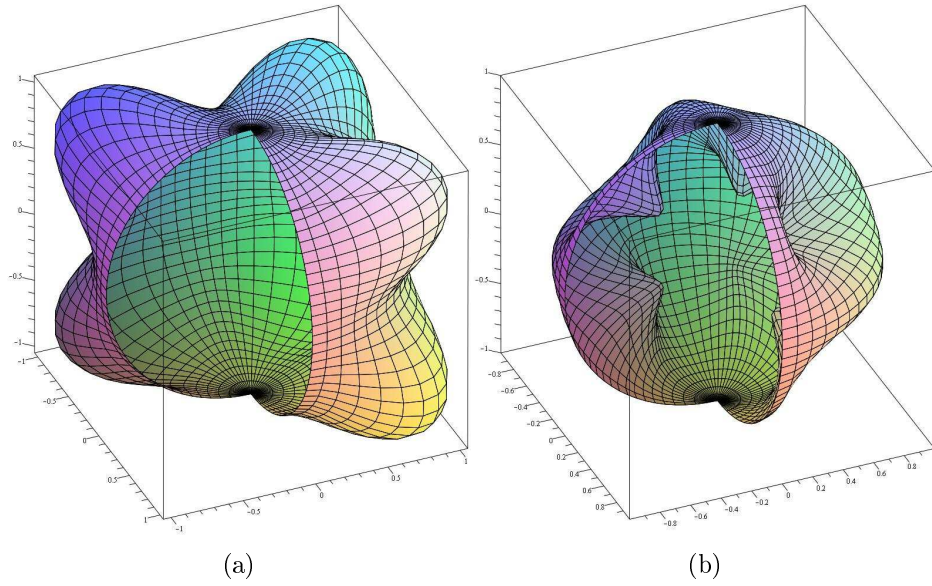


Figure 3.3: The second magneto-crystalline anisotropy constant K_2 : (a) $K_2 = 15$ (b) $K_2 = -15$ ($K_0 = 1$ and $K_1 = 0$ for both cases) quarter is cut out for better visibility.

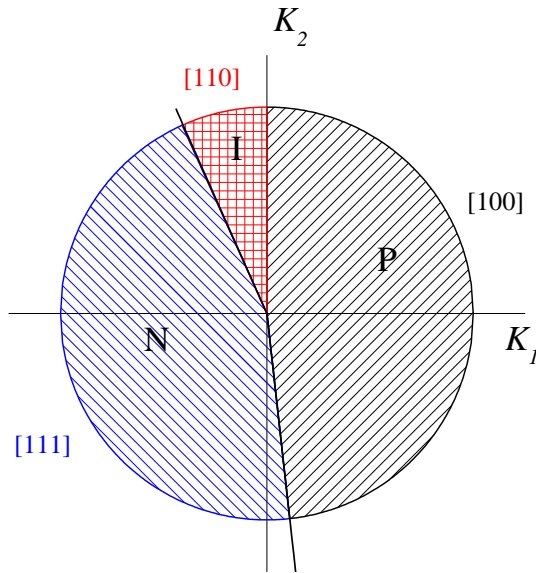


Figure 3.4: Magnetic easy direction as function of the two cubic anisotropy constants K_1 and K_2

3.3 First Order Magnetization Process in the Cubic Case

A First Order Magnetization Process (FOMP) denotes an abrupt change in magnetization $M(H)$, which manifests itself as a jump in the magnetization curve along a certain crystallographic axis. This behaviour was quite often observed in materials with uniaxial anisotropy and a theoretical explanation was supplied as well [45]. Nevertheless it is observed in cubic and other symmetries as well [3, 43].

In a simple picture the magnetization vector has to rotate into the direction of the increasing applied magnetic field. The higher the magnetic field, the higher the magnetic energy in the system (Zeeman energy term: $\mathbf{H} \cdot \mathbf{M}$). As the magnetization vector follows the path where it needs a minimum in energy (Le Chatelier's principle), we can set the total energy E_{tot} of our cubic system to:

$$E_{tot} = K_0 + K_1(\alpha_1\alpha_2 + \alpha_2\alpha_3 + \alpha_1\alpha_3) + K_2(\alpha_1^2\alpha_2^2\alpha_3^2) - \mathbf{H} \cdot \mathbf{M} \quad (3.5)$$

In the following we restrict ourselves to a P-type system (K_1 is positive and $K_2 < -9K_1$), where the easy axis is [100]. When calculating the magnetization as function of the internal magnetic field, we start by parameterizing the rotation of the magnetization vector from the [100] to the [110] axis. Due to symmetry considerations we can stay in the (001) plane. In figure 3.5 the coordinate system is plotted in black. The magnetic field is applied along the [110] axis, which is plotted as red arrow. The magnetization vector is rotating inside the (001) plane from the [100] to the [110] axis, drawn as light grey arrow. The parametrization angle θ is enclosed between the red marked [110] axis and the light grey magnetization vector M :

$$\begin{aligned} \alpha_1 &= \cos\left(\frac{\pi}{4} - \theta\right) \\ \alpha_2 &= \sin\left(\frac{\pi}{4} - \theta\right) \\ \alpha_3 &= 0 \end{aligned}$$

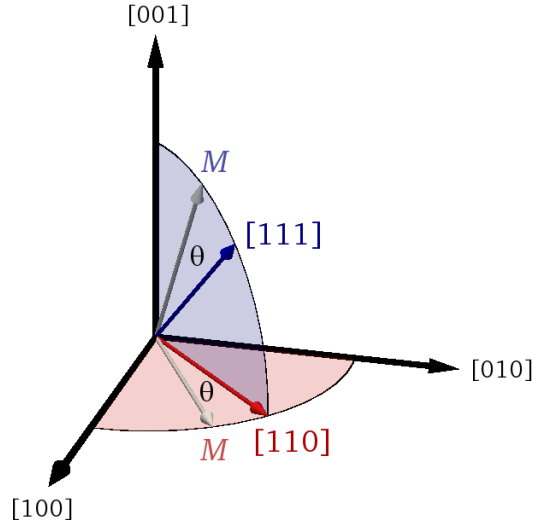


Figure 3.5: red: Parametrization for rotating the magnetization vector M from the $[100]$ axis to the $[110]$ axis where H is applied. blue: Parametrization for rotating the magnetization vector M from the $[001]$ axis to the $[111]$ axis where H is applied.

As θ is decreasing from $\frac{\pi}{4}$ to 0, $M = M_{Sat} \cos \theta$ is rotating towards the field H , which is applied along $[110]$. By substituting $\cos \theta = \eta$ we can write the condition for minimum of the total energy E_{tot} to:

$$\frac{dE_{tot}}{d\eta} = 0 = 4K_1\eta\left(\frac{1}{2} - \eta^2\right) + HM_{Sat}. \quad (3.6)$$

From $\eta = \frac{M}{M_{Sat}}$, it follows that the magnetization as function of the reduced field $h = \frac{HM_{Sat}}{2K_1}$ can be plotted, which can be seen in figure 3.6, where the magnetization along the $[110]$ axis is plotted as dashed line. It is quite remarkable, that the saturation along the $[110]$ axis is completely independent of K_2 . When the reduced field h reaches the value 1, the sample is saturated. For a P-type material the saturation field along the $[110]$ axis is defined as the anisotropy field $H_A = \frac{2K_1}{M_{Sat}}$, as the sample has overcome the anisotropy to be fully saturated.

When H is applied along the $[111]$ axis, we have to parameterize the α_i in

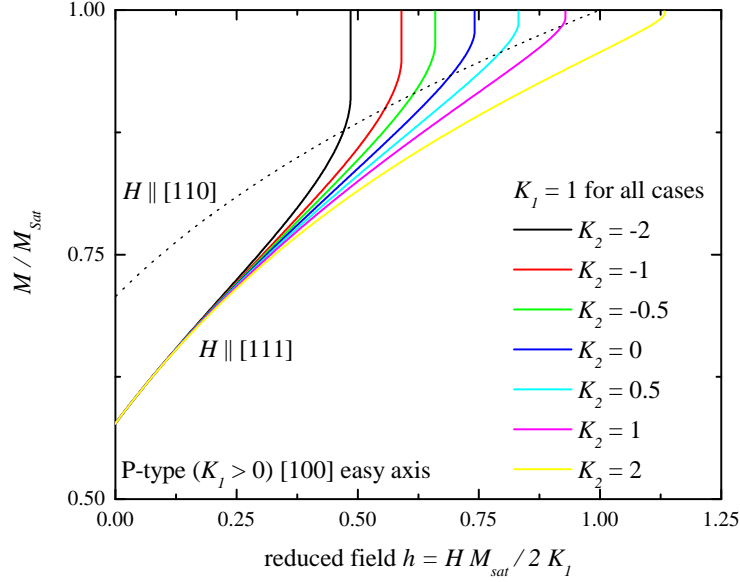


Figure 3.6: Calculated magnetization curves along the $[110]$ and $[111]$ axis of a P-type cubic system with $K_1 = 1$.

such a way that M rotates inside the $(1\bar{1}0)$ plane (see blue plain in figure 3.5):

$$\begin{aligned}\alpha_1 &= \sqrt{\frac{1}{3}} \cos \theta + \sqrt{\frac{2}{3}} \sin \theta \\ \alpha_2^2 &= \frac{1}{2}(1 - \alpha_1^2) \\ \alpha_3^2 &= \frac{1}{2}(1 - \alpha_1^2)\end{aligned}$$

By minimizing again formula 3.5 with respect to θ , we obtain the equation for the magnetization in the $[111]$ direction:

$$\begin{aligned}HM_{Sat} &= \frac{K_1}{3} \left[\eta(7\eta^2 - 3) + \sqrt{2}(4\eta^2 - 1)\sqrt{1 - \eta^2} \right] + \\ &+ \frac{K_2}{18} \left[\eta(1 - 16\eta^2 + 23\eta^4) - \sqrt{2}(1 - 9\eta^2 + 10\eta^4)\sqrt{1 - \eta^2} \right] \quad (3.7)\end{aligned}$$

In figure 3.6 the magnetization along the $[111]$ axis is calculated with different values of K_2 . After the domain wall movement processes are

finished, the reduced magnetization reaches the value $\frac{1}{\sqrt{3}}$. From this point on a further increase of magnetization value is reached by tilting the magnetization vector M from the easy $[001]$ axis to the hard $[111]$ axis. Even for $K_2 = 0$ a singularity at $h = 0.741$ is observed, which yields in a jump of the magnetization. This discontinuity in the magnetization is usually referred as FOMP or sometimes in literature as the “[111] anomaly” [46]. The explanation for this phenomenon lies in an energy barrier between the $[001]$ derived magnetization state and the $[111]$ magnetization. The height of this barrier is approximately $5 \cdot 10^{-4} \cdot K_1$ for $K_2 = 0$, however the height of the barrier depends on the value of K_2 as well [46]. As long as K_2 is bigger than $-9 \cdot K_1$ the jump in the magnetization is visible, as can be seen in figure 3.6.

3.3.1 Numerical evaluation of measured P-type FOMP data

The measurement of the magnetization of a cubic, P-type single crystal along all three major crystallographic axes reveals the following behavior: the magnetic easy axis is the $[100]$, the intermediate follows the $[110]$ axis and the hard axis goes along the $[111]$ axis. While the $[100]$ axis delivers the saturation magnetization M_{Sat} value at a certain temperature, the magnetization along the $[110]$ axis reveals the anisotropy field H_A at the point of magnetic saturation. For further analysis of the FOMP along the $[111]$ axis, it is necessary to use the reduced magnetization $\eta = \cos \theta = \frac{M}{M_{Sat}}$ and the reduced magnetic field $h = \frac{HM_{Sat}}{2K_1}$, as it was already introduced in the previous section. The theoretical calculation following formula 3.7 delivers the reduced FOMP field as function of the reduced magnetization $\eta = \eta_{FOMP}$ with the help of $\zeta = \sqrt{1 - \eta^2}$ to:

$$h_{FOMP} = \frac{\eta}{6}(7\eta^2 - 3) + \frac{\sqrt{2}}{6}(4\eta^2 - 1)\zeta - \frac{(7\eta^2\zeta - \zeta + 3\sqrt{2}\eta - 4\sqrt{2}\eta^3)(\eta(1 - 16\eta^2 + 23\eta^4) - \sqrt{2}(1 - 9\eta^2 + 10\eta^4)\zeta)}{2(\zeta - 48\eta^2\zeta + 115\eta^4\zeta + 19\sqrt{2}\eta - 67\sqrt{2}\eta^3 + 50\sqrt{2}\eta^5)} \quad (3.8)$$

In figure 3.7 the reduced FOMP field h_{FOMP} is plotted as function of the reduced magnetization, as calculated in formula 3.8. As an example let us assume the reduced FOMP field of a measured sample to be $h_{FOMP} = 0.384$. By solving formula 3.8 the calculated value of reduced magnetization is $\eta_{FOMP} = 0.862$, which means that the height of the jump in the reduced magnetization along the $[111]$ axis is $1 - 0.862 = 0.138$. These values are plotted in figure 3.7 as dashed line. The jump in the magnetization is plotted as red double arrow

With the determination of the reduced FOMP magnetization angle η_{FOMP} , it is possible to calculate the ratio of the second and first order cubic anisotropy constant for $\eta = \eta_{FOMP}$ with the help of $\zeta = \sqrt{1 - \eta^2}$:

$$\frac{K_2}{K_1} = \frac{18(-7\eta^2\zeta + \zeta - 3\sqrt{2}\eta + 4\sqrt{2}\eta^3)}{\zeta - 48\eta^2\zeta + 115\eta^4\zeta + 19\sqrt{2}\eta - 67\sqrt{2}\eta^3 + 50\sqrt{2}\eta^5}. \quad (3.9)$$

However it has to be noted that the first anisotropy constant K_1 has to be

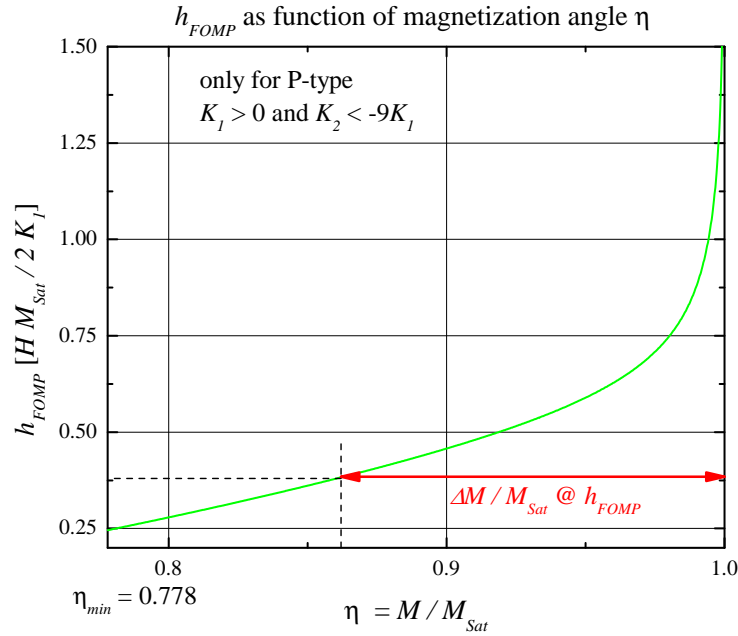


Figure 3.7: Calculated reduced FOMP field h_{FOMP} as function of the reduced magnetization $\eta_{FOMP} = \frac{M_{FOMP}}{M_{Sat}}$, according to formula 3.8.

positive and the second anisotropy constant $K_2 < -9K_1$, in order to fulfill the prerequisites of the P-type anisotropy. A result of the second condition is the existence of a minimum reduced magnetization angle $\eta_{min} = 0.778$.

Using formula 3.9 for our example with $\eta_{FOMP} = 0.862$, the ratio of the anisotropy constants is calculated to $\frac{K_2}{K_1} = -3.6$. By using the value of K_1 , which we already obtained from the anisotropy field H_A , it is now possible to calculate the second order anisotropy constant K_2 . Formula 3.9 is plotted in figure 3.8. The reduced magnetization η_{FOMP} is plotted from its minimum value $\eta_{min} = 0.778$ to the maximum of 1, where $\frac{K_2}{K_1}$ diverges. It is remarkable that the FOMP always exists throughout the whole range, although the height of the jump in the magnetization is constantly decreasing, when η_{FOMP} approaches the value of 1 (see figure 3.7).

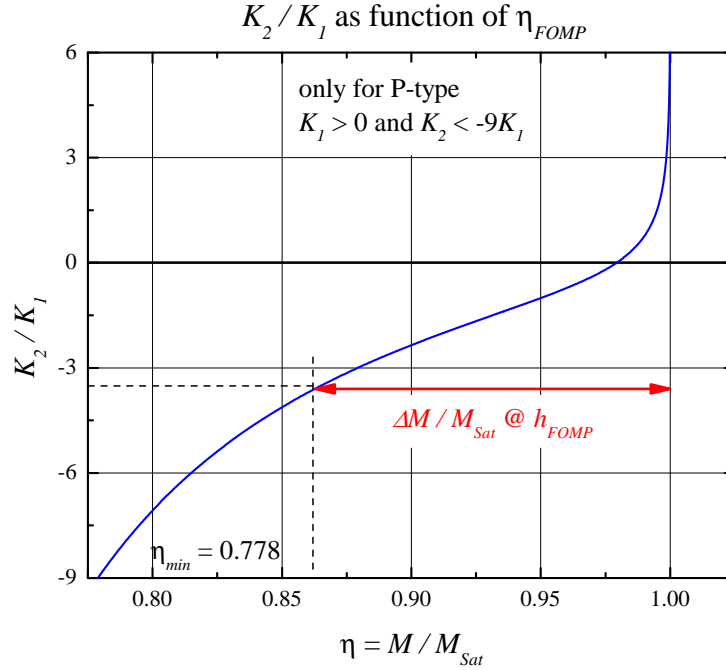


Figure 3.8: Calculated ratio of the anisotropy constants $\frac{K_2}{K_1}$ as function of the reduced FOMP magnetization angle η_{FOMP} , according to formula 3.9.

3.3.2 The cubic FOMP for P-type materials in literature

FOMPs are widely discussed in literature, as they are present in every cubic ferromagnetic material. One very important material is the Yttrium iron garnet (YIG): $\text{Y}_3\text{Fe}_5\text{O}_{12}$. Intensive research has been performed to determine the magnetic properties and to tune them in order to fit the desired application (as e.g. microwave absorption, permanent magnets, ...) [28].

The first example for the FOMP was chosen to be Tb-substituted YIG: $\text{Tb}_{0.1}\text{Yb}_{2.9}\text{Fe}_5\text{O}_{12}$. Lagutin and co-workers [47] determined the first anisotropy constant to $K_1 = 3.4 \cdot 10^5 \frac{\text{J}}{\text{m}^3}$ and the second to $K_2 = -16.7 \cdot 10^5 \frac{\text{J}}{\text{m}^3}$ at room temperature. With these constants the anisotropy of the compound can be classified as P-type. Therefore the FOMP has to be visible in the magnetization along the [111] axis which is plotted in figure 3.9, where the data were digitized from [48]. Clearly the FOMP is visible at temperatures lower than $T < 77\text{K}$. It is interesting to note that with decreasing temperature, the FOMP is getting more and more pronounced as the second anisotropy constant K_2 is further increasing.

The second example of a P-type FOMP in literature is pure and Cd-substituted cobalt ferrite. Guillot and co-workers [26] have measured the magnetization along the [111] axis and found the FOMP at temperatures lower than $T < 150\text{K}$ as can be seen in figure 3.10. A more detailed discussion on the anisotropy constants and the FOMP in cobalt ferrite can be found in chapter 6.2.1.

The third sample is a 0.7 weight-% silicon steel single crystal. The data were digitized from [49] and plotted in figure 3.11. In order to plot the theoretical magnetization curves, the anisotropy constants were fitted to the measured magnetization curves. We obtained for $K_1 = 4.6 \cdot 10^4 \frac{\text{J}}{\text{m}^3}$ and for $K_2 = -0.81 \cdot 10^4 \frac{\text{J}}{\text{m}^3}$.

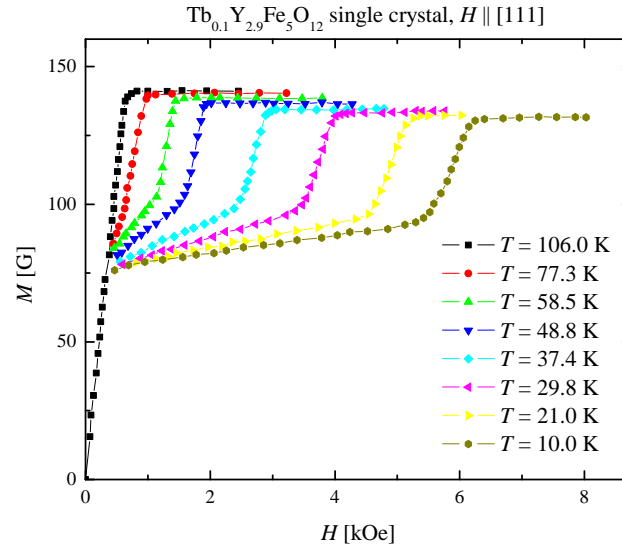


Figure 3.9: Magnetization data of the iron garnet $\text{Tb}_{0.1}\text{Yb}_{2.9}\text{Fe}_5\text{O}_{12}$ along the $[111]$ axis at several temperatures. Data were digitized from [48].

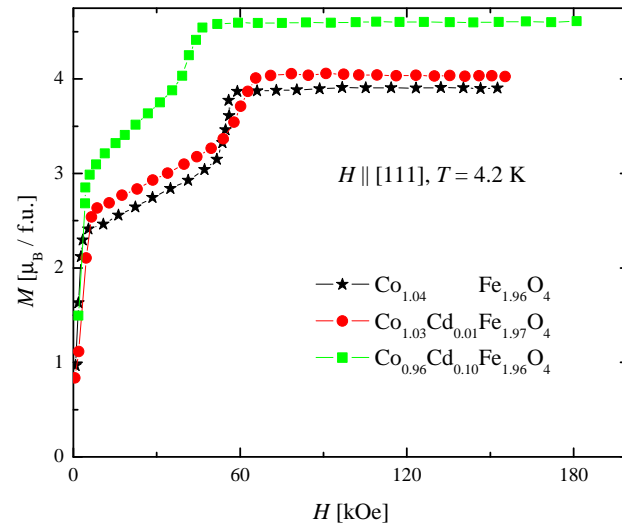


Figure 3.10: Magnetization of Cd-substituted cobalt ferrite measured along the $[111]$ axis at $T = 4.2$ K, digitized from [26].

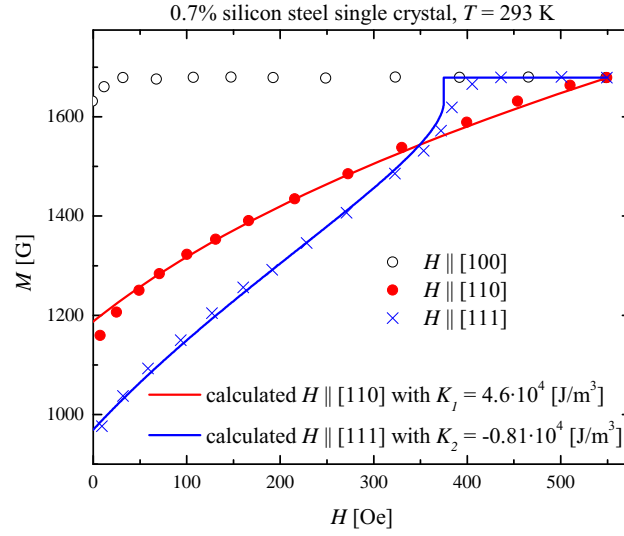


Figure 3.11: Magnetization of 0.7-weight% silicon steel at room temperature, digitized from [26]. The curves are drawn according to formulas 3.6 and 3.7.

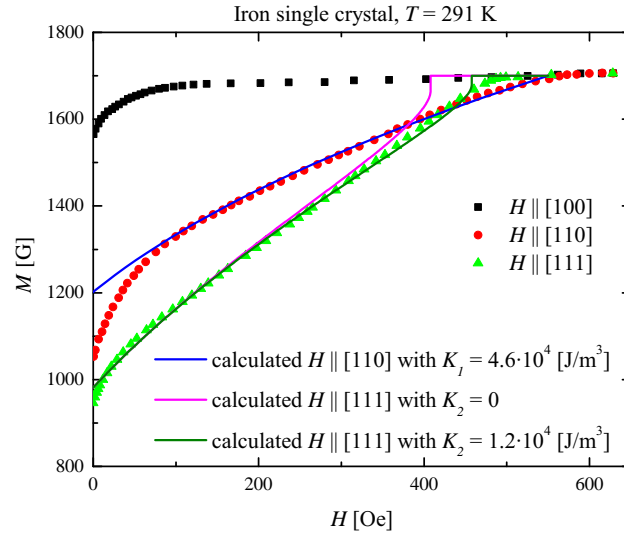


Figure 3.12: Magnetization of an iron single crystal measured at $T = 291$ K, digitized from [42]. The curves are drawn according to formulas 3.6 and 3.7.

Finally, the last example of a FOMP in the literature is pure iron. Although this material is investigated over a hundred years, it is still quite controversial, because the jump in the magnetization is not very clearly visible [50, 42]. In figure 3.12 the magnetization of an iron single crystal at room temperature is shown. These data were digitized from [42]. Our theoretical calculations of the magnetization along the intermediate and hard magnetic axes were plotted according to formulas 3.6 and 3.7. The resulting anisotropy constants are $K_1 = 4.6 \cdot 10^4 \frac{J}{m^3}$ and $K_2 = 1.2 \cdot 10^4 \frac{J}{m^3}$.

The FOMP is not that clearly visible as in the examples shown before. The main reason for that lies in the internal stress of the material. As iron is mechanically quite soft as compared to the YIGs or spinels, a small stress produces an additional uniaxial anisotropy inside the material. Consequently the magnetization curve is smeared out, which hides the FOMP [51, 52]. Even in a single crystal of very high purity, dislocations and the demagnetizing field produce small distortions, which lead to a covered, smeared out FOMP.

3.4 Anisotropy Measurement Techniques

There exist a lot of different measurement techniques for determining the magnetic anisotropy [3, 28]. A short list of methods is given here :

1. Law of approach to saturation
2. Integral method
3. Torque method
4. Ferromagnetic resonance

Among these the law of approach to saturation and the integral method are the two used for evaluating the data of this thesis. Therefore they will be introduced and discussed in more detail.

3.4.1 Law of Approach to Saturation

This method is mainly applied for untextured, isotropic polycrystalline materials. The use and its limitations are described in more detail in chapter 2.2.

3.4.2 Integral Method

For using the integral method the magnetization curve of a single crystal has to be measured along certain crystallographic directions until full magnetic saturation. The number and the directions of the axis depend on the crystal structure and the symmetry which lies therein. When we restrict ourselves to the cubic case, it is necessary to measure the magnetization along the three main axis $[100]$, $[110]$ and $[111]$ in order to determine the first three anisotropy constants K_0 , K_1 and K_2 . The anisotropy energy E_A is defined in formula 3.4. When measuring along a certain $[hkl]$ axis, E_A is equivalent to the performed work:

$$E_{A[hkl]} = \int_0^{M_{Sat}} H_{[hkl]} dM_{[hkl]}. \quad (3.10)$$

With the energies of the three main crystallographic axes the anisotropy constants are given by:

$$\begin{aligned} K_0 &= \int_0^{M_{Sat}} H_{[100]} dM_{[100]} \\ K_1 &= 4 \cdot \left\{ \int_0^{M_{Sat}} H_{[110]} dM_{[110]} - \int_0^{M_{Sat}} H_{[100]} dM_{[100]} \right\} \\ K_2 &= 27 \cdot \left\{ \int_0^{M_{Sat}} H_{[111]} dM_{[111]} - \int_0^{M_{Sat}} H_{[110]} dM_{[110]} \right\} - \\ &\quad - 36 \cdot \left\{ \int_0^{M_{Sat}} H_{[110]} dM_{[110]} - \int_0^{M_{Sat}} H_{[100]} dM_{[100]} \right\}, \end{aligned}$$

alternatively expressed in terms of $E_{A[hkl]}$:

$$\begin{aligned} K_0 &= E_{A[100]} \\ K_1 &= 4 \cdot (E_{A[110]} - E_{A[100]}) \\ K_2 &= 27 \cdot (E_{A[111]} - E_{A[110]}) - 36 \cdot (E_{A[110]} - E_{A[100]}). \end{aligned}$$

Two important points on this method should be considered: First, it is a prerequisite to saturate the sample fully. When the sample is not saturated, the method fails and will deliver wrong values. Second, this method might produce wrong signs for K_2 , when the absolute value of K_2 is small compared to K_1 . That behaviour is well known in literature [42, 3] and can not be avoided, as the integration error along the certain directions is propagated in the calculation.

An additional possible source of error is the shape of the sample. The ideal sample is a spherical or ellipsoidal single crystal where the demagnetizing field can be corrected exactly. That can not always be fulfilled and the shape anisotropy of the sample has to be taken into account. With the help of the demagnetizing factor the internal magnetic field can be calculated with $H_{int} = H_{ext} - N \cdot M$. The demagnetizing factor N can be calculated under certain assumptions according to [53]. Nevertheless it is an approximation and a spherical sample should be favoured.

Chapter 4

Magnetostriction

4.1 Definition - the Cubic Case

Magnetostriction denotes the relative change of length of a sample under an applied magnetic field H [3, 28]. For all materials the magnetization, magnetic anisotropy, magnetostriction and many other physical properties are dependent on the crystal structure and the resulting symmetry of the lattice. For this thesis we restrict ourselves to a cubic crystal structure, as all here investigated materials have cubic crystal structure. The saturation magnetostriction of a cubic material can be described with the well known [3, 28, 54] relation:

$$\frac{\Delta l}{l} = \frac{3}{2}\lambda_{100}(\alpha_1^2\beta_1^2 + \alpha_2^2\beta_2^2 + \alpha_3^2\beta_3^2) + 3\lambda_{111}(\alpha_1\alpha_2\beta_1\beta_2 + \alpha_2\alpha_3\beta_2\beta_3 + \alpha_1\alpha_3\beta_1\beta_3) \quad (4.1)$$

where the α_i are the direction cosines of the magnetization vector and the β_i are the direction cosines of the observed direction. For the definition of the α_i and β_i see formula 3.3. The field independent constants λ_{100} and λ_{111} are the two cubic saturation magnetostriction constants. With these two constants it is possible to describe magnetostriction in any field direction with the above formula, as for example the magnetostriction in the $[110]$ crystal axis λ_{110} :

$$\lambda_{110} = \frac{1}{4}\lambda_{100} + \frac{3}{4}\lambda_{111} \quad (4.2)$$

For the general polycrystalline case it is necessary to measure the magnetostriction parallel λ_{\parallel} and perpendicular λ_{\perp} to the magnetic field in order to calculate the saturation magnetostriction λ_{Sat} :

$$\lambda_{Sat} = \frac{2}{3}(\lambda_{\parallel} - \lambda_{\perp}) \quad (4.3)$$

However for the isotropic, polycrystalline case $\lambda_{\parallel} = -2\lambda_{\perp}$ is valid, leading to:

$$\lambda_{Sat} = \lambda_{\parallel} = \frac{2}{5}\lambda_{100} + \frac{3}{5}\lambda_{111} \quad (4.4)$$

The last part of this formula is derived by averaging formula 4.1 over all crystal directions under the assumption that the grains are completely randomly distributed inside the polycrystalline sample and no texture is present.

4.1.1 Remanent Magnetostriction

As magnetostriction is a relative change in length $\frac{\Delta l}{l} = \frac{l-l_0}{l}$, it is important to know about the initial state l_0 of the sample. Remanent magnetostriction λ_{Rem} denotes the irreversible change of length after applying a magnetic field. The origin of this effect lies mainly in the formation of irreversible magnetic domains inside a magnetic sample with a non-zero coercivity. It can be observed in polycrystalline samples with sufficient high coercive field H_C , as mainly the grain boundaries are a possible source of pinning spots for magnetic domains. Unfortunately this effect can not be measured repetitively, so after the first measurement of $\lambda(H)$ the sample has to be demagnetized by heating above the Curie temperature. In analogy with the hysteresis curve $M(H)$ the first $\lambda(H)$ measurement corresponds to the “virgin” curve. If the sample will be “demagnetized” by applying an alternating magnetic field with a continuously damped amplitude, usually the irreversible domain walls do not vanish completely and so the sample still exhibits a remanent magnetostriction, although with a reduced value. As a rule of thumb it can be said that as soon as a sample has a remanent magnetization, it will have a remanent magnetostriction - this is only important if the demagnetizing field H_D is smaller than the coercive field. Unfortunately this effect is very rarely

discussed in literature [55, 22], especially in connection with its identification and correct methods of measurement. Although there exist models on treating this effect [56, 57].

In figure 4.1 the magnetization and magnetostriction of a polycrystalline Cobalt Ferrite sample was measured. When starting from the origin in both curves, the magnetization and the magnetostriction increase until they are near the saturation value - marked with “A” (At this temperature the saturation of this material would be reached at 160 kOe - see chapter 6). When reducing the magnetic field to zero, the remanence point “B” is reached. This is valid for the ideal case, however in reality “B” is not at $H = 0$ for a sample with finite length. For a magnetic sample in a magnetically open circuit the working point is at $H = -H_D$, the demagnetizing field. Nevertheless at the remanence point “B” the sample has changed its length irreversible (remanent magnetostriction). By increasing the field again to the point “A” both curves follow the same path from “B” as for reducing the field. By reversing the mag-

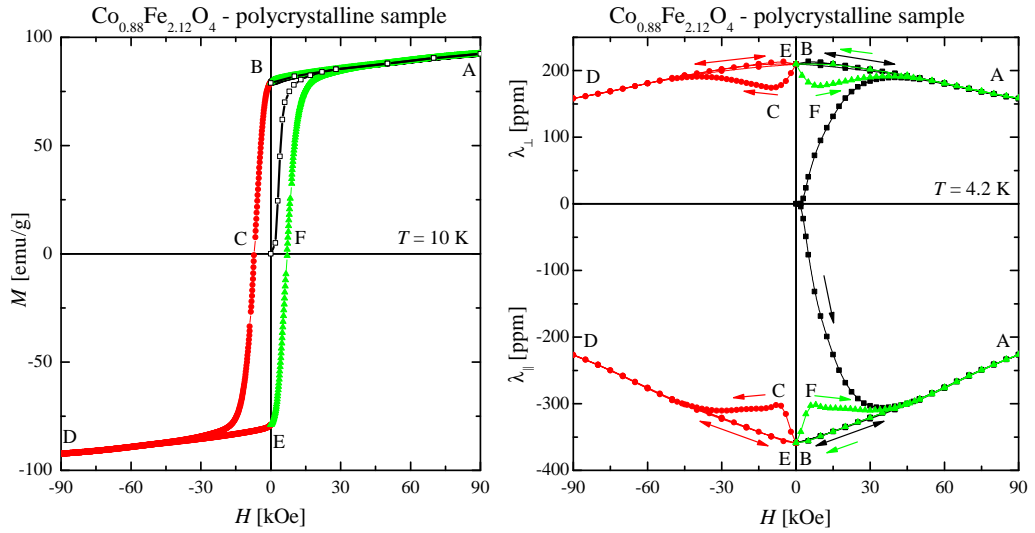


Figure 4.1: Magnetization and magnetostriction measurement of a polycrystalline Cobalt Ferrite sample. The black, open symbols in the magnetization curve are estimated values, as no magnetization measurement of the demagnetized sample was performed.

netic field to point “D” the coercivity “C” can be seen in the magnetostriction as a local minimum or maximum (“C” or “F” in the magnetostriction graph). The enclosed areas (\overline{EDCE} and \overline{BAFB}) of the butterfly shaped magnetostriction measurements correspond to the magneto-elastic losses and can be accounted to the magnetic hysteresis losses inside the sample.

Generally spoken these butterfly shaped magnetostriction curves are pretty hard to explain, nevertheless interpretations and conclusions on magnetostriction measurements on cobalt ferrite can be found in chapter 6.

Magnetostriction along the easy axis of a single crystal

Remanent magnetostriction mainly affects polycrystalline samples, but it can happen as well for single crystalline samples that magnetic domains might affect the magnetostriction measurement. Domain formation is a mechanism for reducing the stray field of the sample. Generally spoken, two kinds of domains can be established inside a sample: 90° and 180° domains. The magnetization vector at zero field is always pointing along one of the easy axes of the single crystal by definition. By applying a magnetic field along one distinct easy axis, all the magnetization vectors of the different domains are tilted and rotated towards the field direction. While the contribution of the 180° domains perpendicular to the magnetic field contribute to the magnetostriction signal, the 180° domains parallel to the magnetic field do not contribute at all, as only rotation processes account for the magnetostriction signal. Whereas the 90° domain wall configuration will only partly account for the magnetostriction signal.

Summing up, when measuring along the easy axis of a single crystal, it might happen that the measured signal is smaller than the actual magnetostriction signal would be. Depending on the initial domain configuration the measured magnetostriction signal can also be not affected at all. A safe way for determining the correct easy axis magnetostriction constant is the measurement of the hard and intermediate axes and the evaluation of formula 4.2, where one can deduce the easy axis magnetostriction constant with the help of the other two constants. As magnetostriction is a relative quantity, the initial length and its domain state(s) always have to be considered [54].

4.2 Measurement Methods

4.2.1 Capacitance Cell

The basic principle of the used capacitance cell (CC) is described by [58]: The sample is clamped in a protective cage inside the two ring shaped electrodes of a capacitance. When applying a magnetic field, the sample is changing its length, which yields in a change of capacitance. The capacitance is measured with an “AH2500A” capacitance bridge from Andeen-Hagerling Inc. The resolution of the capacitance bridge is about 1 aF which corresponds in a relative change of length approximately 10^{-9} [58]. In figure 4.2 the schematics and an actual photo of the used cell can be seen. The whole cell is made of silver because of its excellent thermal conductivity, which minimizes a thermal gradient in the cell on heating or cooling. For electric isolation sapphire washers and kapton foil is used together with brass screws

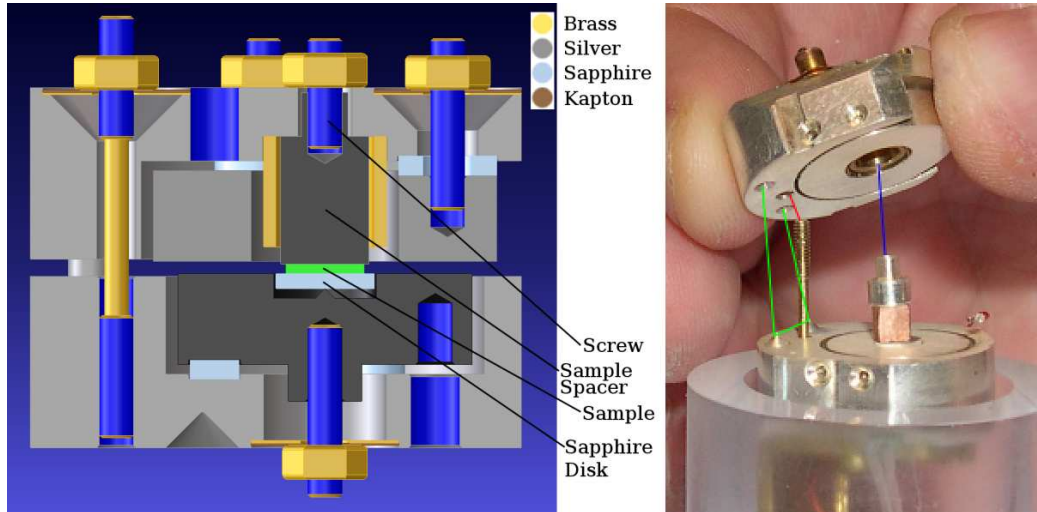


Figure 4.2: Schematics and photo of the capacitance cell for magnetostriction measurement. On the right image the sample (Cu - reference sample) and the silver sample spacer can be seen.

for fixing the cell. In figure 4.2 on the right side a photo of an open cell is shown. Besides the two ring shaped electrodes of the capacitance the sample and the sample spacer are visible. The maximum sample space is a cylinder with 3.5mm in diameter and height. In principle the sample can be of arbitrary shape, but two flat parallel surfaces should generally be favoured. The main advantage over other capacitive cell designs is the tilted plate principle, which leads to a self compensated dilatometer over the whole temperature range yielding in a very low background signal [58]. The temperature range of operation is 2 - 315K as the cell is mounted inside a variable temperature insert in an ^4He -cryostat with a superconducting 90 kOe coil.

4.3 Modelling

There exist numerous models for describing magnetostriction as a function of temperature and magnetic field [54]. Most of them are based on spin-orbit coupling or crystal electric field interactions which is valid for $4f$ -elements. However there exists hardly any good model for describing the magnetostriction of $3d$ -elements including the magnetic anisotropy. Our new developed model is purely phenomenologically, but can be integrated in a quantum-mechanical calculation as well.

In a demagnetized, polycrystalline sample all magnetic domains are randomly distributed, which yields to a macroscopically non-magnetic state. When a magnetic field is applied to the sample, the domains start to align parallel to the field. As soon as all moments are aligned parallel, the magnetization is saturated. The path from the demagnetized to the fully magnetized state can be described with a distribution function. This function has to incorporate various kinds of anisotropies (shape, magnetocrystalline, ...) as well as the internal hysteresis losses due to domain formation and their movement when increasing the field strength. It is clear that the description of such a distribution function is not trivial. Nevertheless a general description for the magnetostriction $\lambda = \frac{\Delta l}{l}$ as function of the applied magnetic field H was

found with a modified distribution function:

$$\lambda(H) = \lambda_0 + \frac{\lambda_1}{1 + e^{f(H)}} + \tau H, \quad (4.5)$$

where special care was taken on the remanent magnetostriction $\lambda_{Rem} = \lambda_0$, the saturation magnetostriction $\lambda_{Sat} = \lambda_0 + \lambda_1$ and the high-field magnetostriction τ . The analytical function $f(H)$ describes the magnetization process inside the magnetic material as function of the applied magnetic field H in a phenomenological way. It includes the magnetic anisotropy and domain rotation processes as well. As this function would get even more complicated when taking the magnetic hysteresis into account as well, we omit hysteresis effects totally. When $f(H)$ is expanded in a polynomial series, it can most accurately be fitted to any magnetostriction measurement:

$$f(H) = \sum_{i=0}^{\infty} a_i H^i. \quad (4.6)$$

In order to reduce the number of parameters to describe this function $f(H)$, we restrict ourselves to the first two elements:

$$f(H) \approx a_0 + a_1 H, \quad (4.7)$$

where we rename the coefficients to get to the final form of our magnetostriction model:

$$\lambda(H) = \lambda_0 + \frac{\lambda_1}{1 + e^{-c_1(H-H_1)}} + \tau H. \quad (4.8)$$

H_1 is exactly the magnetic field value, where half of the saturation magnetostriction is reached. The parameter c_1 describes the steepness of the magnetostriction slope. The two field independent constants c_1 and H_1 can be related to the magnetic anisotropy with the help of the 95% criterion, where the anisotropy field¹ can be estimated: We define the anisotropy field H_A as the magnetic field, where 95% of the moments are aligned and so most of the sample is saturated. However one should keep in mind that the determined anisotropy field is only of the correct order of magnitude as the 95% criterion

¹The term anisotropy field is suitable for the hard and intermediate axes, for the easy axis the term saturation field should be used, in order to be consistent with literature.

is just an assumption:

$$H_A = H_1 - \frac{\ln(\frac{0.05}{0.95})}{c_1} \quad (4.9)$$

with the natural logarithm of the ratio of the criterion.

In figure 4.3 own magnetization and magnetostriction measurements of a Nickel single crystal can be seen. The solid curves in the magnetostriction measurement (right) are fitted according to formula 4.8. The fit parameters can be seen in table 4.1 together with the calculated anisotropy fields. The arrows in the magnetization plot (figure 4.3, right) are indicating the excellent agreement of the anisotropy field in certain crystallographic directions, which were obtained by the magnetostriction model.

The saturation magnetostriction constants are consistent with literature, although one has to be careful when comparing magnetostriction constants of Nickel. Deviations in magnetostriction measurements might arise due to stress, as Nickel reduces its magnetostriction at the presence of (internal) stress [59]. Another question might be the purity grade of the material, be-

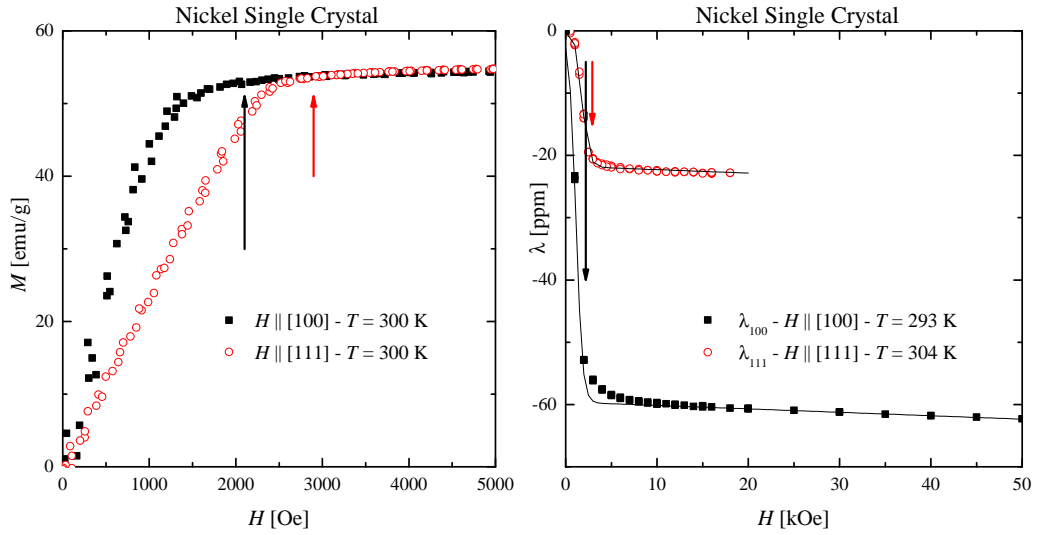


Figure 4.3: Own magnetization and magnetostriction measurement of a Nickel single crystal along two main crystal axis [100] and [111].

Table 4.1: Fit parameters of Figures 4.3 and 4.4 including the calculated anisotropy field.

	T [K]	λ_1 [ppm]	c_1 [ppm ⁻¹]	H_1 [T]	τ [ppm ⁻¹]	H_A [kOe]
Nickel - [100]	293	-58.9	27.67	0.11	-0.55	2.2
Nickel - [111]	304	-21.7	27.13	0.18	-0.55	2.9
Co _{0.8} Fe _{2.2} O ₄ - [111]	4.2	70	2.82	0.55	2.7	
		320.6	5.9	5.5		

cause the higher the purity, the least stress is induced into the sample. Therefore it is difficult to compare magnetostriction measurements even of pure Nickel.

4.3.1 Validity

This model is valid for any ferro-, ferri- or anti-ferromagnetic ordering substance. Moreover it is possible to extend this model to two or more sublattices, simply by adding an additional distribution term:

$$\lambda(H) = \lambda_0 + \frac{\lambda_1}{1 + e^{-c_1(H-H_1)}} + \frac{\lambda_2}{1 + e^{-c_2(H-H_2)}} + \tau H. \quad (4.10)$$

In figure 4.4 as an example the comparison between the measured magnetostriction data and the extended fitting parameters is shown (red curve). In table 4.1 all fit parameters together with the calculated anisotropy fields are listed. All three measurements do not exhibit remanent magnetostriction, which leads to $\lambda_0 = 0$. The anisotropy field H_A was calculated with the help of the 95% criterion in formula 4.9 (More data on Cobalt Ferrite together with an interpretation can be found in chapter 6). Note that the value of the calculated magnetostriction (red curve in figure 4.4) at zero magnetic field is not exactly zero, as it should be. Moreover it can be seen that the slope of the magnetostriction curve in the low field region can not be precisely reproduced. This behaviour shows some problems of that model, which is discussed in the next section.

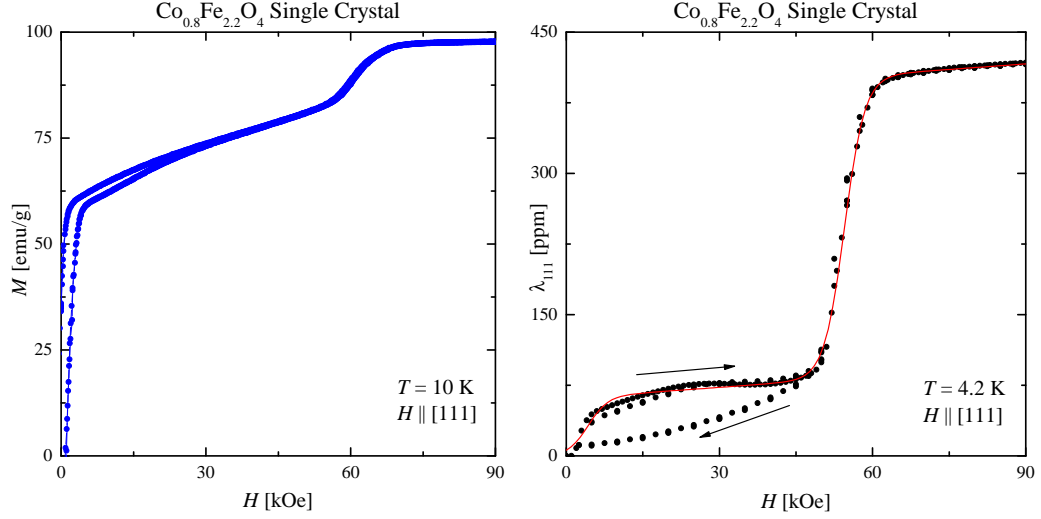


Figure 4.4: Own magnetization and magnetostriction measurement of a Cobalt Ferrite single crystal along the [111] axis.

4.3.2 Limitations

The main weakness of this model lies in the fact that it can not describe micro-magnetically what happens inside the sample while applying the magnetic field. So it can only deliver the maximum value of magnetostriction and an averaged value of the steepness of the magnetostriction slope $\frac{d\lambda}{dH}$. It does not provide any insight to the internal magnetization process which depends on the pre-magnetized state, the microstructure, the internal stress, the magnetic anisotropy and many more physical quantities. The emphasis of that model lies clearly in the inclusion of the magnetic anisotropy together with the saturation magnetostriction of the high-field range and definitely not in the low-field magnetic ordering range, because it does not include magnetic domain effects.

For further development one can improve the distribution function by adding a stress dependent term to the magnetic anisotropy term. Summing up this model proves itself as a valuable tool for describing the magnetostriction process $\lambda(H)$ macroscopically rather well.

Chapter 5

Sample Preparation and Analytics

5.1 Sample Preparation: $\text{Co}_{0.8}\text{Fe}_{2.2}\text{O}_4$ Single Crystal

The single crystal was grown by Prof. Weijun Ren at Shenyang National Laboratory for Materials Science from the Chinese Academy of Sciences in People's Republic of China. He employed a flux method with Borax as flux material [60]. The starting materials are 18 g of Borax ($\text{Na}_2\text{B}_4\text{O}_7 \cdot 10\text{H}_2\text{O}$), 2.3 g CoO of 99.99% purity and 6.7 g Fe_2O_3 of 99.99% purity. After sufficiently mixing, the materials were put in a tightly closed Pt crucible and were heated from room temperature to 1370 °C at a rate of 100 °C/h, and then held for a period of 6 hours. Next, the crucible was slowly cooled from 1370 to 990 °C at 2 °C/h, followed by a furnace cooling by switching off the power supply. The crystals were formed inside the crucible due to the fact that the bottom of the Pt crucible was slightly colder than the top and so the solidification process started. By cooking the flux with the included crystals in a hot dilute solution of 20% HNO_3 as reported in [60] the crystals were separated from the flux. The size of our single crystal was approximately 2x2x1 mm³. Afterwards Prof. Weijun Ren determined the composition of the single crystal with the

help of X-ray Diffraction (XRD) to $\text{Co}_{0.8}\text{Fe}_{2.2}\text{O}_4$.

5.2 Analytics of the $\text{Co}_{0.8}\text{Fe}_{2.2}\text{O}_4$ Single Crystal

5.2.1 Scanning Electron Microscopy Study

In order to determine the exact composition of the cobalt ferrite single crystal and to have a look at the elemental distribution as well as possible concentration gradients a concise Scanning Electron Microscopy (SEM) study was performed. The SEM we used is a JEOL JSM-5040 with an electron backscatter detector and an additional Energy-dispersive X-ray spectroscopy (EDX) detector for elemental analysis. All pictures and spectra were taken at an acceleration voltage of 20 kV and a working distance of 20 mm. In figure 5.1 one can see the triangular (111) plain of the octahedron shaped single crystal at a magnification of 35. In the middle and the right image of figure 5.1, the magnification was increased and one can see small platelets formed during the growing process. The surface of the sample was not ground or polished, as it is very smooth from the crystal growth process.



Figure 5.1: Triangular (111) plain of the as grown, octahedron shaped Cobalt Ferrite single crystal

As it is not possible with EDX to determine the correct amount of lighter elements as oxygen without large error, we could only determine the Fe-Co ratio. Therefore, we first measured over a large area of the sample, turned the single crystal around and measured the second side as well. Later we

performed several spot measurements in order to determine the homogeneity of the single crystal. The measured Fe-Co ratios were found to be quite the same within the experimental error: $\frac{Fe}{Co} = 2.436$. When assuming that the sum of cobalt and iron has to be 3 and the amount of oxygen is 4, the elemental composition of the single crystal is calculated to $Co_{0.87}Fe_{2.13}O_4$ with an experimental error of $\pm 3\%$. No gradients in composition were found as shown in figure 5.2. In the backscatter electron image the change in brightness is referring to different elemental composition. Besides the variation in brightness due to topographical changes, the surface is quite uniform. As in figure 5.2 shown there is only some dirt on the as grown surface of the single crystal, but no stoichiometric gradient over the whole sample. From this investigation it is proven that the single crystal is of high purity without gradients of elemental composition.

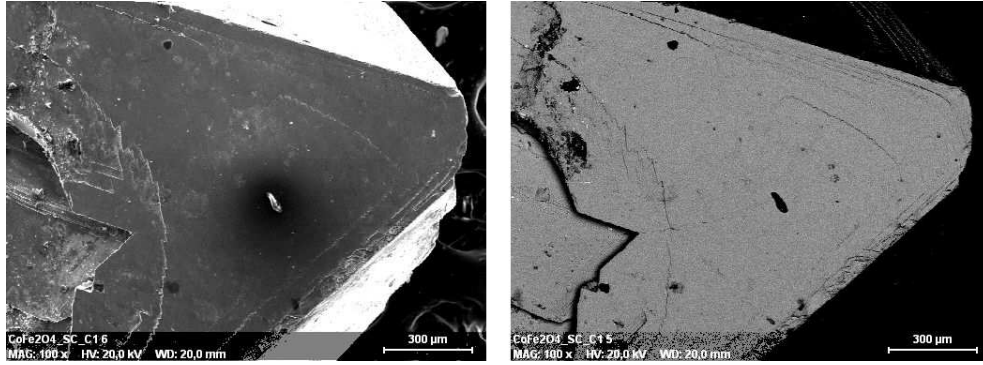


Figure 5.2: left: Secondary electron image of the surface. right: Backscattered Electron Image for checking variation of different elemental composition of the same spot.

5.2.2 Transmission Electron Microscopy Study

It is well known that the oxygen content is very important to the magnetic properties of cobalt ferrite. A lot of studies have been performed on the variation of the oxygen content in the samples. For instance a variation of the oxygen partial pressure while annealing cobalt ferrite influences the saturation magnetization [13] or the sintering of cobalt ferrite under vacuum even

leads to a formation of a second phase and inferior magnetic properties [25]. Therefore, it is important to determine the oxygen content with high accuracy. The aim of the Transmission Electron Microscopy (TEM) study was to determine the exact stoichiometric composition of our single crystal.

As the accuracy of normal X-ray diffraction (XRD) or Energy-dispersive X-ray spectroscopy (EDX) is not sufficient to determine the stoichiometric composition of light elements as oxygen, we employed Electron Energy-loss Spectroscopy (EELS). This technique measures the energy loss of the electron beam (usually 200 keV) in the TEM going through the sample. While passing the sample the incident electrons are scattering with the shell electrons of the sample atoms and lose energy. This loss of energy is dependent on the main shells (K, L_1 , L_2 , L_3 , ...) of the sample atoms and lies in the range of 30 to a few thousand eV, depending on the shell and the sample atom. For our measurements we used the K-edge of oxygen with an energy loss of 532 eV, the L_3/L_2 edges of iron with an energy loss of 708/721 eV and the L_3/L_2 edges of cobalt with an energy loss of 779/794 eV. For performing a

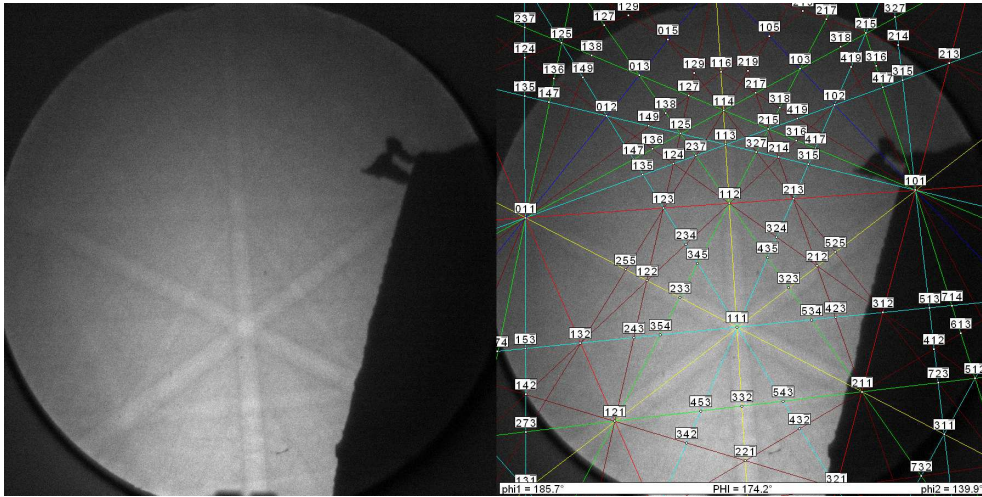


Figure 5.3: SEM-EBSD image of the Cobalt Ferrite single crystal before cutting out the TEM sample from the (111) plain. The Kikuchi lines are visible with and without labeling.

concise TEM study, we first oriented the single crystal along the $[114]$ axis inside a SEM. This was verified by an electron backscatter diffraction (EBSD)

image, where the electron beam is directed in a rather small angle (typically 20°) towards the sample surface. Due to elastic scattering on the regularly assembled lattice of the single crystal a pattern can be detected by a CCD camera. The pattern is arranged in so called Kikuchi bands which reflect the symmetry, structure, lattice parameters and orientation of the sample [61]. In figure 5.3 one can see the Kikuchi bands with and without the calculated structural information. After orientating the single crystal in the $[114]$ axis, a small oriented platelet was cut out of the single crystal with a focused ion beam (FIB). The thickness of the platelet was further reduced by ion-milling to less than 200 nm ($\pm 10\%$). In figure 5.4 one can see the aligned single

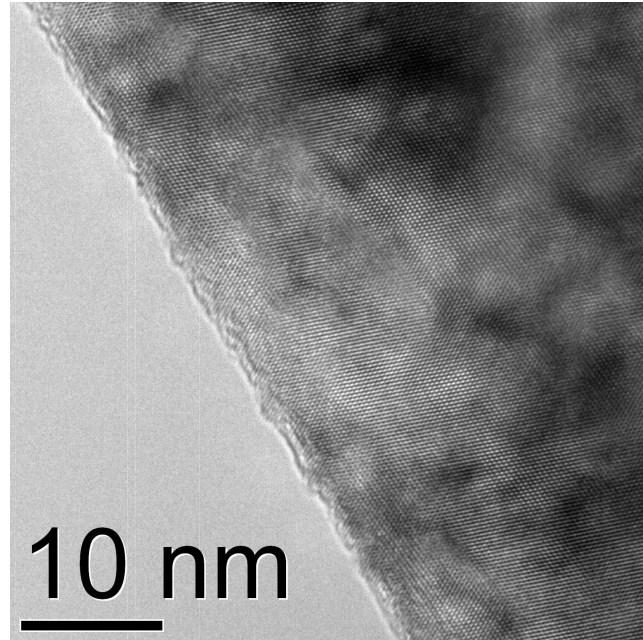


Figure 5.4: TEM image of the Cobalt Ferrite single crystal.

crystal in the TEM. The variation of the brightness in the sample points to a different thickness due to the ion-milling process. In the diffraction pattern in figure 5.5 the $[114]$ axis is visible. By the ratio of $\frac{a}{b} = 1.16$ and the two angles $\angle aa = 50^\circ$ and $\angle ab = 65^\circ$ the $[114]$ direction was verified. In figure 5.6 the raw data of the EELS spectrum are shown on the left side, whereas on the right side the background subtraction (red lines) and the resulting elemental edges (green lines) are shown. Several spectra were taken at different locations of

the sample. The results of this investigation are presented in table 5.1, where we can see that there is just a very slight oxygen defect in the samples.

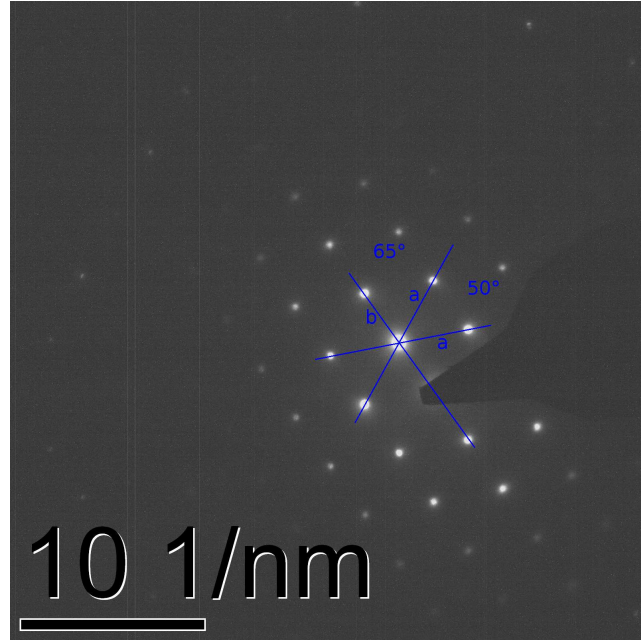


Figure 5.5: Diffraction pattern of Figure 5.4 with the construction lines for the evaluation of the $[114]$ axis.

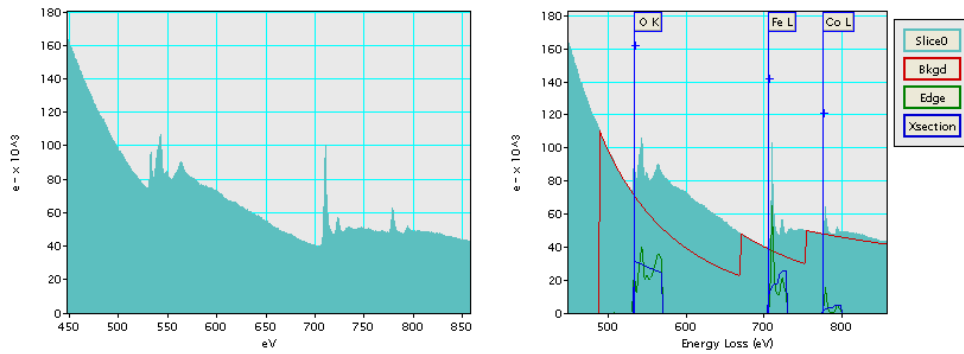


Figure 5.6: Left: EELS Spectrum of Cobalt Ferrite single crystal. Right: Calculated background subtraction and the resulting characteristic energy loss of the oxygen, iron and cobalt ions.

5.2.3 Conclusion

The average Co-Fe ratio was determined with the use of three different and independent methods. All three results are listed in table 5.1. The average composition ($\text{Co}_{0.8}\text{Fe}_{2.2}\text{O}_4$) over all three methods was chosen because it cancels out the various systematic errors of each analytical method. Moreover with the help of the EELS method it is possible to determine the amount of oxygen inside the sample, which was found to be very near to the theoretical value. Among these three methods the EELS method provides the best resolution, with the disadvantage of measuring very locally. Therefore the combination of all three methods ensures that our single crystal is of very high purity with an uniform element distribution. Above all we were able to determine the oxygen content and proved that it is in excellent agreement with the sum formula.

Table 5.1: Composition of cobalt ferrite single crystal compared with a ball-milled polycrystalline sample.

	Single Crystal			Polycrystal
Method	XRD	SEM	TEM-EELS	SEM
Fe/Co ratio	2.75	2.436		2.407
Composition (Co+Fe = 3)	$\text{Co}_{0.71}\text{Fe}_{2.29}\text{O}_{3.95}$			
Composition (Co+Fe = 3 and O = 4)	$\text{Co}_{0.8}\text{Fe}_{2.2}\text{O}_4$	$\text{Co}_{0.87}\text{Fe}_{2.13}\text{O}_4$		$\text{Co}_{0.88}\text{Fe}_{2.12}\text{O}_4$

5.3 Sample Preparation: $\text{Co}_{0.88}\text{Fe}_{2.12}\text{O}_4$ Polycrystalline Samples

There exist numerous methods for preparing polycrystalline Cobalt Ferrite. A quite concise overview on the various production routes is given by [62]. For our polycrystalline $\text{Co}_{0.88}\text{Fe}_{2.12}\text{O}_4$ samples we chose the ball milling technique. Therefore the stoichiometric correct amount of CoO and Fe_2O_3 are put together with steel balls in a ball mill. The ball to powder ratio was kept to 10:1. After 24 hours of continuous milling the powder is given in an oven at $T = 1000^\circ\text{C}$ under air atmosphere where the sample is annealed and forms single phase $\text{Co}_{0.88}\text{Fe}_{2.12}\text{O}_4$. In order to make sure that the crystallite size is more homogeneous, the milling process and the annealing process in the oven have been repeated one more time. Afterwards the powder was pressed into a pellet and the analytical investigations were performed. The single phase, cubic structure and composition were verified with X-Ray Diffraction (XRD). The SEM was used to determine the average size and micro-structure of the crystallites.

5.4 Analytics of the $\text{Co}_{0.88}\text{Fe}_{2.12}\text{O}_4$ Polycrystalline Samples

5.4.1 X-ray Diffraction study

The XRD measurements were performed using $\text{CuK}\alpha_{1,2}$ radiation in a Bragg-Brentano geometry. The evaluation of the data were made using “TOPAS 4.2” (Bruker AXS) software package. All polycrystalline $\text{Co}_{0.88}\text{Fe}_{2.12}\text{O}_4$ samples were single phase and crystallized in the $\text{Fd}\bar{3}\text{mZ}$ space group with lattice parameter of $a = 8.386$ ($\sigma < 1$) Å. The samples were measured with and without rotation of the sample-holder, however no difference was observed. In figure 5.7 a typical diffraction pattern of our polycrystalline samples is shown. Using intensity analysis from XRD diffraction data one can refine an average surface texture of the samples, however no surface texture was found.

The average crystallite size was found to be 206 nm.

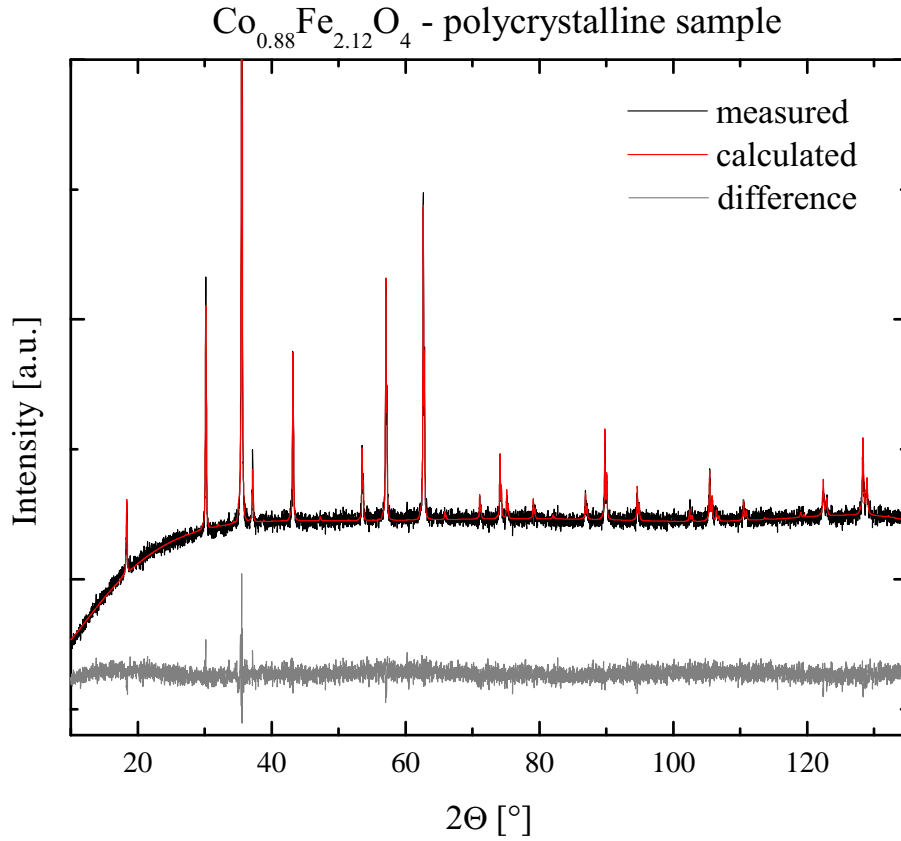


Figure 5.7: XRD pattern of measured polycrystalline $\text{Co}_{0.88}\text{Fe}_{2.12}\text{O}_4$ in black. The red curve denotes the calculated Rietfeld refinement and the grey curve shows the difference between the calculated and measured XRD pattern.

5.4.2 Scanning Electron Microscopy Study

For the determination of the composition of the polycrystalline cobalt ferrite pellet and to check the elemental distribution and possible concentration gradients a scanning electron microscopy (SEM) study was performed. The

SEM we used is a JEOL JSM-5040 with an electron backscatter detector and an additional Energy-dispersive X-ray spectroscopy (EDX) detector for elemental analysis. All pictures and spectra were taken at an acceleration voltage of 20 kV and a working distance of 20 mm. In figure 5.8 the very small grains of the pressed pellets are shown. In table 5.1 the mean results of the evaluation of the EDX spectra are presented.

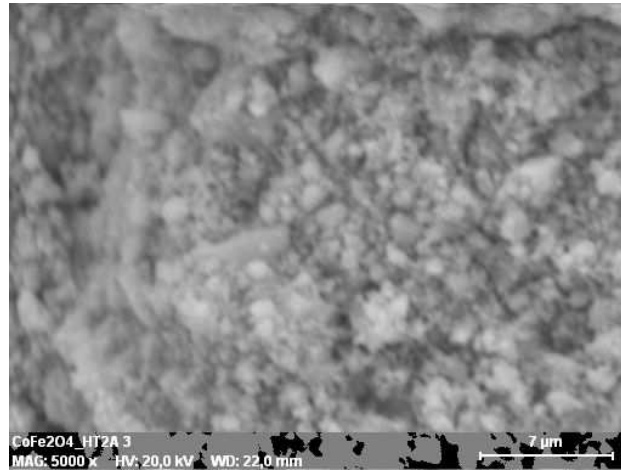


Figure 5.8: Microstructure of nanocrystalline cobalt ferrite, the average crystallite size of 206 nm was determined by XRD.

5.4.3 Conclusion

The average Co-Fe ratio was determined with the use of the scanning electron microscope to 2.407. This sets the composition of the polycrystalline sample to $\text{Co}_{0.88}\text{Fe}_{2.12}\text{O}_4$. With the help of the XRD an investigation on possible textures was performed, which revealed that all the samples were free of texture. This is important, as it is a prerequisite for using the law of approach to saturation (see chapter 2.2).

Chapter 6

Magnetic Properties of Cobalt Ferrite

6.1 Magnetic Properties

The single crystal and the polycrystalline samples were measured in a standard vibrating sample magnetometer (VSM) from Quantum Design Inc., as explained in chapter 2. The single crystal was oriented by use of a backscatter Laue geometry with the software package OrientExpress. Because it was worked very accurately, the average misalignment of the actual to the desired crystal axis was smaller than 1.5° . The three main axes ([100], [110] and [111]) were measured first in the magnetometer and then under the same orientation in the magnetostriction measurement cell (explained in chapter 4). For magnetostriction measurements it was necessary to grind the crystal in order to create two parallel, flat surfaces perpendicular to the desired crystal axis.

Overall one can say that the shape of the single crystal as well as the polycrystalline cylinder-like sample for all magnetization and magnetostriction measurements can be approximated as a sphere ($N = \frac{1}{3}$) [53]. This is important for correcting the external to the internal magnetic field of the sample. With the well known relation $H_{int} = H_{ext} - N \cdot M$ the demagnetizing field was subtracted from the applied magnetic field, yielding to the internal

magnetic field. The used density for evaluating the magnetization data of the single crystal and the polycrystals was the theoretical XRD density $\rho = 5.259 \frac{\text{g}}{\text{cm}^3}$, which we obtained from our XRD refinement.

6.1.1 Magnetization of the Single Crystal

Magnetization as a function of the applied field was measured for a set of crystallographic directions over a very broad temperature range of 10 to 400 K with a maximum applied field of 90 kOe. Only the easy [100] axis was measured in an extended temperature range of 10 to 900 K.

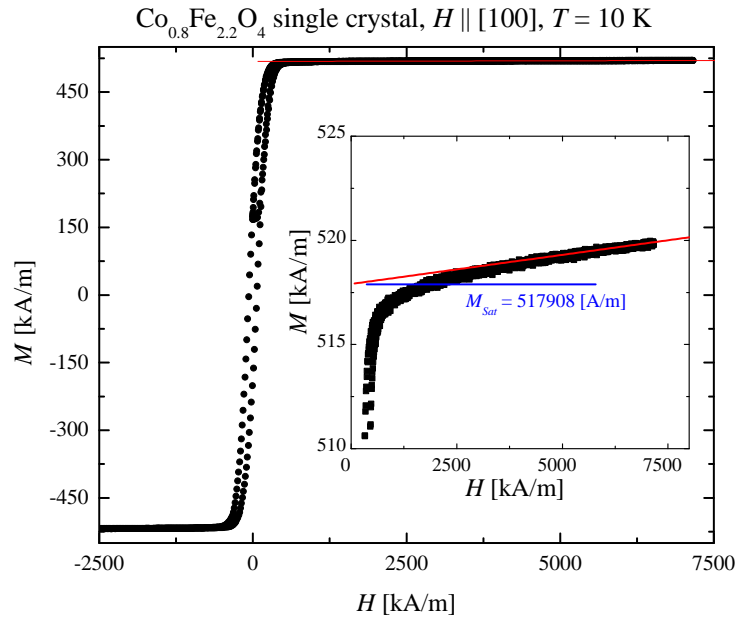


Figure 6.1: Magnetization as function of the applied field at $T = 10$ K along the easy [100] axis of the $\text{Co}_{0.8}\text{Fe}_{2.2}\text{O}_4$ single crystal. The red curve is a fit according to the law of approach to saturation (LAS), while the horizontal blue line denotes the value of the obtained saturation magnetization from LAS.

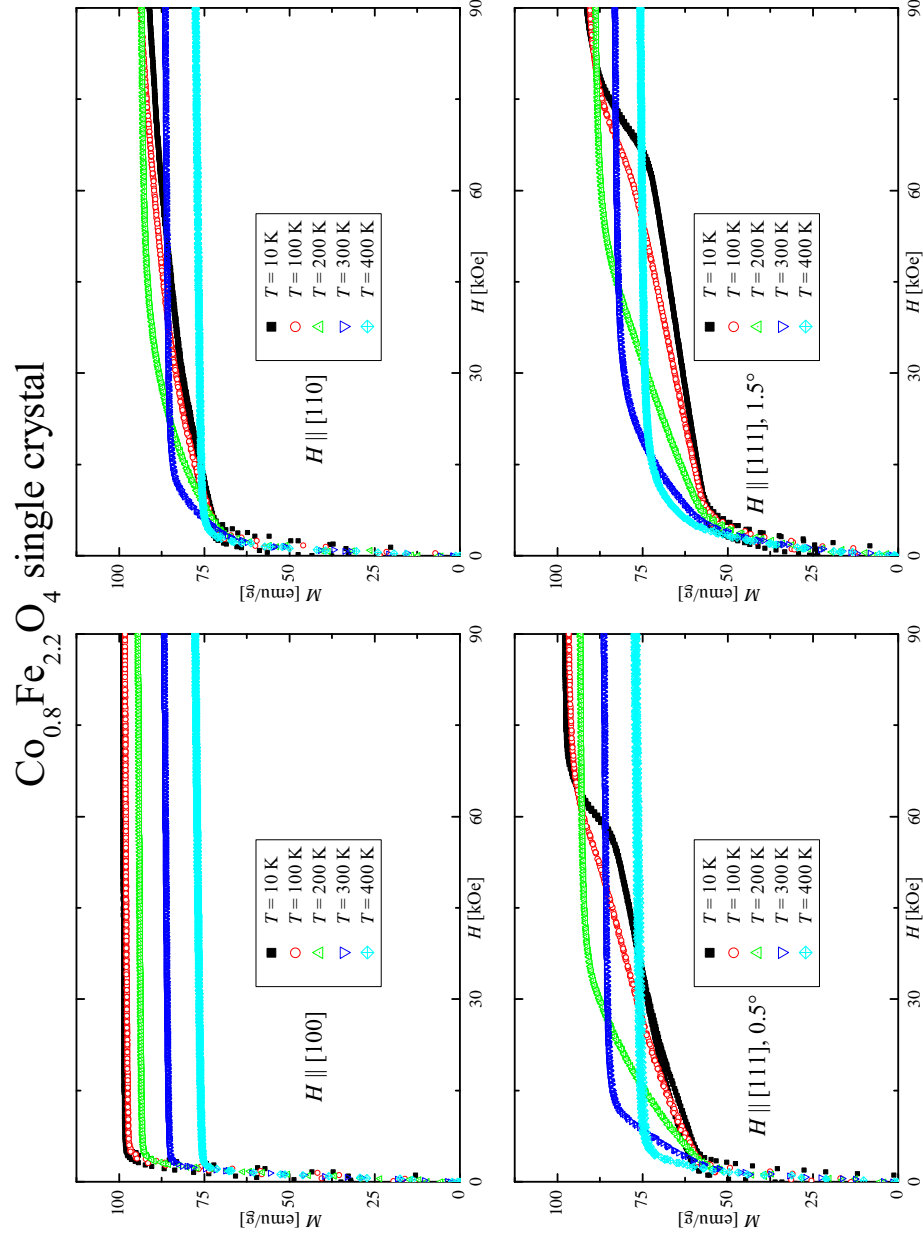


Figure 6.2: Magnetization curves along the main crystal axes of cobalt ferrite: $[100]$, $[110]$ and $[111]$ with 0.5° and 1.5° misalignment.

[100] easy axis

Over the whole temperature range the [100] axis turned out to be the easy axis of magnetization $M(H)$ as can be seen in figure 6.2 on the top, left position, where the magnetization $M(H)$ is plotted for five different temperatures. With the help of the law of approach to saturation (LAS) it was not only possible to determine the exact saturation magnetization of the [100] axis, but also the high field susceptibility κ along the easy axis (see figure 6.10) and the anisotropy constant K_0 as function of temperature (see figure 6.20). In table 6.1 all fit parameters and the resulting anisotropy values are listed. The anisotropy constant K_0 was determined with the help of the fit parameter b according to this empirical formula:

$$K_0 = M_{Sat} \sqrt{b \cdot C}, \quad (6.1)$$

where C is an empirical constant which was found to be 1 in order to fit the K_0 from the integration method with the LAS method. It should be noted that usually only the anisotropy constant K_1 can be determined with the LAS. Following the derivation of formula 2.9 the numerical factor has to be zero, as the magnetization vector has to point along the easy axes of the single crystal even without any magnetic field applied. Nevertheless the inset of figure 6.1 shows the steepness of the magnetization slope and its fit according to the LAS. The blue horizontal line shows the obtained saturation magnetization value M_{Sat} .

The temperature dependence of $K_0(T)$ and a comparison with the integral method is shown in chapter 6.2.1.

Table 6.1: Fit parameters for the law of approach to saturation measured along the [100] axis. K_0 is calculated according to formula 6.1.

T [K]	M_{Sat} [$\frac{A}{m}$]	b [$\frac{m^2}{A^2}$]	κ [1]	K_0 [$\frac{J}{m^3}$]
5	518507	$6.418 \cdot 10^9$	$2.188 \cdot 10^{-4}$	52200
10	517908	$4.326 \cdot 10^9$	$2.793 \cdot 10^{-4}$	42806
25	517770	$1.478 \cdot 10^9$	$3.082 \cdot 10^{-4}$	25013
50	516858	$5.891 \cdot 10^9$	$4.757 \cdot 10^{-4}$	49852
75	515816	$7.014 \cdot 10^9$	$4.626 \cdot 10^{-4}$	54286
100	513197	$9.665 \cdot 10^9$	$4.760 \cdot 10^{-4}$	63400
125	509925	$8.827 \cdot 10^9$	$5.257 \cdot 10^{-4}$	60204
150	505081	$9.640 \cdot 10^9$	$5.493 \cdot 10^{-4}$	62318
175	498880	$1.027 \cdot 10^{10}$	$5.863 \cdot 10^{-4}$	63528
200	491428	$9.423 \cdot 10^9$	$6.229 \cdot 10^{-4}$	59947
225	483111	$9.606 \cdot 10^9$	$6.749 \cdot 10^{-4}$	59502
250	472914	$8.999 \cdot 10^9$	$7.257 \cdot 10^{-4}$	56376
275	462392	$8.679 \cdot 10^9$	$7.886 \cdot 10^{-4}$	54132
300	451055	$7.927 \cdot 10^9$	$8.672 \cdot 10^{-4}$	50465
325	439010	$7.940 \cdot 10^9$	$9.447 \cdot 10^{-4}$	49159
350	426197	$7.409 \cdot 10^9$	$1.030 \cdot 10^{-3}$	46101
375	413352	$8.361 \cdot 10^9$	$1.110 \cdot 10^{-3}$	47497
400	399868	$8.333 \cdot 10^9$	$1.190 \cdot 10^{-3}$	45870
425	383494	$7.983 \cdot 10^9$	$1.160 \cdot 10^{-3}$	43059
450	368331	$1.302 \cdot 10^{10}$	$1.210 \cdot 10^{-3}$	52817
475	352165	$9.093 \cdot 10^9$	$1.370 \cdot 10^{-3}$	42199
500	336328	$1.373 \cdot 10^{10}$	$1.390 \cdot 10^{-3}$	49520
525	319318	$1.190 \cdot 10^{10}$	$1.530 \cdot 10^{-3}$	43779
550	302378	$1.320 \cdot 10^{10}$	$1.610 \cdot 10^{-3}$	43663
575	283982	$1.370 \cdot 10^{10}$	$1.740 \cdot 10^{-3}$	41763
600	266078	$1.851 \cdot 10^{10}$	$1.810 \cdot 10^{-3}$	45491
625	247493	$1.450 \cdot 10^{10}$	$1.910 \cdot 10^{-3}$	37446
650	230789	$2.085 \cdot 10^{10}$	$1.990 \cdot 10^{-3}$	41873
675	216344	$2.470 \cdot 10^{10}$	$1.950 \cdot 10^{-3}$	42726
700	198988	$2.984 \cdot 10^{10}$	$2.040 \cdot 10^{-3}$	43192
725	174502	$4.584 \cdot 10^{10}$	$2.330 \cdot 10^{-3}$	46950
750	142796	$8.941 \cdot 10^{10}$	$2.930 \cdot 10^{-3}$	53658
775	96144	$3.574 \cdot 10^{11}$	$4.450 \cdot 10^{-3}$	72230
787.5	65690	$1.051 \cdot 10^{12}$	$5.730 \cdot 10^{-3}$	84609
800	27805	$2.174 \cdot 10^{12}$	$7.400 \cdot 10^{-3}$	51516
812.5	7696	$2.481 \cdot 10^{12}$	$6.640 \cdot 10^{-3}$	15236
825	2227	$2.507 \cdot 10^{12}$	$5.450 \cdot 10^{-3}$	4432
837.5	845.6	$1.805 \cdot 10^{12}$	$4.480 \cdot 10^{-3}$	1428
850	464.1	$9.692 \cdot 10^{11}$	$3.820 \cdot 10^{-3}$	574

In figure 6.3 the saturation magnetization of the [100] axis is plotted as function of the temperature for the low and high temperature measurement. In the low-temperature region up to $\sim 0.3 \cdot T_C$ [0 - 225 K] the sample obeys the spin wave theory, which means that the saturation magnetization follows the modified Bloch Law [33, 63]:

$$M_{Sat}(T) = M_{Sat}(0K) \left(1 - B \cdot T^{\frac{3}{2}} - C \cdot T^{\frac{5}{2}} \cdot e^{\frac{-E_G}{k_B T}} \right), \quad (6.2)$$

with $M_{Sat}(0K) = 518194 \frac{A}{m}$, $B = 4.07 \cdot 10^{-6} K^{-\frac{3}{2}}$, $C = 8.71 \cdot 10^{-8} K^{-\frac{5}{2}}$ and the energy gap along the measured crystallographic direction $E_G = 3.78 \text{ meV}$. A fit of the saturation magnetization of the polycrystalline sample with the Bloch Law could not be performed, as it is not possible to saturate the sample with 90 kOe. Franco and co-workers [64] could however apply a stronger magnetic field and obtained for nanocrystalline (crystallite size $\sim 42 \text{ nm}$) cobalt ferrite a value for $B = 2.35 \cdot 10^{-5} K^{-\frac{3}{2}}$ with $C = 0$.

For the high temperature range [300 - 800 K] the saturation magnetization $M_{Sat}(T)$ follows a general scaling law, which was also used for determining the Curie-temperature T_C (see chapter 6.1.4):

$$M_{Sat}(T) = M_{Sat}(0K) \left(1 - \frac{T}{T_C} \right)^n, \quad (6.3)$$

with $n = 0.557$, $T_C = 807.6 \text{ K}$ and $M_{Sat}(0K) = 581.6 \frac{kA}{m}$. The fit parameter n points to an isotropic molecular field model ($n = 0.5$). When extrapolating to temperatures below $T = 300 \text{ K}$, it is clearly visible that the scaling law fails to describe the saturation magnetization and produces much too high values for the saturation magnetization, as can be seen in figure 6.3.

[110] intermediate axis

The saturation magnetization along the [110] axis in a cubic environment is only dependent on the first anisotropy constant K_1 . The magnetic field value where the sample reaches a magnetically saturated state is called the anisotropy field $H_A = \frac{2K_1}{M_{Sat}}$. In chapter 3 the magnetization process

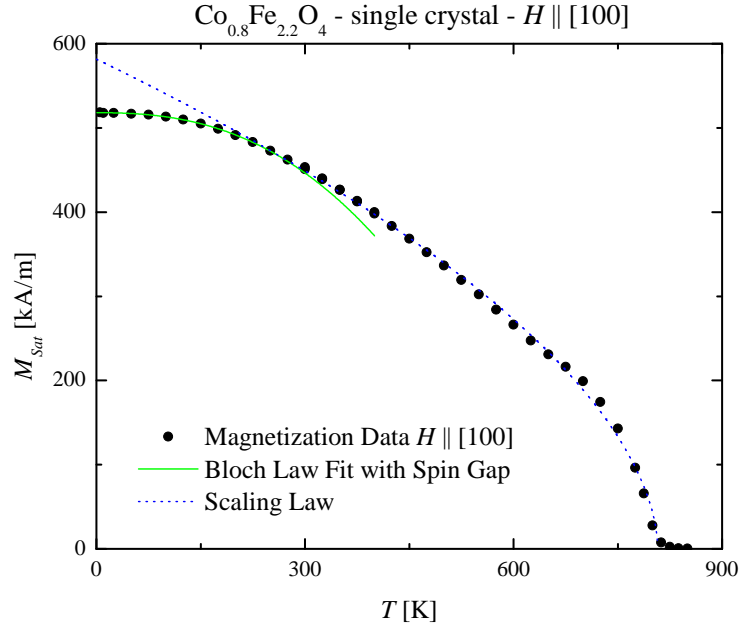


Figure 6.3: Temperature dependence of saturation magnetization of single crystalline cobalt ferrite measured along the easy $[100]$ axis.

along $[110]$ was calculated and its independence of K_2 was proven (see formula 3.6). From the upper, right magnetization curve in figure 6.2, it can be learned that below $T = 150$ K saturation can no longer be reached by applying a magnetic field of 90 kOe. In 1988 Guillot and co-workers found out that at $T = 4.2$ K a magnetic field of 170 kOe is necessary to saturate cobalt ferrite [26]. K_1 can therefore only be determined when the magnetization data are extrapolated, which is discussed in more detail in chapter 6.2.1.

$[111]$ hard axis

Below $T = 150$ K a jump in the magnetization along the $[111]$ axis is visible, as shown in the bottom, left figure 6.2. The critical field, where the jump

occurs is very sensitive to the alignment of the $[111]$ axis with respect to the magnetic field. As the single crystal was first aligned with Laue and then glued to the VSM sample holder, a small misalignment error may occur. The deviation from the $[111]$ axis was determined with a linear fit in the low field range $[6 - 22\text{kOe}]$ and an extrapolation to zero field. As the magnetization vector lies in the $[100]$ axis, the projection to the $[111]$ axis is $\frac{1}{\sqrt{3}}$, which should correspond to the obtained offset from the linear fit. This offset was also analyzed as function of temperature, as shown in figure 6.4, where the relative magnetization is plotted as function of the temperature. All data were normalized against the saturation magnetization of the $[100]$ axis obtained from the law of approach to saturation (see table 6.1). It can be clearly seen that the magnetization follows our geometric considerations up to 250 K as the value of $\frac{1}{\sqrt{3}}$ is held quite constant over a broad temperature range.

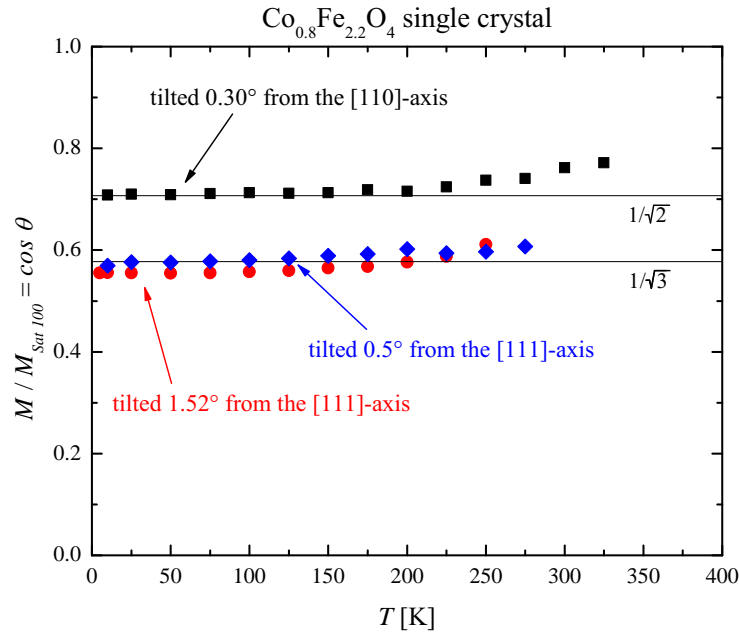


Figure 6.4: Offset of the linear fit in the low field region of the normalized magnetization as function of temperature.

For the first measurements an alignment error of 1.5° off the $[111]$ axis (see figure 6.2 on the bottom right) was achieved, which causes an increase of the FOMP-field to 70 kOe. These magnetization measurements were published in [65]. A later measurement reduced the misalignment to 0.5° resulting in a FOMP-field of 60 kOe (see figure 6.2 on the bottom left). The magnetostriction measurements apparently did not show any misalignment and the FOMP-field H_{FOMP} decreased to 55 kOe [65]. In figure 6.5 these data are plotted at a temperature of $T = 10\text{K}$. A quite linear behavior between the deviation angle and the critical field is observed.

However it should be noted that the higher misalignment of the sample is, the more tends the measurement to behave like a $[110]$ measurement above the FOMP-field, whereas the measurement with lower misalignment angle behaves like a $[100]$ measurement. This behavior is clearly seen in figure 6.2 in the two bottom figures. Moreover it is visible in the magnetization

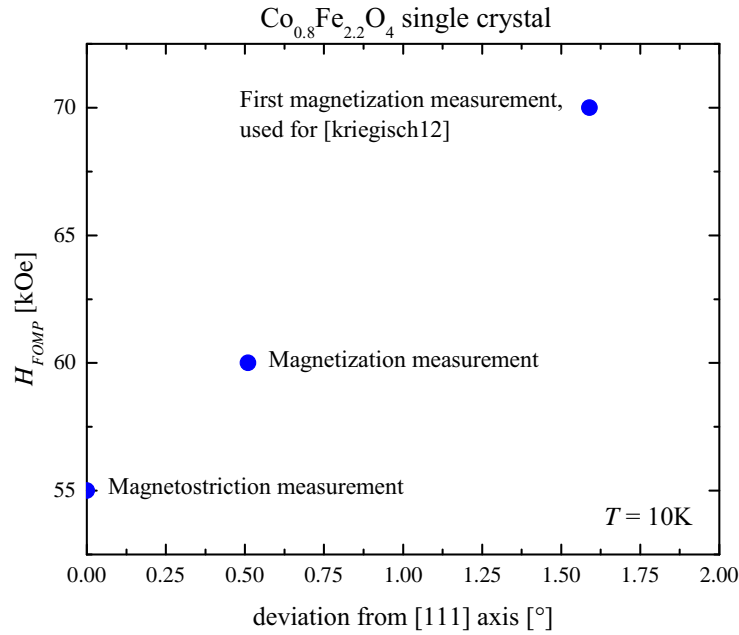


Figure 6.5: Change of the critical FOMP field with the deviation angle from the $[111]$ axis.

calculation in chapter 3, where no misalignment was considered and the magnetization vector jumps over the energy barrier and reaches immediately the saturation magnetization (which is also seen in figure 6.2 on the bottom left).

6.1.2 Magnetization of a Polycrystalline Sample

In the polycrystalline sample it can be assumed that small crystallites are isotropically and completely randomly distributed, as no texture was seen in XRD. So the easy [100], the intermediate [110] and the hard [111] axis characteristics are superimposed. Figure 6.6 shows the signal to noise ratio $\frac{(dM/dH)}{M}$ of the three main crystal axes of the single crystal at $T = 10$ K. The [100] axis measurement saturates fastest, which can be seen in the normalized derivative as noise around zero. This noise amplitude can be seen as the characteristic for the measurement setup. Whereas the [110] axis

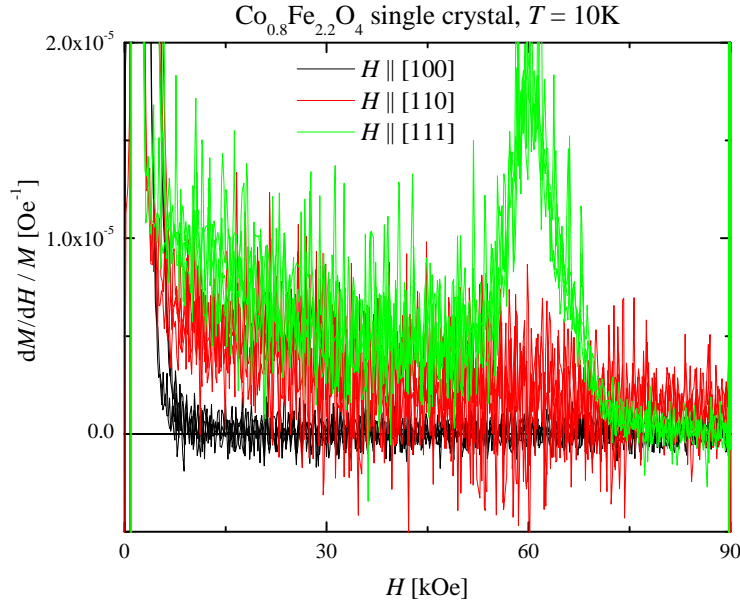


Figure 6.6: Normalized Signal to Noise ratio of the magnetization of the single crystalline sample at $T = 10$ K.

measurement is asymptotically approaching to zero with a much higher noise amplitude. The smaller system inherent noise amplitude will be reached saturation. This is reflected in the magnetization as well, where the saturation at $T = 10\text{ K}$ is not reached below $H = 170\text{ kOe}$ along $[110]$ according to [26]. In the normalized derivative of the magnetization measurement along the $[111]$ axis the FOMP is seen very prominently around $H = 60\text{ kOe}$. It is remarkable that below the FOMP field, the noise amplitude is roughly of the same order of magnitude as the $[110]$ axis measurement, whereas above the FOMP the noise amplitude reduces to the value as found for the $[100]$ axis. This is not surprising, as a similar behavior is found in the magnetization curve. The order of the magnitude of the noise points to local stresses and small rotation processes of the magnetization vector against the magnetocrystalline anisotropy. In the $[110]$ and the $[111]$ axis below the FOMP, the magnetization vector has to work against the magnetocrystalline anisotropy energy E_A . Along the easy $[100]$ axis no work against E_A has to be performed, therefore the noise amplitude is smaller, as it reflects the

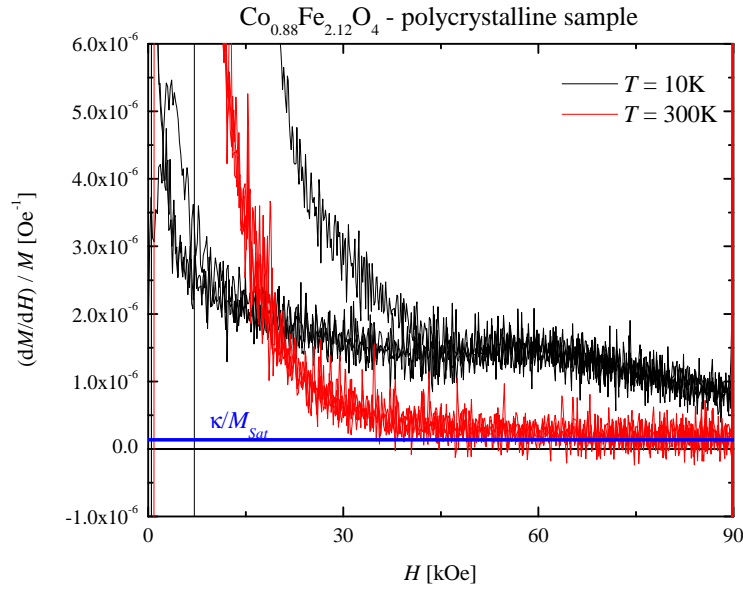


Figure 6.7: Normalized Signal to Noise ratio of the magnetization of the polycrystalline sample at $T = 10\text{ K}$ and $T = 300\text{ K}$.

inherent noise of the measurement setup. As the magnetization vector has passed the energy barrier above the FOMP, the noise level has to get smaller along the $[111]$ axis.

It is noteworthy that the amplitude of the noise depends on the field sweep rate change. As all samples were measured with the same field sweep rate, we can deduce from these measurements that the noise amplitude can deliver valuable information about the rate of changing the magnetic state of this type of sample. This knowledge can also be checked on a polycrystalline cobalt ferrite sample. In figure 6.7 the FOMP from the particles aligned parallel to the $[111]$ axis is visible as well as the steady increase of the magnetization from the $[110]$ axis oriented particles. The features of these two axes are both present, but of course not as strongly pronounced as it is in the single crystal. While at low temperature saturation can not be reached, at $T = 300\text{ K}$ the average value of the normalized derivative of the measured magnetization is approaching the value of $\frac{\kappa}{M_{Sat}}$ asymptotically.

6.1.3 Degree of Inversion

The degree of inversion was determined for the single crystal and with the help of an extrapolation also for the polycrystal. As it denotes the cation distribution of the spinel (see chapter 2.3.2), the degree of inversion is calculated using the saturation magnetization at $T = 0\text{ K}$. Due to the very high ordering temperature of cobalt ferrite ($T_C \sim 800\text{ K}$), it is also possible to take the saturation magnetization value at $T = 5\text{ K}$. In figure 6.8 the saturation magnetization obtained from the law of approach to saturation of the single crystal and the polycrystal are shown as function of temperature. The magnetization of the single crystal was measured along the easy $[100]$ axis, giving a saturation magnetization value at $T = 5\text{ K}$ of $\mu_{eff} = 4.13\mu_B$ per formula unit (*f.u.*). Due to the high magnetic anisotropy it was not possible to saturate the polycrystalline sample below $T < 150\text{ K}$ with 90 kOe . Therefore the saturation magnetization appears to decrease below $T < 150\text{ K}$, which definitely does not reflect the real behaviour of the saturation magnetization. As a consequence, the saturation magnetization

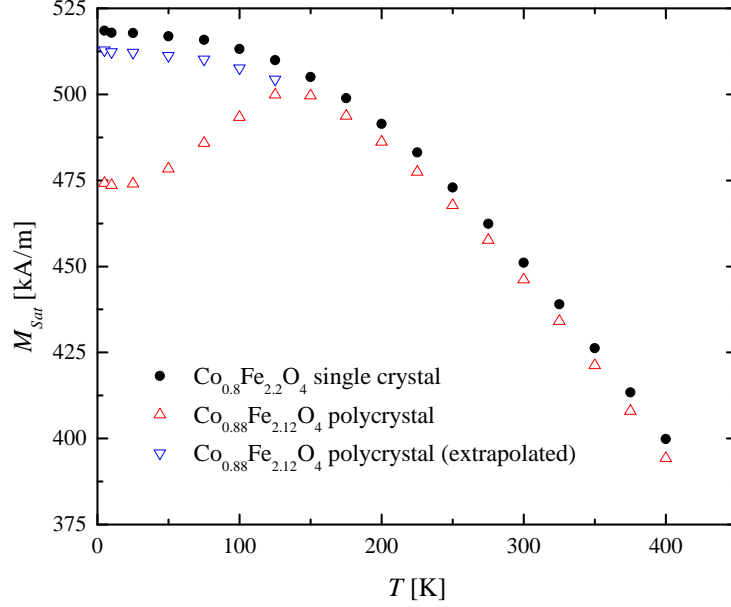


Figure 6.8: Saturation Magnetization obtained from the law of approach to saturation of the single crystal and the polycrystal.

of the polycrystal was extrapolated with the data obtained from the single crystal, yielding in a magnetic moment of $\mu_{eff} = 4.09 \frac{\mu_B}{f.u.}$ at $T = 5$ K.

For a further analysis on the inversion three parameters have to be known: the measured low temperature effective magnetic moment μ_{eff} , the effective moments of all ions involved (see table 2.1) and the sum formula. For the single crystal the sum formula is given by $(Co_{0.8-i}^{2+}Fe_{0.2+i}^{3+})[Co_i^{2+}Fe_{0.2}^{2+}Fe_{1.8+i}^{3+}]O_4^{2-}$ leading to an effective moment $\mu_{eff} = \mu_{B-Sites} - \mu_{A-Sites} = 4.13 \mu_B$. The degree of inversion $i = 0.783$ results from computing the effective magnetic moments of the A and B-sites with the experimental values μ_{exp} of the magnetic ions from table 2.1¹. As i can vary between 0 and 0.8 the spinel is nearly completely inverse. The resulting sum formula is calculated to: $(Co_{0.0137}^{2+}Fe_{0.9863}^{3+})[Co_{0.7863}^{2+}Fe_{0.2}^{2+}Fe_{1.0137}^{3+}]O_4^{2-}$.

The sum formula for the polycrystal differs but the calculation stays in prin-

¹Unfortunately the Fe^{2+} ions were not taken into account for calculating the degree of inversion in the first paper on cobalt ferrite [65].

ciple the same: $(Co_{0.88-i}^{2+}Fe_{0.12+i}^{3+})[Co_i^{2+}Fe_{0.12}^{2+}Fe_{1.88+i}^{3+}]O_4^{2-}$. With an effective moment of $\mu_{eff} = 4.09 \mu_B$ the degree of inversion is determined to $i = 0.494$ which yields in the sum formula $(Co_{0.386}^{2+}Fe_{0.614}^{3+})[Co_{0.494}^{2+}Fe_{0.12}^{2+}Fe_{1.386}^{3+}]O_4^{2-}$. While the single crystal seems to be inverse, the polycrystal is definitely a mixed spinel. Approximately 44% of the cobalt ions are sitting in the tetrahedral site and 56% in the octahedral site. This is not surprising as the polycrystalline sample was annealed at $T = 1000^\circ\text{C}$, while the single crystal was exposed to higher temperature $T = 1370^\circ\text{C}$. Although there is approximately 10% more cobalt in the polycrystalline compound, the magnetic moment is 1% lower due to the mixed cation distribution.

6.1.4 Curie Temperature

The Curie Temperature T_C of the polycrystalline and the single crystalline sample was determined from magnetization measurements with four different methods.

Maximum in high field susceptibility - LAS κ

When measuring the initial magnetic susceptibility of a ferromagnetic material it is known that a peak is observed close to the Curie-Temperature. For the low field or initial susceptibility this peak is called the Hopkinson-Peak and the effect is referred to the Hopkinson-Effect [35, 66]. For the high field susceptibility κ this effect can be described with Langevin theory and the Weiss molecular field theory (see chapter 2.2.2).

For our polycrystalline sample we employed the law of approach to saturation (see chapter 2) throughout the whole measured temperature range [5 - 850 K]. The temperature dependence of the high field susceptibility κ is shown in figure 6.9. Clearly one can see the maximum around $T_C = 815\text{ K}$ and the linear rise of κ with temperature in an intermediate range. The linear fit was performed from 150 to 650 K. The upper limit of the fit is

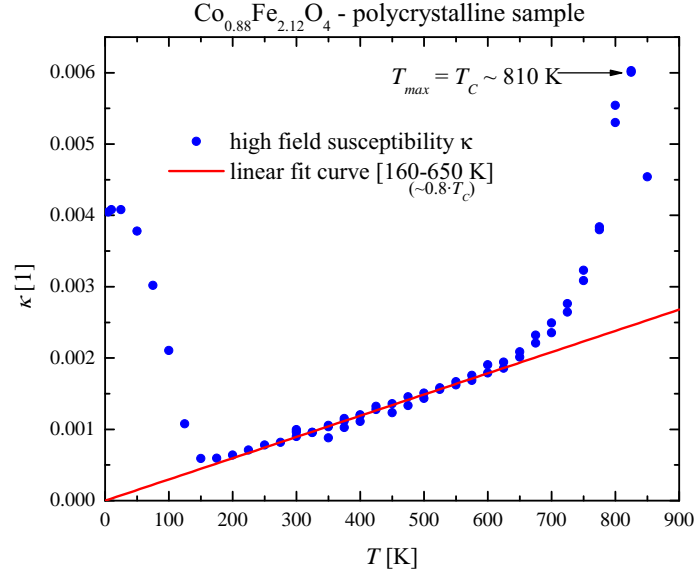


Figure 6.9: Temperature dependence of high field susceptibility κ of polycrystalline cobalt ferrite. Below $T = 150 \text{ K}$ the prerequisites for the law of approach to saturation is no longer fulfilled, which results in a physically unlikely increase of κ .

given by the rule of thumb that most temperature dependent fits are valid below $0.8 \cdot T_C$, whereas the lower limit (150 K) is given by the fact that the law of approach to saturation is not longer valid, as the sample can not be saturated by the maximum available field of 90 kOe of the superconducting coil inside our cryostat. A more detailed discussion on the validity of the law of approach to saturation is given in chapter 2.

For the single crystal the easy [100] axis was chosen to measure the magnetization from 5 to 850 K. The law of approach to saturation was employed here as well to determine the saturation magnetization M_{Sat} and the high field susceptibility κ . In figure 6.10 the temperature dependence of κ is plotted as function of temperature. The linear fit was performed as well in the temperature range of 150 to 650 K. At $T = 803.7 \text{ K}$ the maximum in the high field susceptibility is clearly visible. The slopes of the two linear fit curves are very similar: The slope for the polycrystalline sample is $2.926 \cdot 10^{-6}$

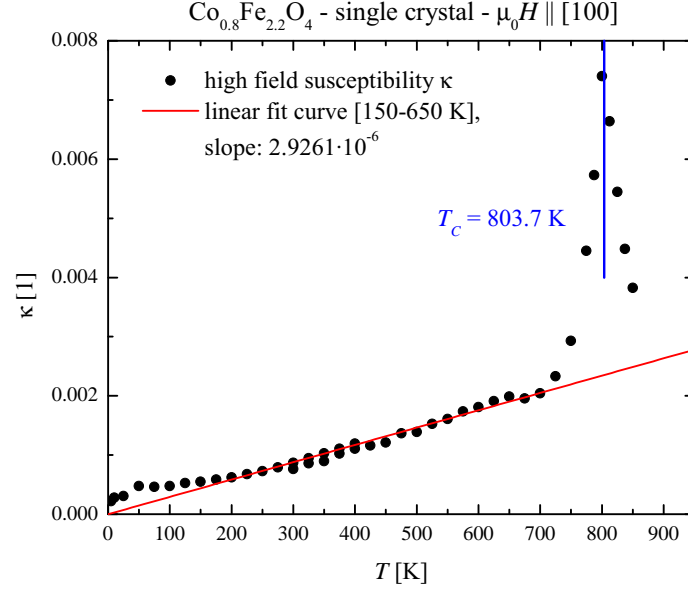


Figure 6.10: Temperature dependence of the high field susceptibility κ along the $[100]$ axis of single crystalline cobalt ferrite.

$[\text{K}^{-1}]$ and for the single crystal $2.976 \cdot 10^{-6} [\text{K}^{-1}]$. The deviation of the slopes is only 1.7%.

$\frac{H}{M}$ versus M^2

When plotting a set of isothermal inverse susceptibility $\frac{H}{M}$ curves versus the magnetization squared M^2 around T_C , one can fit the resulting curves with a straight line. The offset on the $\frac{H}{M}$ -axis is zero for $T = T_C$. This theory was developed by [67] and is widely used for example by [68, 69]. In figures 6.11 and 6.12 the results of this analysis are shown for the polycrystalline sample leading to $T_C = 788 \text{ K}$ and for the single-crystalline sample leading to $T_C = 782 \text{ K}$. In the inset of the figures 6.11 and 6.12 the offset of the susceptibility is plotted against the temperature.

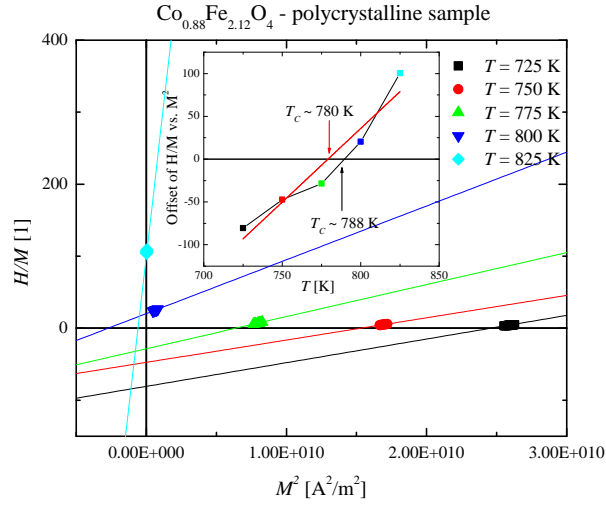


Figure 6.11: A set of isothermal inverse susceptibilities versus M^2 of polycrystalline cobalt ferrite.

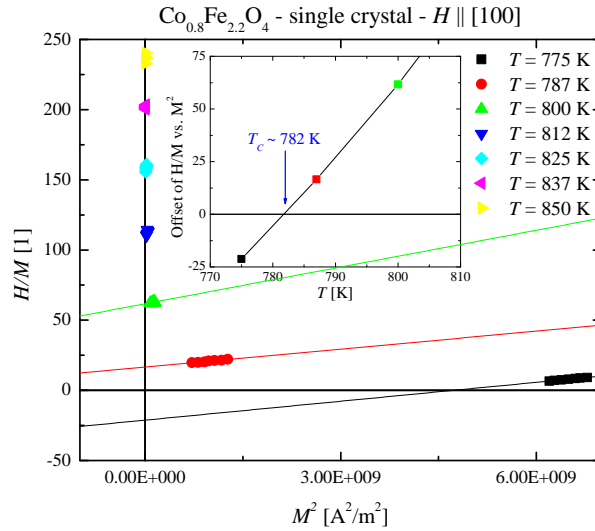


Figure 6.12: A set of isothermal inverse susceptibilities versus M^2 , measured along the $[100]$ axis of single crystalline cobalt ferrite.

Scaling Law

It is seen very often that temperature dependent measurement quantities like the saturation magnetization M_{Sat} , magnetic anisotropy constants or magnetostriction constants are plotted against the reduced temperature $\frac{T}{T_C}$. As [69] is summing up, one reason is to determine critical exponents in order to check the physical origin of the magnetic quantities and to test theoretical predictions concerning phase transitions. Another reason is simply to provide an easy relation for further simulations with the help of such empirical plots.

The power law used here for the polycrystalline and the single crystalline samples is the scaling law for the saturation magnetization (see formula 6.3). The critical exponent n , as well as the other parameters $M_{Sat}(0K)$ and T_C were left free for the fitting procedure. The range for these fits was extended from 150 to 775 K for the polycrystalline (see figure 6.13) and from zero to

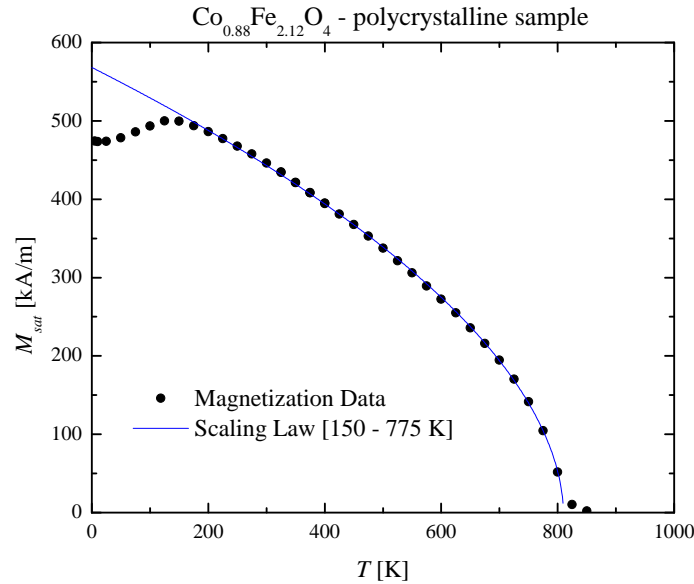


Figure 6.13: Temperature dependence of saturation magnetization of polycrystalline cobalt ferrite. Below $T = 150$ K the law of approach to saturation is no longer applicable, which results in an decrease of M_{Sat} .

800 K for the single crystalline sample (see figure 6.3). The obtained value for n is 0.557 for the polycrystalline and 0.543 for the single crystalline sample, which points to an isotropic molecular field model ($n = 0.5$). The values for the saturation magnetization for both samples were far too high and therefore dismissed. The values given from the law of approach to saturation were used for further analysis. The temperature range has to be limited to values above 150 K, as will be discussed in chapter 6.2.2. The values of T_C were determined for the polycrystalline to $T_C = 809$ K and single-crystalline sample to $T_C = 803.6$ K.

M versus T

The last method is quite similar to the high field susceptibility, although with reduced magnetic field. When looking at the magnetization at a small constant field, the temperature where the curvature of the magnetization

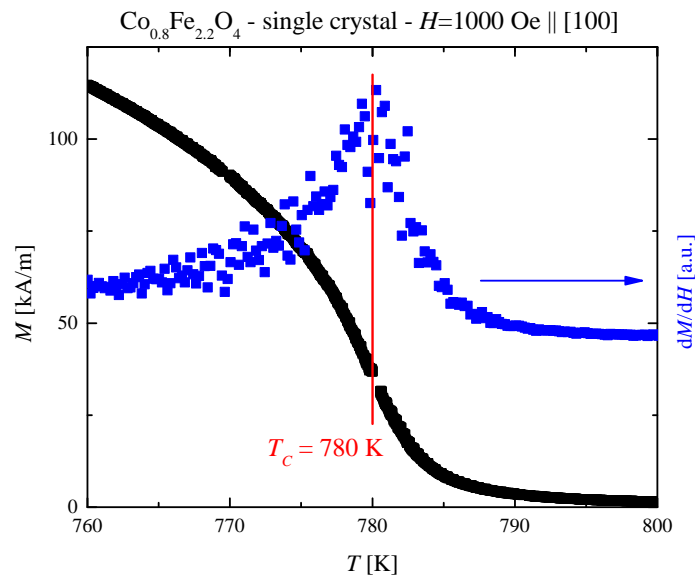


Figure 6.14: First derivative of magnetization measurement along the [100] axis of single crystalline cobalt ferrite.

curve is changing, is considered as Curie temperature. Therefore it is necessary to calculate the first derivative of the magnetization. In figure 6.14 the change in the magnetization curve is shown. The derivative is plotted in blue as second axis. The values of T_C were determined for the polycrystalline sample to $T_C = 790$ K and single-crystalline sample to $T_C = 780$ K.

Results and Discussion

In table 6.2 the results for T_C using all four methods are shown. Very remarkable is the fact that the deviations tends to be the same for each method. While the “LAS- κ ” and the “Scaling Law” produce a higher T_C , the “ $\frac{H}{M}$ vs. M^2 ” and “M vs. T” method produce a lower T_C . The reason for this behaviour is found in the fact that the “LAS- κ ” method and the “Scaling Law” use high-field data and the high external magnetic field supports magnetic order and shifts therefore the Curie temperature up. Whereas T_C determined with low field methods should give more correct values, as this second order phase transition is defined without external magnetic field. Therefore the mean value of the low field methods is used as Curie-Temperature, which delivers $T_C = 789$ K for the polycrystalline sample and $T_C = 781$ K for the single-crystalline sample.

Although the investigated sample of Fayek and co-workers has the same Co concentration $x = 0.8$, T_C is higher than our obtained value [70]. It is important to consider that T_C was determined with Mössbauer method, which is

Table 6.2: Curie Temperatures obtained by various methods for poly- and single-crystalline sample

	polycrystalline	single crystal
Co concentration x	0.88	0.8
Method	T_C [K]	T_C [K]
LAS- κ	815	803.7
$\frac{H}{M}$ vs. M^2	788	782
Scaling Law	809	803.6
M vs. T	790	780

very sensitive to short range order and tends to produce higher T_C values. Moreover it has to be mentioned that the dependence of the Curie-Temperature on the Co-ratio shows a different trend according to the work of Persoons [71], who used Mössbauer method as well. In figure 6.15 the mean value of the two low field methods Curie-Temperature is plotted together with literature data.

The general difference of the Curie temperature for the polycrystalline and single-crystalline samples might arise from the different composition and from the degree of inversion of the samples. Depending on their prior heat treatment the degree of inversion can be easily changed which affects T_C as well.

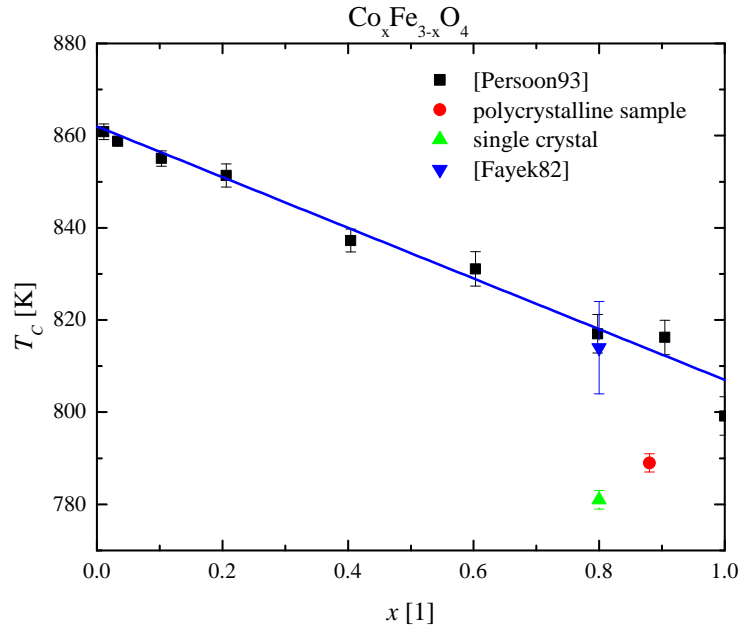


Figure 6.15: Variation of the Curie-temperature with cobalt content x for poly- and single-crystalline cobalt ferrite $\text{Co}_x\text{Fe}_{3-x}\text{O}_4$.

6.2 Magnetic Anisotropy

6.2.1 Magnetic Anisotropy: Single Crystal

The magnetic anisotropy of the single crystal was determined first with the integral method as described in chapter 3 and second from the FOMP and saturation field.

One of the prerequisites for the integration method is the magnetic full saturation of the sample. In figure 6.16 the magnetization at $T = 10$ K is plotted as function of the magnetic field (filled symbols). It can be clearly seen, that the sample is not saturated up to the maximum available field of 90 kOe. Therefore the magnetization data along the [100] and [110] axes were fitted with a linear function in the range from 70 to 90 kOe and extrapolated. The [111] axis was fitted between 80 to 90 kOe and extrapolated to high field values as well. The saturation field was determined as the point where the intermediate [110] axis meets the easy [100] axis. This linear fit procedure was necessary for all measurements below $T = 175$ K.

The values of the saturation field H_{Sat} is shown in figure 6.17. The red, square symbols denote the measured saturation field, whereas the blue, round symbols are derived from the extrapolated crossing point of the intermediate with the easy axes. The purple line shows the maximum magnetic field limit which can be applied by the superconducting coil inside the cryostat. The diamond shaped symbols are digitized from [26] and represent measured data. Overall, the excellent agreement of the extrapolated data with the measurements leads to the conclusion that the assumption for the linear extrapolation proves to be justified.

In figure 6.18 the integrated area $\int_0^{H_{Sat}} H dM$ (see formula 3.10) along the main crystallographic directions is plotted as function of the upper integration limit. The open symbols refer to literature data [26] and the purple line shows the maximum applicable magnetic field. The values of saturation magnetization at 4.2 and 10 K are practically the same, due to the very high ordering temperature ($T_C \sim 800$ K). Starting with the integrated data of the magnetization along the [100] axis, it is remarkable that the integration area differs nearly a factor of 2 with the data obtained

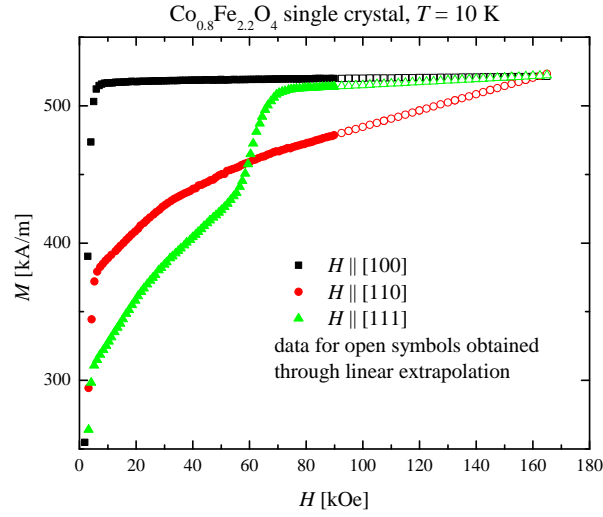


Figure 6.16: Magnetization measurement of the $\text{Co}_{0.8}\text{Fe}_{2.2}\text{O}_4$ single crystal at $T = 10$ K with linear extrapolation data.

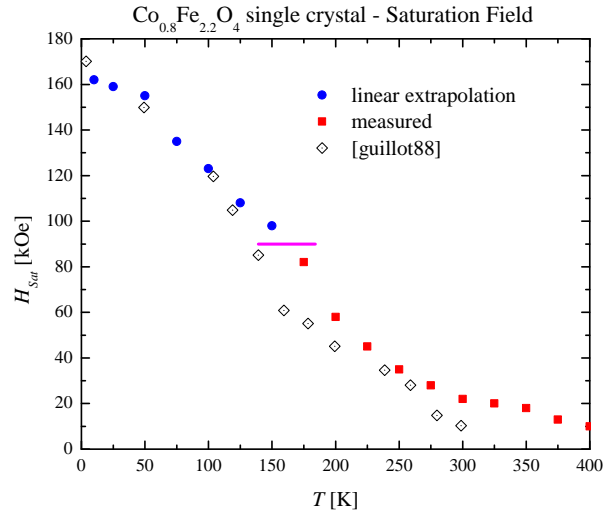


Figure 6.17: Saturation field H_{Sat} along the $[110]$ axis as function of temperature for cobalt ferrite. The diamond shaped symbols were digitized from [26].

from [26]. As this area corresponds to K_0 , this difference is significant. Moreover K_0 can be seen as a measure for the quality of a single crystal, as dislocations, impurities and internal stress affect the magnetization measurement and increases the value of K_0 (see chapter 3). This can be seen as an indicator that our sample has fewer dislocations and less internal stress. The integration values for the intermediate axes are similar within an uncertainty of the measurement error. Both curves are increasing until they reach the saturation field H_{Sat} , which lies around 160 kOe at low temperatures. The green, filled triangles are the integration results of the 1.5° misaligned $[111]$ axis (used for publication in [65]). After the FOMP, which is visible in a huge step around 70 kOe, the magnetization curve approaches the $[110]$ axis (see figure 6.2 bottom, right), resulting in an steady increase of the corresponding integrated area. With these values a far too high integration area is obtained which results in a high positive K_2 published in [65]. When aligning the sample more carefully (0.5° from the

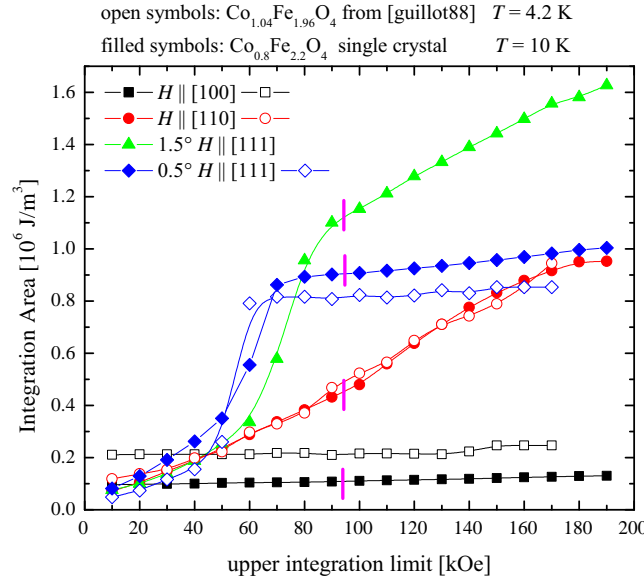


Figure 6.18: Magnetization integration values as function of the upper integration limit and the comparison of the integration areas with literature values. The open symbols were digitized from [26].

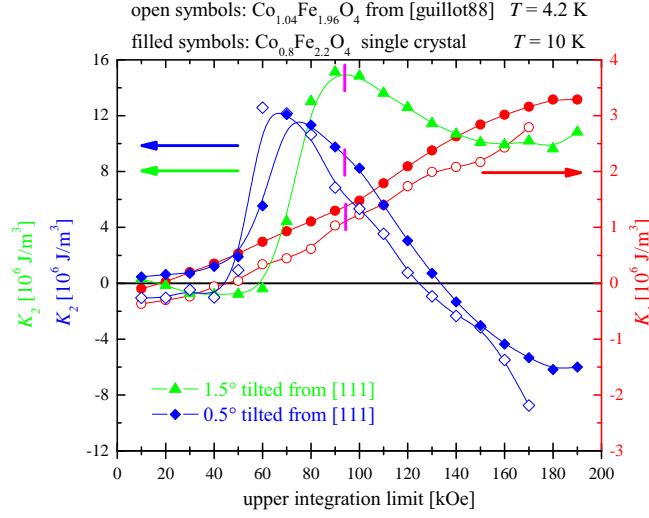


Figure 6.19: Magnetic anisotropy constants as function of the upper integration limit and the comparison with literature values. The open symbols were digitized from [26].

[111] axis) a more accurate measurement is possible (see figure 6.2 bottom, left). The diamond shaped symbols show the FOMP at a lower field values of approximately 60 kOe and the integrated values of the area is saturating as well.

With this area a negative K_2 is obtained, as can be seen in figure 6.19. For the integral method it is very important to have the crystallographic axes perfectly aligned when measuring the magnetization. With a small misalignment, a huge change in the integrated values can occur, which leads in our case to a change of sign of the anisotropy constants. This behavior is observed in literature as well [3]. Overall our measured data are in good agreement with the digitized data from [26].

K_0 - a measure of the quality of the single crystal

The anisotropy constant K_0 was determined in two ways: First by fitting with the law of approach to saturation (LAS) and evaluating the

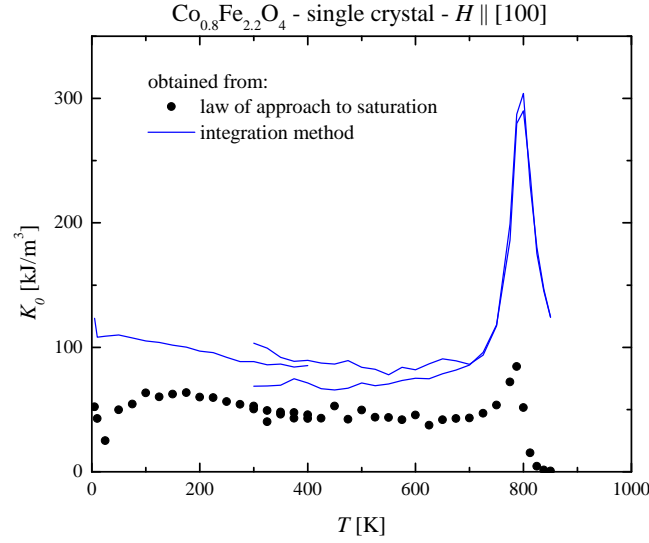


Figure 6.20: Magnetic anisotropy constant K_0 as function temperature obtained by two different methods.

fit parameters with the empirical formula 6.1 and second by using the integration method as can be seen in figure 6.20. The symbols represent the fits in the high field region with the law of approach to saturation. In comparison with the obtained values from the integration method, they are nearly half of the integration values. As the external field was used for the integration method, the values for K_0 are nearly double the real values, as will be shown in chapter 6.2.4. Nevertheless, K_0 is nearly constant over the whole temperature range [10 - 700 K], until the quite sharp increase around the Curie-Temperature T_C which is discussed in more detail in chapter 2.2.2. Above T_C , K_0 is decreasing to zero, as the sample is no longer ferrimagnetically ordered. A direct comparison at low temperature with the data from [26] is plotted in figure 6.18 (open and closed square shaped symbols), where the values of [26] are nearly double in comparison with the integration method.

K_1 - first anisotropy constant

The anisotropy constant K_1 is plotted in figure 6.21 as function of temperature. As the saturation field is increasing with decreasing temperature (see figure 6.17), it exceeds the maximum field limit of 90 kOe, resulting in too low values of K_1 (black, filled square symbols green, open triangular symbols). The overall difference e.g. at room temperature between the polycrystalline and single-crystalline sample might arise due to the different degree of inversion. Whereas the completely inversed spinel (single crystal) has a lower anisotropy constant, the mixed spinel (polycrystal) has a nearly doubled anisotropy constant K_1 . The red, filled circle symbols show the correct evolution of K_1 with temperature, when the magnetization is extrapolated as described in the previous chapter. An additional calculation of K_1 was performed with the help of the saturation or anisotropy field $H_{Sat} = H_A = \frac{2K_1}{M_{Sat}}$ along the [110] axis, which is presented by the blue, hexagonal symbols. The

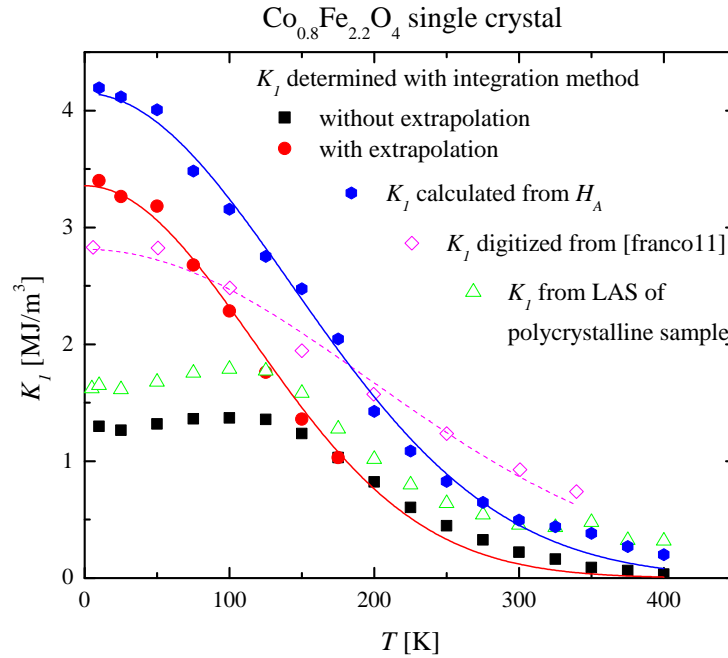


Figure 6.21: Magnetic anisotropy constant K_1 as function of temperature.

red and blue solid lines represent fits according to the empirical Brühkatov-Kirensky fit [72, 73]:

$$K_1(T) = K_1(0) \cdot e^{-\alpha T^2}, \quad (6.4)$$

where $K_1(0)$ is the anisotropy constant at $T = 0$ K and α is an empirical constant. The obtained values for the fits are shown in table 6.3 together with literature values. Unfortunately it is very hard to find reliable, temperature dependent literature data to compare with the obtained results.

Various models were tried for describing the temperature dependence of the anisotropy constants K_1 and K_2 [74, 75, 76, 17], but only the purely phenomenological Brühkatov-Kirensky formula can describe the measured data $K_1(T)$ and $K_2(T)$ over the whole temperature range [72, 73]. The reason here is that no simple theoretical model allows to calculate and describe the origin of K_1 and K_2 . Therefore no analytical formula exists for the temperature dependence of the anisotropy constants.

Table 6.3: Results of Brühkatov-Kirensky fits of the first order anisotropy constant of cobalt ferrite in comparison with literature values.

$K_1(0)$ [$\frac{J}{m^3}$]	α [K^{-2}]	Temperature Range [K]	Source
$1.96 \cdot 10^7$	$1.90 \cdot 10^{-5}$	[20-325]	[19]
$5.20 \cdot 10^6$	$3.27 \cdot 10^{-6}$	[300-825]	[77], nanocrystalline
$2.81 \cdot 10^6$	$1.31 \cdot 10^{-5}$	[4.2-340]	digitized and fitted from [64]
$3.35 \cdot 10^6$	$3.61 \cdot 10^{-5}$	[10-400]	integration method
$4.15 \cdot 10^6$	$2.46 \cdot 10^{-5}$	[10-400]	calculated from H_A

K_2 - second anisotropy constant

The second order anisotropy constant K_2 is plotted in figure 6.22 as function of temperature. The values for K_2 appear to be very small and slightly positive for $T > 150$ K, where no extrapolation is necessary. It is reported in literature [3], that the integration method for small values of K_2 might produce wrong signs. Comparing with literature values at room temperature, K_2 is generally assumed to be zero or too small and therefore being neglected over the whole temperature range [19]. Below $T \leq 150$ K however

K_2 is strongly negative and exceeds K_1 by a factor of approximately -2 at $T = 10$ K. Again it is important to mention that due to the overall high anisotropy of the sample a high magnetic field has to be applied, which was not possible as the maximum available field is 90 kOe. As a consequence, the magnetization curves were extrapolated as described in the previous chapter. With the help of the integration method the anisotropy constant K_2 was determined with (red circles) and without (black squares) extrapolation, as can be seen in figure 6.22. The values of K_2 which were obtained without extrapolation are also shown to emphasize the weakness of the integration method: All small measurement uncertainties in the magnetization measurement do show up as propagated error in the anisotropy constants.

The Brühkatov-Kirensky fit (red line in figure 6.22) delivers for $K_2(0) = -7.56 \frac{\text{MJ}}{\text{m}^3}$ and for $\alpha = 121.17 \cdot 10^{-6} \text{ K}^{-2}$. In table 6.4 all anisotropy constants obtained by the Brühkatov-Kirensky fits are listed up.

Another possibility of determining K_2 is to calculate it from the reduced

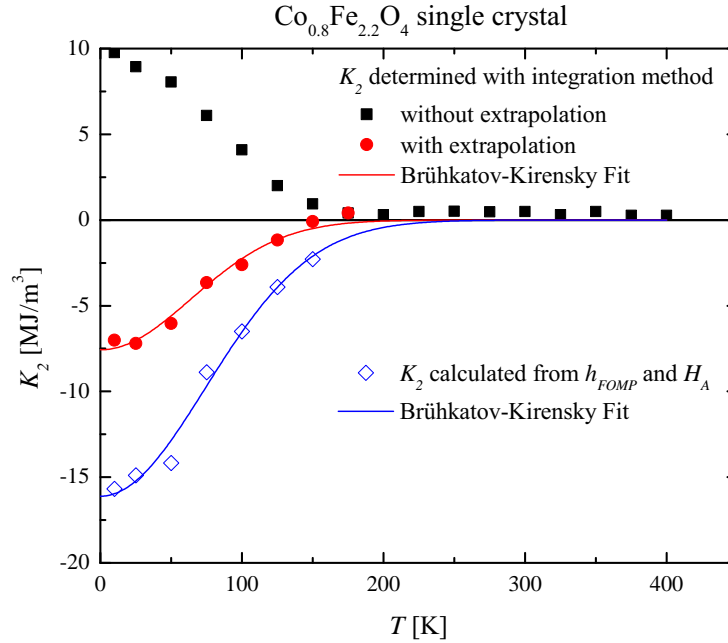


Figure 6.22: Magnetic anisotropy constant K_2 as function temperature.

Table 6.4: Results of Brükatov-Kirensky fit of the second order anisotropy constant of cobalt ferrite.

$K_2(0) [\frac{J}{m^3}]$	$\alpha [K^{-2}]$	Temperature Range [K]	Source
$-7.56 \cdot 10^6$	$1.21 \cdot 10^{-4}$	[10-400]	integration method
$-16.1 \cdot 10^6$	$9.03 \cdot 10^{-5}$	[10-400]	calculated from h_{FOMP}

Table 6.5: Anisotropy constants K_{1calc} and K_{2calc} of cobalt ferrite obtained by direct calculation via H_{Sat} and H_{FOMP} .

$T [K]$	$H_{Sat} [kOe]$	$H_{FOMP} [kOe]$	η_{FOMP}	$\frac{K_2}{K_1}$	$K_{1calc} [\frac{MJ}{m^3}]$	$K_{2calc} [\frac{MJ}{m^3}]$
10	162	61	0.862	-3.600	4.20	-15.1
25	159	61	0.862	-3.600	4.12	-14.8
50	155	60	0.866	-3.470	4.01	-13.9
75	135	60	0.892	-2.590	3.48	-9.02
100	123	59	0.910	-2.070	3.16	-6.53
125	108	59	0.958	-1.320	2.75	-3.63
150	98	59	0.953	-0.934	2.47	-2.31

FOMP field h_{FOMP} and the saturation or anisotropy field $H_A = \frac{2K_1}{M_{Sat}}$ along the [110] axis. As the saturation field is only depending on K_1 and the FOMP field is depending on the ratio of K_2 to K_1 , we can use the derived relations from chapter 3 (see figure 3.6). With a saturation field of 162 kOe at $T = 10$ K and a FOMP field of 61 kOe, we get a reduced FOMP field of $h_{FOMP} = 0.377$ yielding in the reduced magnetization value of $\eta_{FOMP} = 0.862$, according to formula 3.8. With formula 3.9 we get a K_2 to K_1 ratio of -3.6. By using the calculated quantity $K_{1calc} = \frac{H_{Sat} M_{Sat}}{2} = 4.2 \frac{MJ}{m^3}$, we finally get for $K_{2calc} = -15.1 \frac{MJ}{m^3}$ instead of the value $K_2 = -7.01 \frac{MJ}{m^3}$ obtained from integration method. In figure 6.22 the open diamond shaped symbols show the results of the calculation. In table 6.5 both calculated anisotropy constant K_{1calc} and K_{2calc} of cobalt ferrite are listed up for various temperatures.

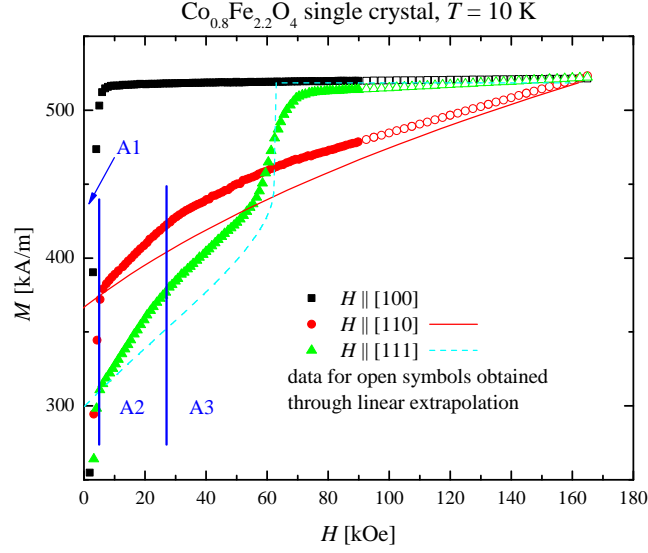


Figure 6.23: Magnetization measurement of the $\text{Co}_{0.8}\text{Fe}_{2.2}\text{O}_4$ single crystal at $T = 10\text{ K}$ with linear extrapolation data and calculated theoretical behavior of the magnetization.

Discussion on anisotropy constants

The most striking difference of both methods used for evaluating the anisotropy constants is that the integration method delivers smaller values throughout the whole temperature range. In figure 6.23 the magnetization measurements at $T = 10\text{ K}$ is plotted as example. It shows the linear extrapolation and the calculated theoretical behaviour of the magnetization $M(H)$. The overall trend for both is the same, but with one major discrepancy: the values of the measured magnetization curves are much higher as compared to the calculated. This behavior can be explained with the help of the phase theory [78]. Phase theory is based on the assumption that the total energy of the system can be lowered due to the formation of additional phases. In figure 6.23 three phases can be found: the first phase (A1) is a six-phase region and starts from zero field and ends approximately around 5000 Oe. In this region the internal stray field of the magnetic domains has to be overcome. As there exist six equivalent easy axes in a P-type material, the

field to overcome the stray field depends on the absolute values of the anisotropy energy E_A . Summing up, the higher the anisotropy energy is, the larger the first region will be.

The second phase (A2) lies in between the field interval $5 < H < 27$ kOe and is characterized by two-phase processes and rotation of the magnetization vector. An energetic minimum is formed by the two easy axes which are closest to the direction where the magnetic field is applied. This minimum in energy gives rise to a reduced anisotropy, which manifests in an increased slope of the magnetization, as can be seen in figure 6.23).

The beginning of the third phase (A3) is visible as small kink in the magnetization. The one-phase region is characterized by rotational processes only, as the magnetization vector has completely rotated towards the favorable easy axis derived state. Above $H > 27$ kOe only rotational processes are responsible for the change of magnetization with applied magnetic field.

The deviations from the calculation of the magnetization process can be fully understood and described with phase theory [78]. The only remaining open question is, which set of anisotropy constants should be used for describing the anisotropy of cobalt ferrite: While the integration method takes the micromagnetic behavior into account, the calculation from the FOMP field only delivers the theoretical, perfect single crystalline behavior of the magnetic anisotropy. Clearly the integration method has to be favoured: First because the calculation from the FOMP field only describes an ideal single crystal which never can be obtained, as dislocations and internal stresses are always present. Second the integration method is reflecting the reduced anisotropy, which arises due to phase theory.

While at room temperature the magnetic anisotropy of cobalt ferrite can be described with the first order anisotropy constant only, at temperatures below 150 K it is necessary to include the second order anisotropy constant K_2 . It was found that the temperature dependence of both constants can be described with the empirical Brühkatov-Kirensky law [72, 73].

E_A - the anisotropy energy function

With all three anisotropy constants K_0 , K_1 and K_2 it is possible to draw the temperature dependent anisotropy energy function E_A . In figure 6.24 the anisotropy energy function of cobalt ferrite at $T = 10$ K is plotted as an example. The first section was performed along the (100) plane, while the second section was done along the (110) plane. With these two sections the anisotropy energy function along the three main axes is better visible. The minima in the energy function refer to the [100] directions, while the maxima represent the [110] and the [111] directions. Figure 6.25 shows the anisotropy energy along the (110) plane, which is described by the function:

$$E_{A[110]}(\theta) = K_0 + K_1 \cdot \left(\frac{1}{4} \sin^4 \theta + \sin^2 \theta \cos^2 \theta \right) + \frac{K_2}{4} \cdot \sin^4 \theta \cos^2 \theta, \quad (6.5)$$

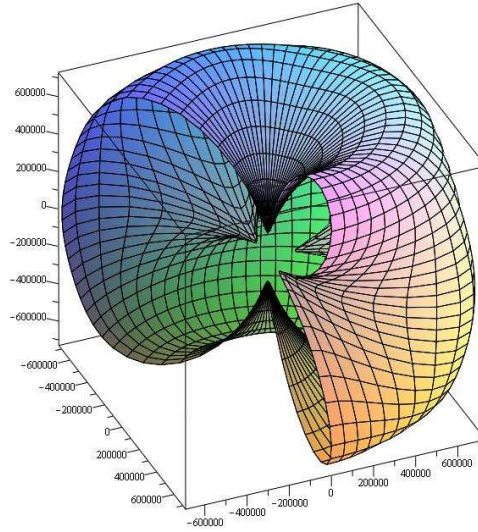


Figure 6.24: Three dimensional plot of the magnetic anisotropy energy function for cobalt ferrite at $T = 10$ K. The cuts along the (100) and (110) plane are made for better visibility.

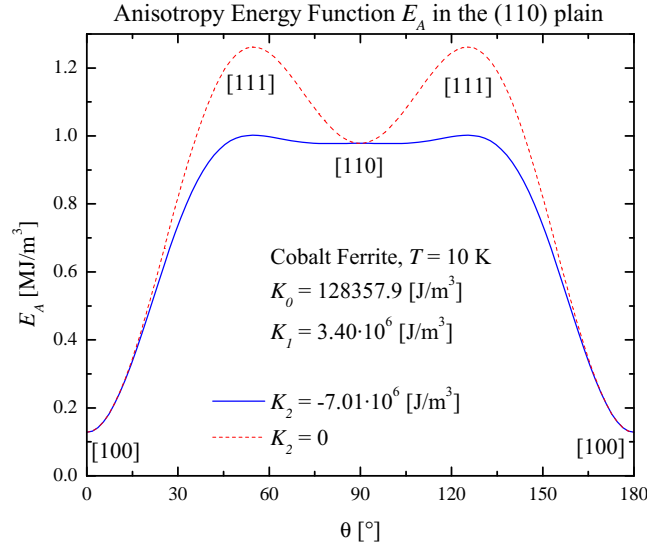


Figure 6.25: Magnetic anisotropy energy along the (110) plain for cobalt ferrite at $T = 10$ K with and without the contribution of K_2 .

where θ is the parametrization angle for rotating inside the (110) plain. Clearly it can be seen that the [100] axis is the easy one, while the [111] and the [110] axes are magnetically harder. Just for comparison the anisotropy energy is plotted with $K_2 = 0$ as dashed line. The second order anisotropy constant is reducing the overall anisotropy energy along the [111] axis, which makes that direction more favorable.

6.2.2 Magnetic Anisotropy: Polycrystalline Sample

For the polycrystalline sample the magnetic anisotropy constant K_1 was determined with the law of approach to saturation method as described in chapters 2 and 3. In the polycrystalline sample the grains are isotropically distributed and we are measuring an averaged anisotropy constant K_1 . Below $T = 150$ K it is not possible to saturate the sample with 90 kOe (see figure 6.17), which results in an reduced value of K_1 . There has been a lot of

calculations and theories on this reduced value of K_1 in literature. Only few of them are solving this problem by applying a sufficiently high magnetic field for saturating the sample [26, 64]. In figure 6.21 the green, open triangular shaped symbols represent the anisotropy constant K_1 obtained by the law of approach to saturation. Below $T = 150$ K it happens that K_1 decreases due to the insufficient high magnetic field. The magenta diamond shaped symbols are digitized data points from [64], who applied a sufficiently high magnetic field and got reasonable results also below $T = 150$ K. The reason for the higher values throughout the whole temperature range lies in the fact that this sample was nanocrystalline (average crystallite size 42 nm), which lead to an increased K_1 due to surface effects of the nanocrystalline crystallites [64].

6.2.3 Discussion: Influence of Co^{2+} Ions in Magnetite

In this section we will discuss the influence of the Co^{2+} ions on the magnetic properties in magnetite (Fe_3O_4). In pure magnetite a temperature induced structural change at the Verwey temperature $T_V \sim 120$ K is observed [79]. This transition goes from a cubic ($T > T_V$) to a monoclinic ($T < T_V$) crystal structure. Several XRD and neutron diffraction experiments were performed to determine the exact symmetry² below T_V . As the change from cubic crystal structure is very small, the results are not conclusive. The obtained symmetry varies from orthorhombic [80, 81] to tetragonal [82, 83], triclinic [84, 85, 86] and monoclinic [87, 88]. But at least they all do agree that the symmetry is no longer cubic. As the most recent publications [87, 88] have the best resolution in their experiment, the most likely crystal structure can be assumed to be monoclinic.

Besides this symmetry change, cation ordering is observed and the resulting changes in electrical resistivity [79], specific heat [89] and magnetization were investigated [90, 91]. At $T_I \sim 130$ K an isotropic point is found where a change of easy axis of the magnetization occurs. For $T > T_I$ the magnetic

²The term “symmetry” is used here as abbreviation for the “point group of the crystallographic space group”.

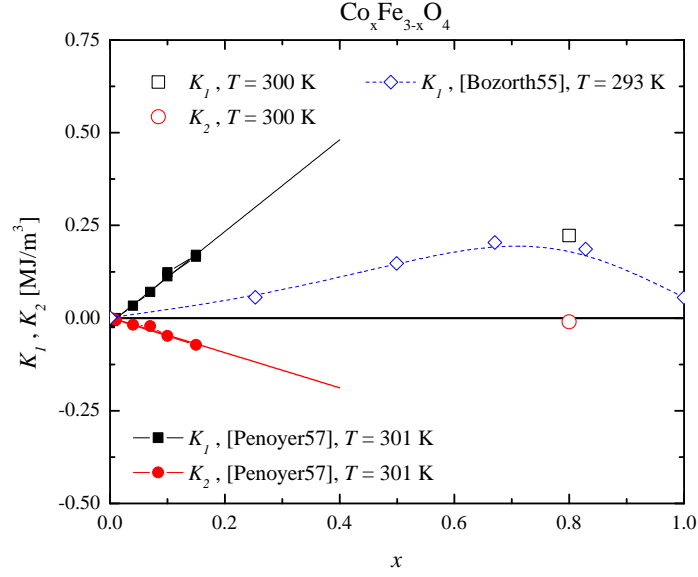


Figure 6.26: First and second order anisotropy constants as function of Co concentration x . Filled Symbols are digitized from [16], while open symbols represent measured values (see chapter 6.2.1).

easy axis is parallel to the $[111]$ direction (N-type) which changes for $T_V < T < T_I$ to the $[100]$ direction (P-type). This isotropic point is caused by a change of the anisotropy constants K_1 and K_2 . A lot of investigations with different dopants in magnetite were performed and their influence on the Verwey transition T_V with respect to their the concentration was studied [92].

The influence of the Co^{2+} ions in magnetite was investigated quite early [91]. Special care was taken on the change of the Verwey transition and its temperature shift with increasing Co content. With higher doping levels this structural transition from cubic to monoclinic even vanishes completely.

Moreover with the presence of Co^{2+} ions in the spinel lattice an increase of the first and second order anisotropy constant is observed [16], which is shown in figure 6.26. A quite linear increase of both anisotropy constants of Co doped Magnetite $\text{Co}_x\text{Fe}_{3-x}\text{O}_4$ with respect to the doping concentration x is found. Together with the data of our measured anisotropy constants

(see chapter 6.2.1) and digitized data from Bozorth [10], a maximum in the anisotropy constant K_1 around $x = 0.7$ can be seen, followed by a decrease with increasing Co content x .

The origin and rise of the second order anisotropy constant K_2 is discussed in chapter 2.3.5, where an additional trigonal symmetry axis in the structure along the $[111]$ axis is pointed out. With the presence of Co^{2+} ions in the octahedral site [93] an increase of the second order anisotropy constant K_2 is also expected, as indicated in figure 6.26.

6.2.4 Internal vs. External Magnetic Field

The evaluation of the magnetization data revealed that for calculating the magnetic anisotropy (see chapter 3) and the law of approach to saturation (see chapter 2) the difference between internal and external magnetic field is so small, that it even vanishes in the error bar. As the single crystal has not a very defined shape, the demagnetizing factor N was approximated with $\frac{1}{3}$, which corresponds to a sphere. Moreover the integration area for determining the anisotropy energy was calculated for different values of N , yielding in a quite linear change of the integration area as can be seen in figure 6.27, where the relative change of the integrated areas is plotted as function of N at two different temperatures. The resulting anisotropy constants are shown in figure 6.28. Clearly it can be seen that the difference between the internal magnetic field ($N = \frac{1}{3}$) and the external magnetic field for calculating K_0 and K_1 is insignificant.

One would not expect that the difference in the anisotropy constant K_1 is that small. For the saturation magnetization, the coercive field, the high-field susceptibility and all other magnetic quantities the correction to the internal magnetic field is not necessary, only for the remanence and K_0 it is important. Because of the fact that the remanence data has a huge uncertainty as the demagnetizing factor was only estimated, any analysis was omitted. For determining all other quantities the external magnetic field was used, as the correction to the internal magnetic field proved to be not necessary.

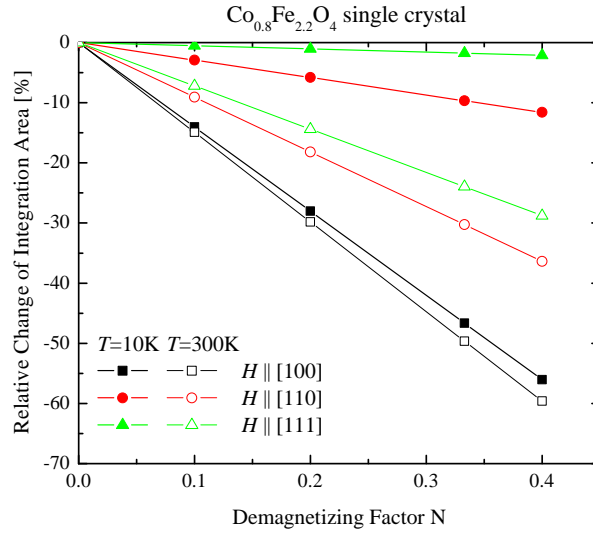


Figure 6.27: Relative change of the integration area as function of the demagnetizing factor N at two different temperatures.

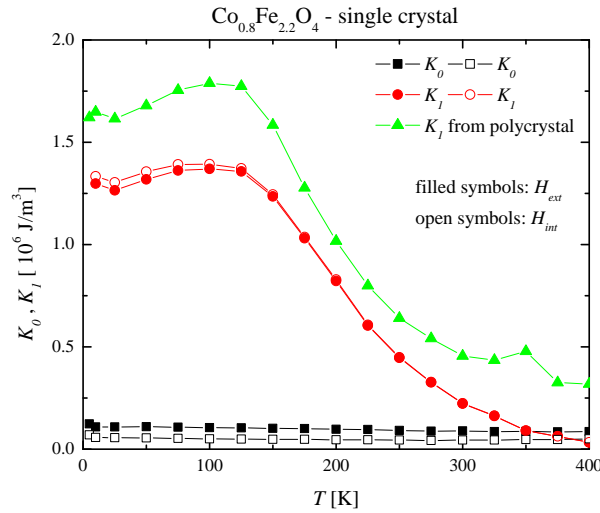


Figure 6.28: Magnetic anisotropy constants K_0 and K_1 evaluated with internal and external magnetic field without extrapolation, see figure 6.21.

6.2.5 Coercive field

Coercive field of the single crystal

In figure 6.29 the coercive field H_C of the single crystal is plotted as function of the temperature. The coercive field for all three main crystallographic axes is very small above $T = 200$ K and therefore not really easy to measure in a magnetically open system. However below $T = 200$ K the coercive field is continuously rising with decreasing temperature. It is remarkable that H_C the easy $[100]$ axis reaches the highest values, followed by the intermediate $[110]$ axis. Only the coercive field of the hard $[111]$ axis is constantly below the two other axes. One possible explanation might lie in the formation of a direction dependent magnetic domain configuration. As the magnetization vector lies in the easy $[100]$ axis at low magnetic field, more domain walls can be formed along the $[100]$ axis. It is clear that the other axes are

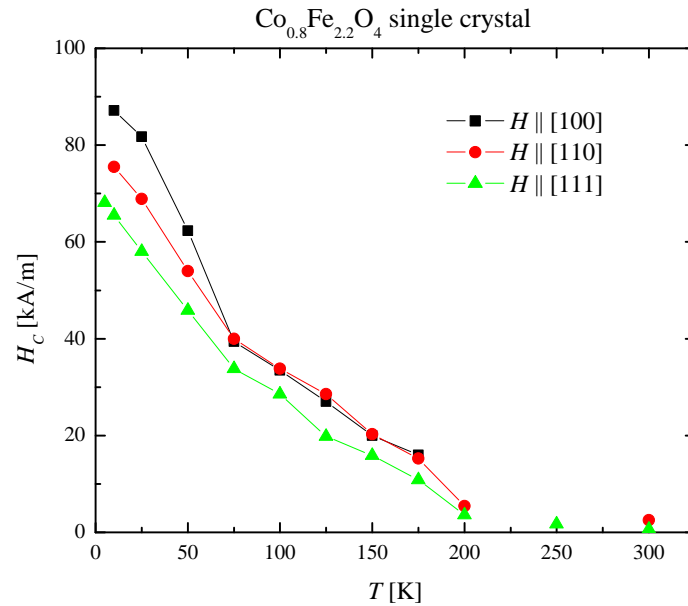


Figure 6.29: Variation of the coercive field with temperature along the three main crystal axes of single crystalline cobalt ferrite.

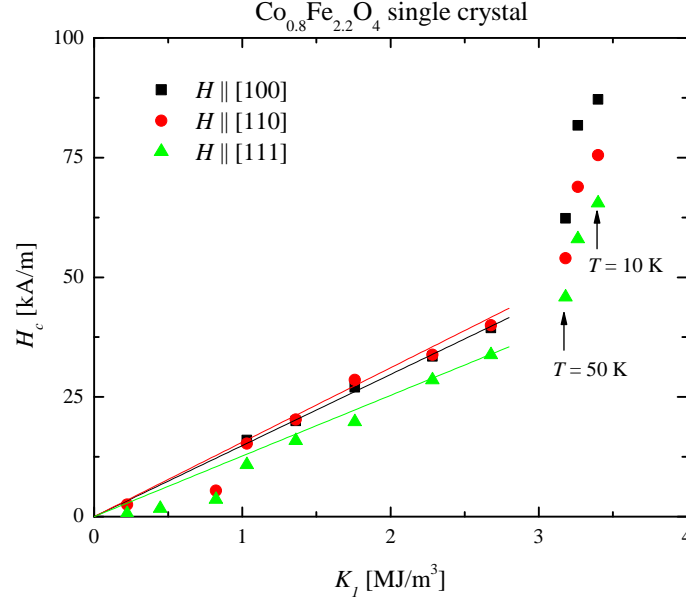


Figure 6.30: The coercive field of the three main crystal axes of cobalt ferrite plotted as function of the first anisotropy constant K_1 . The lines were added after a linear fit in the temperature range of [300 - 75 K].

energetically less favorable and the coercive field is therefore reduced.

The overall behavior of the increasing coercive field with decreasing temperature points to a correlation with the temperature dependence of the magnetic anisotropy energy and - as a consequence - a change of the rotation behavior of the magnetization vector. In figure 6.30 the coercive field is plotted as function of the first magnetic anisotropy constant K_1 . A quite linear behavior is found over a very broad temperature range [300 - 75 K], the lines were added after a linear fit. It is however clear that the coercive field can not be fully described only using the first anisotropy constant, as it was shown in the previous chapter that the second order anisotropy constant is no longer negligible below $T = 150 \text{ K}$.

Coercive field of the polycrystal

The coercive field of the polycrystal is of course much higher than that of the single crystal as can be seen in figure 6.31. It is clear however that the number of grain boundaries and dislocations in the polycrystal is much higher than in a single crystal (which should be free of dislocations at all). Consequently the coercive field of a polycrystal should be larger as well. The single crystal data were plotted as comparison. The overall trend of increasing coercive field with decreasing temperature is observed in the polycrystal as well.

The coercive field as function of the first anisotropy constant K_1 is shown in figure 6.32. Once more a quite linear behavior is found, although it is not perfectly fitting over the whole temperature range. And again it should be mentioned that beside the microstructure, the second order anisotropy constant K_2 should be taken into account for a more detailed temperature dependent analysis.

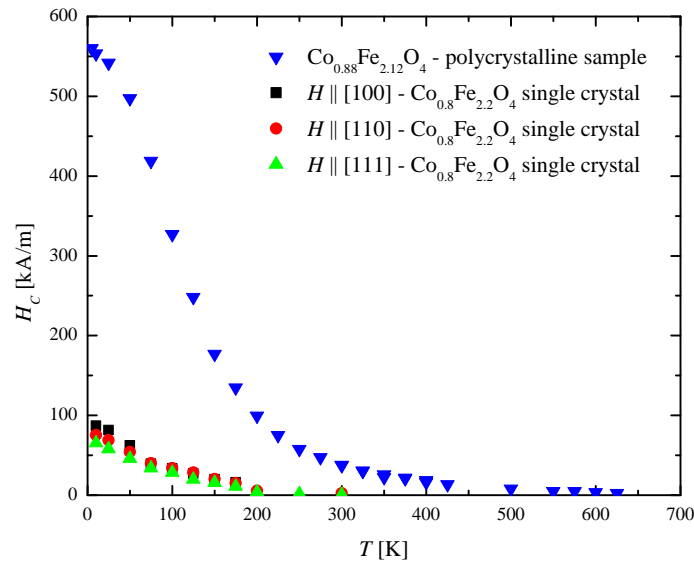


Figure 6.31: Variation of the coercive field with temperature for the single crystal and polycrystal cobalt ferrite sample.

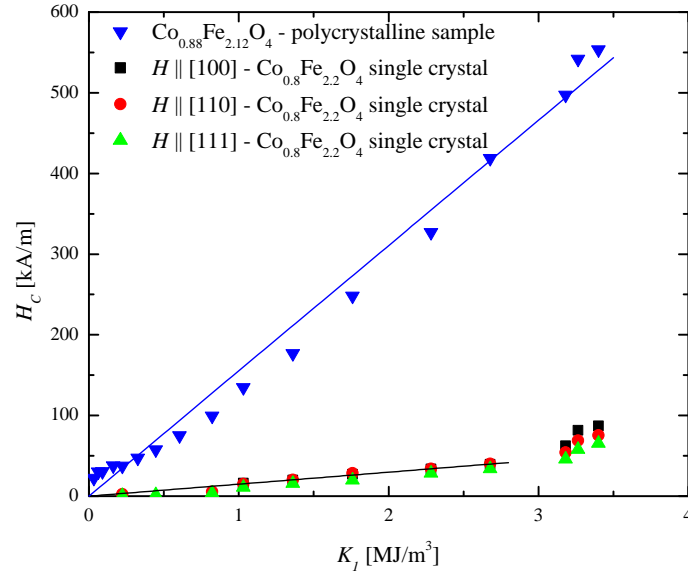


Figure 6.32: The coercive field of polycrystalline cobalt ferrite sample plotted as function of the first anisotropy constant K_1 . The lines were added after a linear fit.

6.3 Magnetostriction

Magnetostriction measurements of the single crystal and the polycrystalline samples were performed from $T = 4.2$ to 300 K in the capacitance cell which was described in chapter 4. The three main crystallographic axes [100], [110] and [111] of the single crystal and two polycrystalline samples were measured at certain temperatures with a maximum applied field of $H = 90$ kOe. For all polycrystalline cobalt ferrite samples a remanent magnetostriction was detected. A measurement procedure was developed for considering this effect. After each measurement at a certain temperature, the whole setup was heated up to room temperature, the sample was taken out of the magnetostriction cell and heated up above the Curie-Temperature (in air) in order to get rid of the field induced magnetic domains, which cause a remanence. In the next step the sample was slowly cooled without any external applied magnetic field, followed by mounting the sample in the magnetostriction cell and cooling the setup to the next desired temperature. It is important to note, that only with this (very time consuming) procedure it is ensured that the sample is demagnetized before the measurement and that the remanent magnetostriction can be determined accurately. Although no remanent magnetostriction was found for the single crystal, this procedure was applied for all measured crystallographic directions as well.

For measuring magnetostriction with the capacitance cell it is also very important to note that the temperature has to be very stable. If the temperature of the sample would change within less than 0.1% while measuring, the cell would notice this change as “parasitic” thermal expansion signal added to the magnetostriction signal and the measurement would produce values far too high or far too low. As an example the desired magnetostriction measurement temperature should be $T = 100$ K together with the linear thermal expansion coefficient of silver $\alpha = 1.45 \cdot 10^{-5} \text{ [K}^{-1}\text{]}$, as the cell is mainly made out of silver. Assuming that the stability of the temperature would be 1 percent yielding to $\Delta T = 1$ K, the parasitic linear thermal expansion signal would be $\frac{\Delta l}{l} = 1 \cdot 1.45 \cdot 10^{-5} = 1.45 \cdot 10^{-5}$ which is of the same order of magnitude as the magnetostriction signal of nickel

or iron. At higher temperatures this contribution will get even bigger, as the linear thermal expansion coefficient increases. Therefore special care was taken on the temperature stability of the measurement setup. Nevertheless it was sometimes necessary to correct the measured signal by subtracting the linear thermal expansion due to small changes in sample temperature while measuring. All magnetostriction measurements were evaluated with the help of the self developed magnetostriction model from chapter 4.

6.3.1 Magnetostriction of the single crystal

[111] hard axis

Figure 6.33 shows the the magnetostriction measurement at $T = 4.2$ K with $H \parallel [111]$. The magnetostriction curve shows a very strong hysteresis below

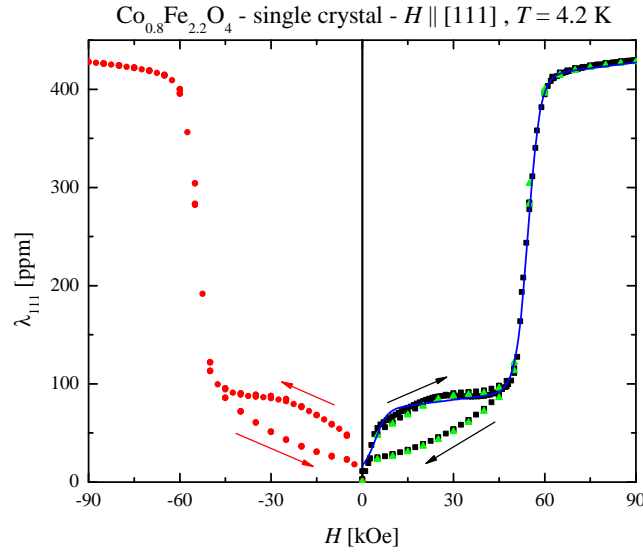


Figure 6.33: Magnetostriction at $T = 4.2$ K with $H \parallel [111]$. The arrows indicate the magnetostriction measurement with increasing and decreasing magnetic field.

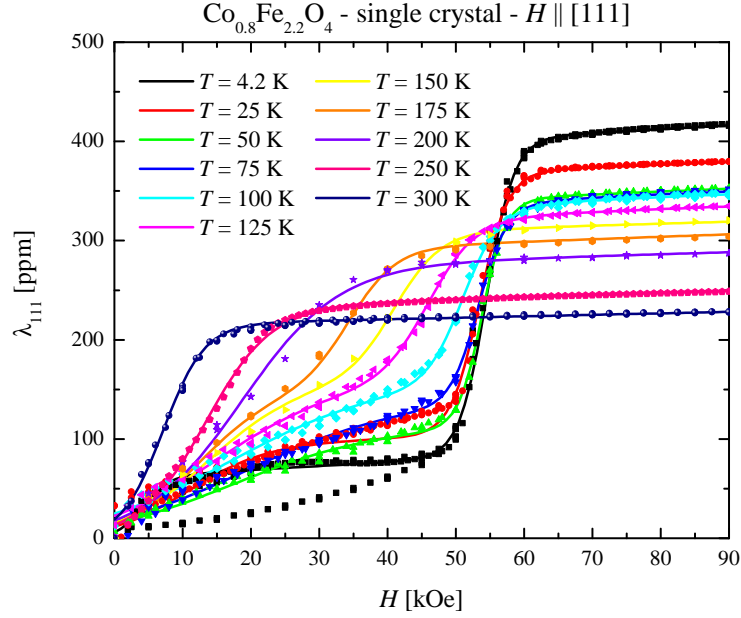


Figure 6.34: Magnetostriction as function of field $H \parallel [111]$, plotted in the temperature range of [4.2 - 300 K]. The lines are drawn after a fit according to the magnetostriction model.

the FOMP field of 55 kOe. The saturation magnetostriction is reached above the FOMP and its value is $\lambda_{111}(4.2 \text{ K}) = 390 \text{ ppm}$, when correcting the linear increase (τH) of the magnetostriction model. Without this correction the determined value is of course higher with $\lambda_{111}(4.2 \text{ K}) = 414.3 \text{ ppm}$. It is worth to note that no remanence is measured, although the sample exhibits a huge hysteresis below the FOMP field. The arrows indicate the magnetostriction measurement with increasing and decreasing magnetic field. For these measurement a negative magnetic field was applied as well, with the result that the curves are reproduced, only mirrored around the ordinate.

In figure 6.34 the magnetostriction measured along the [111] axis in the temperature range [4.2 - 300 K] is plotted. The solid lines represent the fits according to the magnetostriction model. The fit parameters are shown in table 6.6. The FOMP is very prominent as a sharp jump around 55 kOe. With increasing temperature, the height of the jump in the magnetostriction

Table 6.6: Fit parameter using formula 4.10 for describing the measurements of $\lambda_{111}(H)$ (see lines in figure 6.34).

T [K]	λ_1 [ppm]	c_1 [10^{-6} T^{-1}]	H_1 [T]	λ_2 [ppm]	c_2 [10^{-6} T^{-6}]	H_2 [T]	τ [10^{-6} T^{-1}]	λ_{111} [ppm]
4.2	70	2.8	0.55	320	5.96	5.5	2.7	390
25	90	1.75	1.08	264.8	4.8	5.34	2.7	354.8
50	100	0.99	1.75	228.01	5.81	5.38	2.7	328.01
75	125.6	0.92	1.92	199.6	4.93	5.33	2.7	325.2
100	145.9	0.93	1.69	176.5	3.76	5.1	2.7	322.4
125	147.4	1.16	1.47	162.7	2.9	4.6	2.7	310.1
150	150.96	1.55	1.38	150	2.9	4.1	2	300.96
175	143.3	1.81	1.22	140.5	2.92	3.44	2.5	283.8
200	135.15	1.41	1.87	135.15	1.41	1.87	2	270.3
250	114.8	2.09	1.34	114.8	2.09	1.34	2.2	229.6
300	107.35	3.28	0.71	107.35	3.28	0.71	1.5	214.69

is decreasing. In addition the FOMP field is decreasing as well. Starting with a FOMP field of 55 kOe from $T = 4.2 \text{ K}$ to $T = 75 \text{ K}$, it is becoming smaller from 50 kOe at $T = 100 \text{ K}$ to 35 kOe at $T = 175 \text{ K}$ as can be seen in table 6.6. Above $T = 175 \text{ K}$ the FOMP is no longer visible, which manifests itself in the fitting results of the magnetostriction model: As the two magnetostriction related fit parameter λ_1 and λ_2 are no longer separable above $T = 200 \text{ K}$, only one fit parameter was used to describe the magnetostriction. In figure 6.35 the two fit parameter λ_1 and λ_2 , together with λ_{111} are plotted as function of temperature. The reason for this splitting up of λ_{111} below $T < 150 \text{ K}$ is the increased anisotropy (see chapter 6.2.1). Being more precisely the rise of K_2 with the consequence that the jump in the magnetization (see figure 3.6) also influences the magnetostriction behavior.

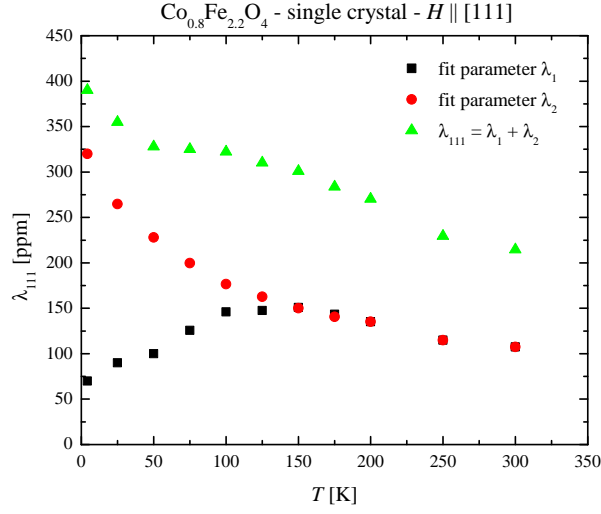


Figure 6.35: Variation of the fit parameter λ_1 and λ_2 and the resulting magnetostriction constant λ_{111} with the temperature.

[110] intermediate axis

Starting with the well known relation for $\lambda_{110} = \frac{1}{4}\lambda_{100} + \frac{3}{4}\lambda_{111}$ (see formula 4.2), it should be possible to describe the magnetostriction along the [110] axis only with the two magnetostriction constants λ_{100} and λ_{111} . An important assumption for this formula is that the sample is magnetically saturated, which is however not fully reached below $T < 150$ K, as the saturation field (see figure 6.17) is higher than the maximum available field of 90 kOe. Nevertheless one of the strengths of the magnetostriction model presented in chapter 4 is the inclusion of the magnetic anisotropy in modeling the magnetostriction. In figure 6.36 the measured magnetostriction $\lambda_{110}(H)$ and the calculated magnetostriction are presented. For the simulation with the magnetostriction-model all parameters, like anisotropy field and magnetostriction constants from the prior measurements along the [111] axis were taken, except for λ_{100} . As it was already mentioned in chapter 4.1.1 the direct magnetostriction measurement along the easy axis might produce wrong values because of a remanent magnetostriction due to a certain, unfavorable domain configuration. Therefore λ_{100} was determined indirectly from

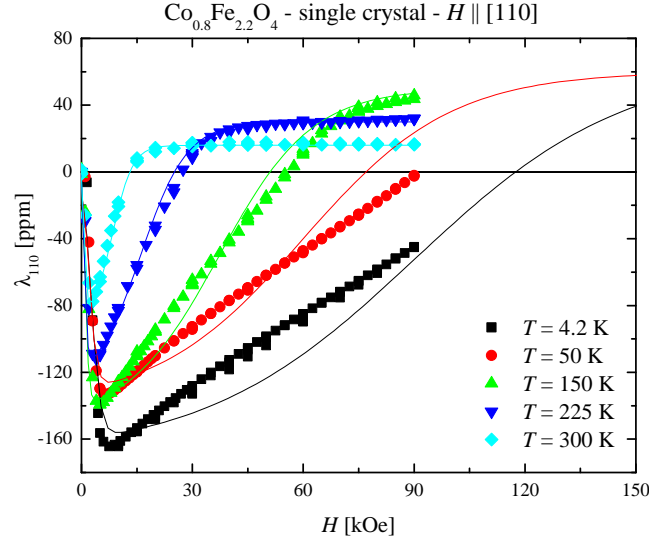


Figure 6.36: Magnetostriction as function of field $H \parallel [110]$, plotted in the temperature range of [4.2 - 300 K]. The lines are drawn after a fit according to the magnetostriction model.

the magnetostriction measurement along the λ_{110} axis. In the next subsection both measurements of λ_{100} will be compared.

In table 6.7 all fit parameters are listed up. From the fit parameter c_2 and h_2 the anisotropy field H_A was calculated with the help of the 95% criterion (formula 4.9). With the obtained magnetostriction model parameters λ_1 and λ_2 the magnetostriction constants $\lambda_{100} = 4\lambda_1$ and $\lambda_{111} = \frac{4}{3}\lambda_2$ were derived.

Table 6.7: Fit parameter for describing the measurements of $\lambda_{110}(H)$ (see figure 6.36 and formulas 4.2 and 4.9).

T [K]	$\lambda_1 = \frac{\lambda_{100}}{4}$ [ppm]	c_1 [10^{-6} T^{-1}]	H_1 [T]	$\lambda_2 = \frac{3\lambda_{111}}{4}$ [ppm]	c_2 [10^{-6} T^{-6}]	H_2 [T]	H_A [kOe]
4.2	-228.4	8.12	0.21	280	0.22	5.9	192.8
50	-218.8	7.57	0.13	284	0.23	4.16	169.6
150	-187.4	12.25	0.13	246.8	0.49	3.19	92
225	-141.4	15.3	0.13	172.3	1.32	1.54	37.7
300	-106.2	17.9	0.11	122.8	3.16	0.7	16.3

Table 6.8: Calculated values of λ_{110} , λ_{100} and λ_{111} , obtained from the fit parameters λ_1 and λ_2 from table 6.7. Data evaluated according to formula 4.2

T [K]	$\lambda_{110} = \lambda_1 + \lambda_2$ [ppm]	$\lambda_{100} = 4\lambda_1$ [ppm]	$\lambda_{111} = \frac{4}{3}\lambda_2$ [ppm]
4.2	51.6	-913.6	373.33
50	65.2	-875.2	378.67
150	59.4	-749.6	329.07
225	30.9	-565.6	229.73
300	16.6	-424.8	163.73

These values are presented in table 6.8 and their excellent agreement with the magnetostriction measurement is shown in figure 6.36. For example the $\lambda_{110}(H)$ measurement at $T = 225$ K: The first sharp downturn is accounted to the first magnetostriction constant λ_{100} , while the upturn is due to the higher anisotropy contribution of λ_{111} . It is remarkable that $\lambda_{100}(H)$ is saturating quite quickly ($H_{Sat} \sim 5$ kOe), as it is expected for the easy axis. Whereas $\lambda_{111}(H)$ shows the anisotropy field values expected for the [110] direction, as can be seen in the calculated H_A in table 6.7. The overall behavior is in good agreement and it is shown that the behavior of the magnetostriction can be described quite accurately as function of the magnetic field including the magnetic anisotropy.

[100] easy axis

In figure 6.37 the magnetostriction measurement along the [100] axis is plotted for four different temperatures. The saturation magnetostriction is reached at quite low magnetic fields around 5 kOe. These values correspond to the measured anisotropy field of the magnetization measurements. In table 6.9 the fit parameter for describing the curves with the magnetostriction model are listed up.

In figure 6.38 the two main magnetostriction constants are plotted as function of temperature. Clearly one can see that the directly measured values of λ_{100} are significantly smaller than the indirectly obtained from

Table 6.9: Fit parameter for describing the direct measurement of λ_{100} (see figure 6.37).

T [K]	$\lambda_1 = \lambda_{100}$ [ppm]	c_1 [10^{-6} T^{-1}]	H_1 [T]	τ [10^{-6} T^{-1}]
4.2	-550	11.48	0.37	-3.2
100	-550	12.52	0.32	-3.3
200	-500.69	13.39	0.27	-3.7
300	-408.8	15.22	0.25	-4.4

the λ_{110} measurement. Although the sample was demagnetized before each measurement, an unfavorable domain configuration along the easy axis of magnetization occurred which produces smaller linear magnetostriction values. Therefore the indirect magnetostriction measurement values are the more accurate and reliable.

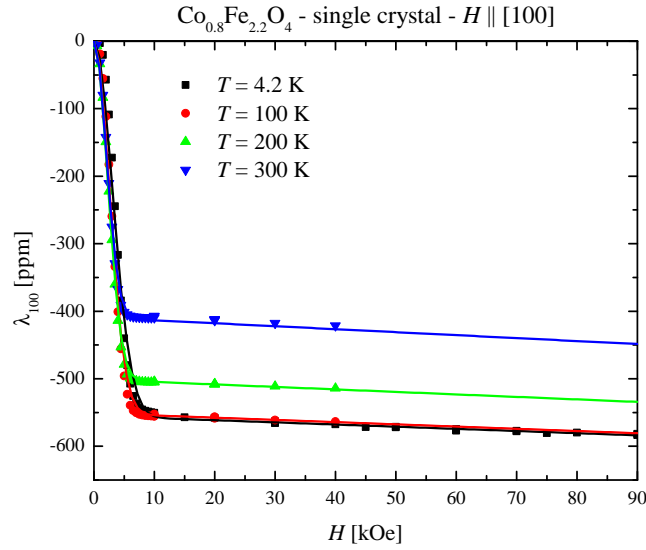


Figure 6.37: Magnetostriction as function of field $H \parallel [100]$, plotted in the temperature range of [4.2 - 300 K]. The lines are drawn after a fit according to the magnetostriction model.

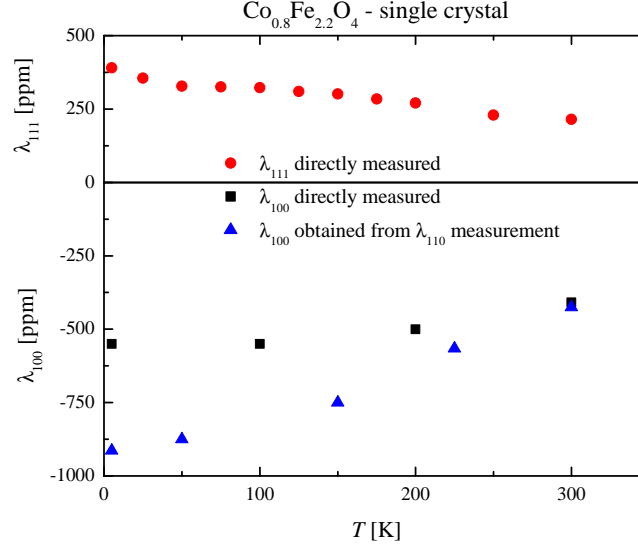


Figure 6.38: Magnetostriction constants λ_{100} and λ_{111} as function of temperature.

6.3.2 Magnetostriction of the polycrystals

The polycrystalline samples are made from pressed powder and were both annealed at very high temperature. Consequently the samples can be regarded as isotropic, so they have an isotropic grain distribution and alignment. Therefore it should be possible to explain the polycrystalline magnetostriction measurements from averaging the single crystalline data. When averaging formula 4.1 over the different crystal orientations with $\alpha_i = \beta_i$ we can describe the saturation magnetostriction for an isotropic polycrystalline sample with:

$$\lambda_{Sat} = \frac{2}{5}\lambda_{100} + \frac{3}{5}\lambda_{111}$$

For a correct description of the magnetostriction of the polycrystalline sample, it is necessary to include the anisotropy related part of the single crystal magnetostriction curve in the volume averaging process. This is included in the magnetostriction model (see chapter 4). With the help of the anisotropy constants obtained from the single crystal measurements (chapter 6.2.1) it is

possible to calculate the mean anisotropy energy $\langle E_A \rangle$ simply by averaging formula 3.4 over the volume:

$$\langle E_A \rangle = K_0 + \frac{K_1}{5} + \frac{K_2}{105} \quad (6.6)$$

and the resulting mean anisotropy field $\langle H_A \rangle$:

$$\langle H_A \rangle = \frac{2 \langle E_A \rangle}{M_{Sat}}. \quad (6.7)$$

With the mean anisotropy field the remanent magnetostriction will be explained.

The magnetization and magnetostriction of the two polycrystalline samples were both measured. Not only the composition but also the heat treatment (100 hours at $T = 1000^\circ\text{C}$ in air) is identically, as they were both pressed into pellets with exactly the same powder. While for one sample - named “HT2” - the emphasis of the measurement was put on the temperature dependence of the magnetostriction, the second sample - named “HT2B” - was investigated in positive and negative applied magnetic fields in order to determine the magneto-elastic hysteresis behavior.

Longitudinal and Transverse Magnetostriction

In figure 6.39 the transverse (λ_\perp - open symbols) and longitudinal (λ_\parallel - filled symbols) magnetostriction of the “HT2” sample was measured, while figure 6.40 shows the measurements of the second sample “HT2B”. The overall trend from the single crystal measurements is also found here: with decreasing temperature the magnetostriction is increasing. Additionally, the remanence magnetostriction of both samples is also increasing. It is important to mention that before each measurement the sample was demagnetized by heating above the Curie-temperature. Otherwise it would not be possible to determine the remanent magnetostriction. From the longitudinal and transverse magnetostriction measurements the saturation magnetostriction was derived and an analysis of the remanence and the magnetoelastic hysteresis was performed.

Saturation Magnetostriction

In figures 6.41 and 6.42 the saturation magnetostriction $\lambda_{Sat} = \frac{2}{3}(\lambda_{\parallel} - \lambda_{\perp})$ of both samples are plotted as function of the magnetic field. As the samples are both isotropic ($\lambda_{\parallel} = -2 \cdot \lambda_{\perp}$), the longitudinal and the saturation magnetostriction are nearly equal. With the help of the magnetostriction model (chapter 4) and formula 4.4, the two cubic magnetostriction constants λ_{100} and λ_{111} were determined as function of temperature. In table 6.10 the fit parameters for both samples are listed.

The mean anisotropy field $\langle H_A \rangle$ is plotted in figures 6.41 and 6.42 as vertical line for various temperatures. It approximately shows the point, where the “virgin” magnetostriction curve meets the “major loop” magnetostriction curve. As the mean anisotropy reflects the averaged magnetic anisotropy which is found in a polycrystalline material [49], it makes sense that the

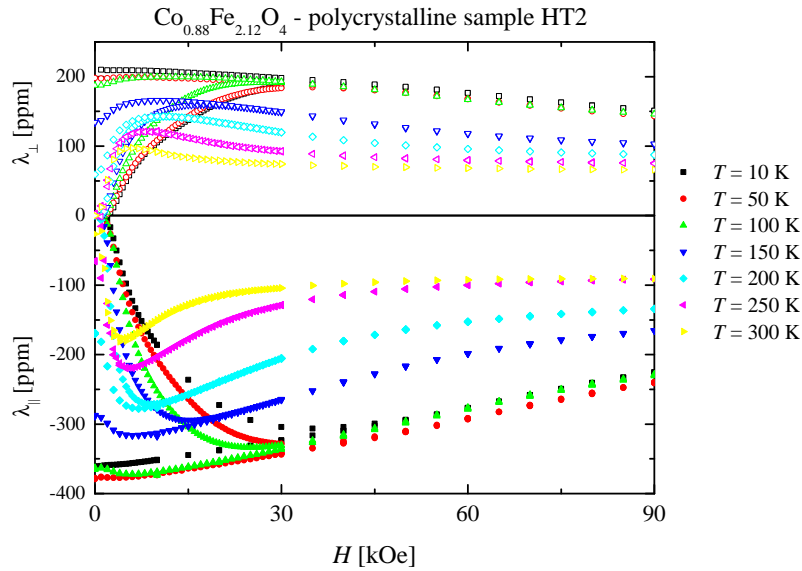


Figure 6.39: Transverse (λ_{\perp} - open symbols) and longitudinal (λ_{\parallel} - filled symbols) magnetostriction of the “HT2” sample.

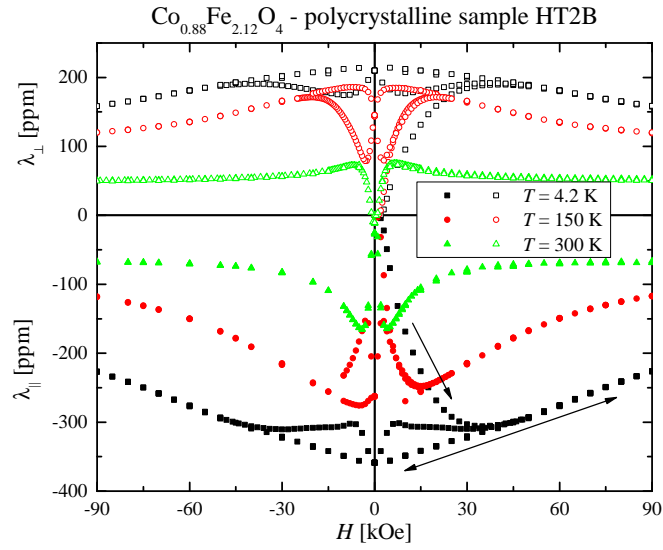


Figure 6.40: Transverse (λ_{\perp} - open symbols) and longitudinal (λ_{\parallel} - filled symbols) magnetostriction of the “HT2B” sample

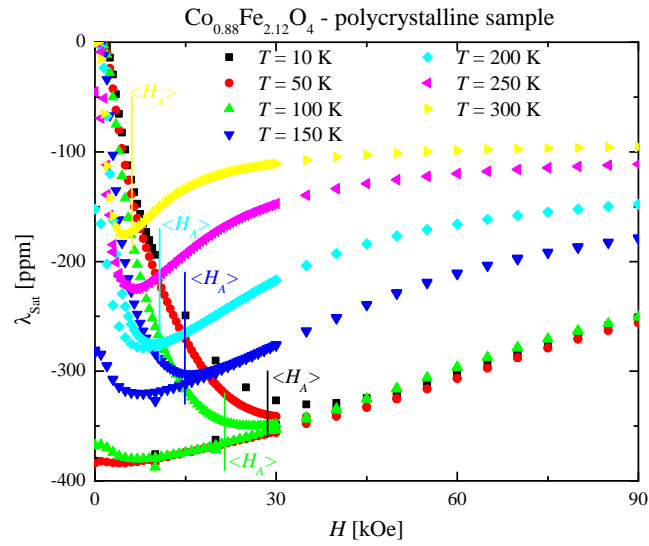


Figure 6.41: Saturation magnetostriction of the “HT2” sample.

mean anisotropy field describes the necessary field strength to overcome the remanent magnetostriction.

In figure 6.43 the saturation magnetostriction of “HT2” at $T = 10$ K is plotted as example for the application of the magnetostriction model. The blue solid line represents the fit of the “virgin” magnetostriction curve according to the magnetostriction model. The fit parameters can be found in table 6.10. The sample exhibits a very prominent remanent magnetostriction of $\lambda_{rem} = -381$ ppm. As soon as the remanent magnetostriction point is reached at $H = 0$, a magnetic domain configuration is formed, where the (negative) λ_{100} -derived magnetostrictive states do no longer contribute to the magnetostriction signal. Only the (positive) λ_{111} -derived magnetostrictive states contribute to the magnetostriction signal. The λ_{111} -derived magnetostrictive states include all crystallographic directions but the $[100]$ oriented grains. Therefore the magnetostriction signal shows a higher magnetic anisotropy, as for example the $[110]$ oriented grains need a magnetic field of 160 kOe to reach saturation.

Overall the saturation magnetostriction of the polycrystals can be described

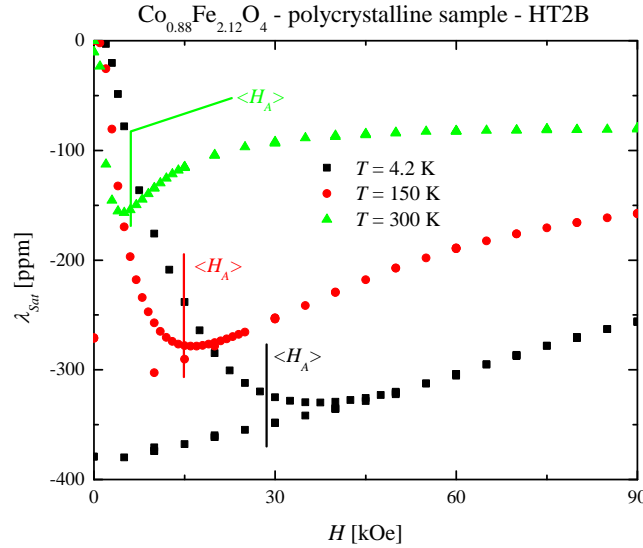


Figure 6.42: Saturation magnetostriction of the “HT2B” sample.

as function of the magnetic field in the same way as for the single crystals: the magnetostriction constants are multiplied with the magnetic anisotropy related distribution function, leading to a field dependent saturation magnetostriction: $\lambda_{Sat}(H) = \frac{2}{5}\lambda_{100}(H) + \frac{3}{5}\lambda_{111}(H)$. The only exception is that the remanent magnetostriction can no longer be neglected. λ_{rem} is mainly caused by the easy axis magnetostriction $\lambda_{100}(H)$, where after being magnetized due to irreversible magnetic domain formation no contribution to the magnetostriction is measured. Whereas $\lambda_{111}(H)$ seems to be not affected at all by magnetic domain formation, because at higher magnetic fields there exist no magnetic domains anymore.

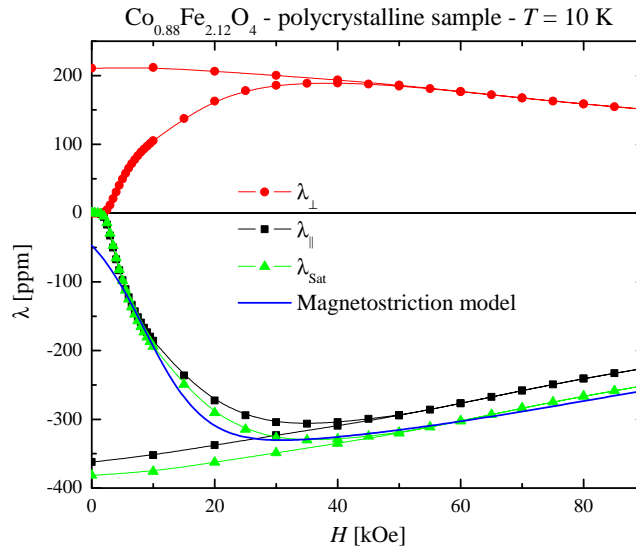


Figure 6.43: Saturation magnetostriction of “HT2” at $T = 10$ K plotted as function of the magnetic field. The solid blue line represents the fit with the magnetostriction model according to formula 4.10.

Table 6.10: Fit parameter according to formula 4.10 for describing the saturation magnetostriction measurements $\lambda_{sat}(H)$ on polycrystalline cobalt ferrite samples “HT2” and “HT2B”.

T [K]	$\lambda_1 = \frac{2\lambda_{100}}{5}$ [ppm]	c_1 [10^{-6} T^{-1}]	H_1 [T]	$\lambda_2 = \frac{3\lambda_{111}}{5}$ [ppm]	c_2 [10^{-6} T^{-1}]	H_2 [T]	τ [10^{-6} T^{-1}]	λ_{100} [ppm]	λ_{111} [ppm]
10	-360	2	0.85	160	0.36	8.1	1	-900	266.67
50	-375	2	1	160	0.52	6	1	-937.5	266.67
100	-375	3.5	0.85	160	0.51	6.4	1	-937.5	266.67
150	-310	6	0.4	140	0.71	5.15	1	-775	233.33
200	-300	7	0.25	145	0.82	3	1	-750	241.67
250	-255	10	0.12	135	0.9	2	1	-637.5	225
300	-207.28	18.22	0.17	100.19	0.97	0.97	1	-518.2	166.98
4.2	-380	1.5	1.5	250	0.3	8	0	-950	416.67
150	-303	5	0.5	173	0.69	5	0	-757.5	288.33
300	-157	20	0.1	77	1.5	1.5	0	-392.5	128.33

6.3.3 Remanent Magnetostriction

The main origin of the remanent magnetostriction λ_{rem} in the sample are irreversible domain configurations. It was shown in the previous chapter that only the easy axis magnetostriction constant λ_{100} contributes to λ_{rem} . In figure 6.44 the remanent magnetostriction of both polycrystalline samples are plotted as function of temperature. Additionally the difference of the indirect and direct magnetostriction measurements of λ_{100} of the single crystal is plotted as well. In table 6.12 all remanent magnetostriction constants together with the calculated difference of both single crystal λ_{100} measurements are listed up. The magnetostriction data for $T = 50, 150$ and 225 K are put in brackets, as they were interpolated in order to have data points for a further calculation. It is remarkable that only the difference of the directly and indirectly measured easy axis magnetostriction constants λ_{100} can be accounted for the remanent magnetostriction of the polycrystalline samples, as can be seen in figure 6.44.

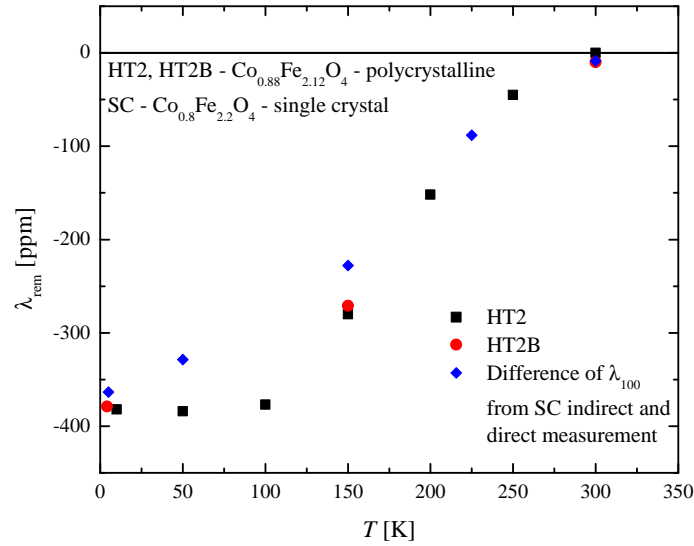


Figure 6.44: Remanent magnetostriction λ_{rem} of polycrystalline samples together with the difference of the directly and indirectly measured magnetostriction constant λ_{100} of the single crystal.

Table 6.11: Remanent magnetostriction λ_{rem} of polycrystalline cobalt ferrite samples “HT2” and “HT2B” and calculated difference of direct and indirect λ_{100} measurement on the single crystal.

T [K]	λ_{rem} HT2 [ppm]	λ_{rem} HT2B [ppm]	λ_{100} indirect [ppm]	λ_{100} direct [ppm]	difference [ppm]
4.2		-379	-913.6	-550	-363.6
10	-382				
50	-384		-875.2	(-546.5)	-328.7
100	-377			-550	
150	-280	-271	-749.6	(-521.9)	-227.7
200	-152			-500.7	
225			-565.6	(-477.5)	-88.1
250	-45				
300	0	-10	-424.8	-416.2	-8.6

6.3.4 Magneto-elastic Hysteresis

As the applied magnetic field was reversed for magnetostriction measurements on the polycrystalline “HT2B” sample, the magneto-elastic hysteresis was determined as well. In figure 6.40 the longitudinal and transversal magnetostriction is shown. The enclosed areas of these hysteresis loops were calculated as they are correlated with the magnetic hysteresis.

When calculating the area of a magnetization hysteresis loop, the result is an energy density [$\frac{J}{m^3}$]. This area corresponds to the magnetic losses of the sample which appear running through the hysteresis loop. These losses are caused by the movement of magnetic domains and domain walls. When integrating the magnetostriction hysteresis loop the resulting units do not form an energy density, as the magnetostriction is a relative measurement with unit of 1. It is therefore not possible to correlate these two kinds of hysteresis loops in a simple way. Although the origin of both hysteresis loops is the same: irreversible magnetic domain and domain wall movement of the easy [100] axis.

However one might try to separate the total hysteresis obtained from

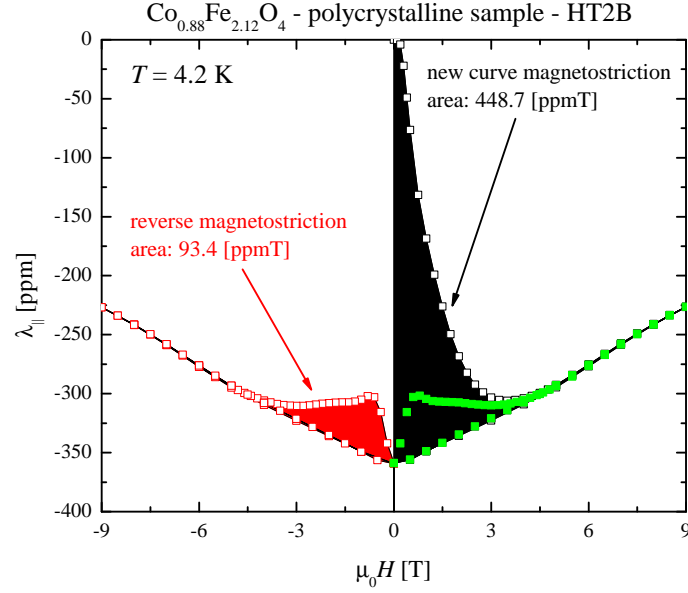


Figure 6.45: Longitudinal magnetostriction $\lambda_{||}$ at $T = 4.2$ K of “HT2B” together with the two enclosed areas.

magnetization measurement into two parts: $\int M dH = P_{Hyst} + P_{me}$. The first part P_{Hyst} comprises the microstructural and anisotropy determined part of the losses, while the second part $P_{me} = c \int \lambda dH$ stands for the magnetoelastic hysteresis contributions. The constant c describes the coupling parameter of the magnetoelastic losses to the magnetization state of the sample.

In figure 6.45 the longitudinal magnetostriction measurement of “HT2B” at $T = 4.2$ K is plotted. The black area shows the magneto-elastic loss of the initial or new curve $A_{||n.c.}$ (or $A_{\perp n.c.}$ for the transverse magnetostriction

Table 6.12: Magneto-elastic losses of magnetostriction measurements on the polycrystalline cobalt ferrite sample “HT2B”.

T [K]	$A_{ }$ [ppm T]	$A_{ n.c.}$ [ppm T]	A_{\perp} [ppm T]	$A_{\perp n.c.}$ [ppm T]	$M \cdot H$ [$\frac{\text{kJ}}{\text{m}^3}$]
4.2	93.4	448.76	91.42	301.58	938.1
150	91.9	148.23	94.87	126.94	345.4
300	3.71	30.02	-6.39	-26.92	52.6

measurement), whereas the red area represents the “normal” magneto-elastic hysteresis loss A_{\parallel} (or A_{\perp} for the transverse magnetostriction measurement). In table 6.12 the magneto-elastic losses together with the integrated magnetization area are shown for all three measured temperatures. The magneto-elastic losses parallel A_{\parallel} and perpendicular A_{\perp} to the magnetic field are the same within the measurement error. The discrepancy in the new curve losses $A_{\parallel n.c.}$ and $A_{\perp n.c.}$ comes from the different magnitude of the magnetostriction signal parallel and perpendicular to the magnetic field. Summing up, it was tried to find an explanation for the magnetostrictive hysteresis behavior of polycrystalline cobalt ferrite. Moreover by introducing the mean anisotropy field a parameter was found for describing the maximum field necessary to overcome the magneto-elastic losses of the new curve, as shown in figures 6.41 and 6.42.

6.3.5 Magnetostriction Constants

In figure 6.46 the two cubic magnetostriction constants λ_{100} and λ_{111} for all measured samples are plotted as function of the temperature. It is remarkable that the magnetostriction constants are all nearly the same, although the elemental composition of the polycrystalline and the single crystal are slightly different. Moreover all magnetostriction measurements follow the same trend in their temperature dependence.

Summing up it is possible to determine λ_{111} and λ_{100} correctly from one single magnetostriction measurement $\lambda_{Sat}(H)$ of a polycrystalline sample. As the anisotropy and the resulting anisotropy field at lower temperature ($T < 150$ K) is strongly increasing, no saturation at a maximum applied field of $H = 90$ kOe can be obtained and therefore no correct value for λ_{111} can be experimentally determined. Only with the help of the magnetostriction model and the therein considered magnetocrystalline anisotropy it is possible to extrapolate to the correct value of λ_{111} .

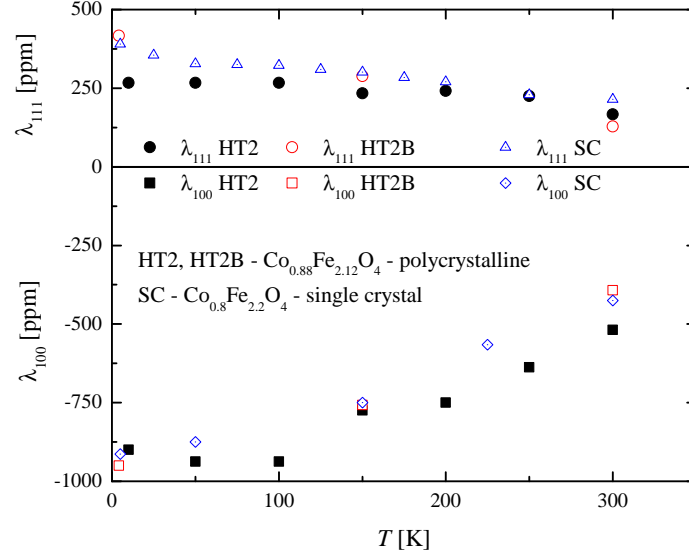


Figure 6.46: Magnetostriction constants λ_{100} and λ_{111} as function of temperature for all measured cobalt ferrite samples.

6.3.6 Discussion on Origin of Magnetostriction in Cobalt Ferrite

In magnetostriction measurements a general increase of λ_{100} and λ_{111} for of Co doped Magnetite $\text{Co}_x\text{Fe}_{3-x}\text{O}_4$ with respect to the Co concentration x is found [94, 95, 96]. In figures 6.47 and 6.48 the evolution of the magnetostriction constants with increasing Co content x is shown. While our measurement ($x = 0.8$) of $\lambda_{100}(x)$ fits with literature data [96], $\lambda_{111}(x)$ does not fit. For $x = 0.4$ and 0.6 a magnetic field of only 23 kOe was employed which can only saturate the easy [100] axis, but introduces large errors in the calculated values of λ_{111} , as Leyman and co-workers state themselves [96]. So a rather large error bar for these datapoints should be considered.

Nevertheless a maximum in both magnetostriction constants was found for cobalt ferrite $\text{Co}_x\text{Fe}_{3-x}\text{O}_4$ around $x = 0.7$, which made it interesting for more intense investigations [10, 22, 97]. Several production routes and their influence on the microstructure, magnetic properties and magnetostriction

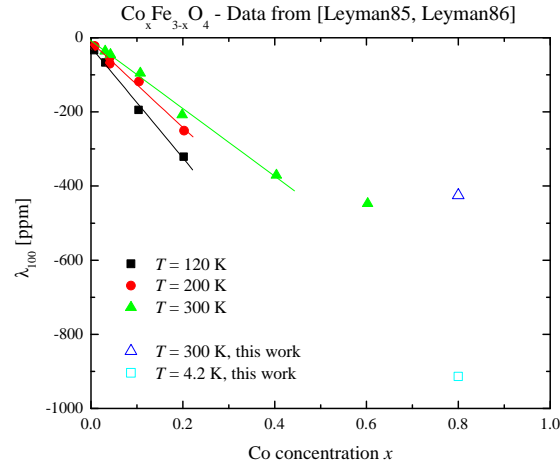


Figure 6.47: Evolution of λ_{100} magnetostriction constant with increasing Co content x . Data for $x \leq 0.6$ digitized from [96] and measured for $x = 0.8$ (see chapter 6.3).

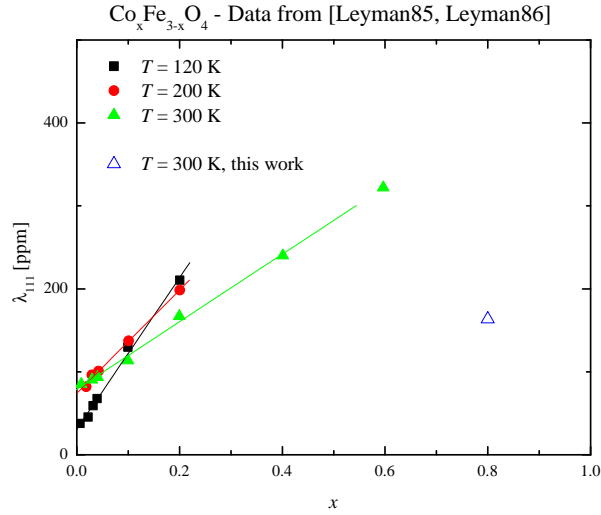


Figure 6.48: Evolution of λ_{111} magnetostriction constant with increasing Co content x . Data for $x \leq 0.6$ digitized from [96] and measured for $x = 0.8$ (see chapter 6.3).

were investigated in numerous publications and the references therein [62, 14, 25].

Although the crystal structure of cobalt ferrite is reported as cubic (as it is within this thesis), high resolution XRD measurements revealed a tetragonal distortion with a $\frac{c}{a}$ -ratio of 0.9988 at $T = 80$ K [98]. Recent synchrotron investigations [99] confirmed this tetragonal distortion and set the $\frac{c}{a}$ -ratio to 0.9989 at $T = 150$ K. No structural transition at either of these temperatures or even in the whole temperature range below the Curie-Temperature (4.2 to 780 K) occurs, as no indication in specific heat or magnetization measurements are ever reported.

The reason for this possible uncertainty in crystal structure is quite simple: Above the Curie-Temperature T_C the sample is paramagnetic and crystallizes in a real cubic crystal structure. Below T_C an increase of the exchange interaction occurs which creates in this case ferrimagnetic ordering. Another consequence is a slight deformation of the lattice due to the coupling of the magnetization vector to the lattice which is also known as magnetostriction. As magnetization and the resulting magnetostriction are increasing with decreasing temperature, the distortion of the cubic lattice can only be seen at low temperatures ($T = 80$ K) [98]. The typical resolution limit of conventional XRD is about $5 \cdot 10^{-3}$ while with synchrotron radiation a limit of $5 \cdot 10^{-4}$ can be achieved, which made it possible to see the lattice distortion even at higher temperatures of $T = 150$ K [99]. As cobalt ferrite has a considerably high magnetostriction at low temperatures ($\lambda_{100} \sim -1000$ ppm at $T = 4.2$ K), it is possible to observe the lattice deformation directly in XRD or synchrotron measurements.

Dionne found by elastic energy considerations that Co^{2+} ions in an octahedral environment favour an overall tetragonal distortion with $\frac{c}{a}$ -ratio < 1 [100, 101]. Moreover this leads to enhanced negative magnetostriction along [100] axis, which is also confirmed by [102].

It is of course important in any theoretical calculation to consider this lowering of symmetry. In a very recent publication an ab-initio calculation of the dependence of symmetry on the degree of inversion for cobalt and nickel ferrite was performed [103]. It was shown only by elastic and magnetoelastic considerations that the crystal symmetry depends on the cation distribution

and the degree of inversion. Moreover it was found that complete inversion is energetically most favorable for cobalt ferrite, because the resulting lowered symmetry is reducing the elastic energy of the system.

Chapter 7

Conclusion

The aim of this thesis was the study of the magnetic and magneto-elastic properties of cobalt ferrite. First, magnetization and then magnetostriction was measured as function of temperature and magnetic field for one single crystal and two polycrystalline samples. The cubic cobalt ferrite shows a magnetic easy [100], intermediate [110] and hard [111] axis.

The magnetization measurement along the crystallographic [111] axis shows a first order magnetization process (FOMP). This FOMP manifests itself as a jump at the critical FOMP field $H_{FOMP} = 55 \text{ kOe}$ below $T = 150 \text{ K}$. In order to describe the FOMP, the magnetic theory of a first order magnetization process was investigated and further developed. With this enhanced theoretical description it was not only possible to describe magnetization $M(H)$ as function of the applied magnetic field H , but also to determine the magnetic anisotropy constants K_1 and K_2 . For the first time, the dependence of the critical FOMP field H_{FOMP} and the height of the jump in the magnetization were calculated based on the first two anisotropy constants $K_1(T)$ and $K_2(T)$.

Moreover the magnetic anisotropy constants $K_1(T)$ and $K_2(T)$ were determined by two independent methods over a broad temperature range [10 - 400 K]. $K_2(T)$ was determined for the first time as function of temperature. As K_2 is regarded to be very small and therefore negligible at room temperature, no previous attempts can be found to measure it at lower

temperatures. At $T < 150$ K K_2 however starts to rise and exceeds K_1 by a factor of -2 . So at lower temperatures K_2 is playing a very dominant role in the magnetic anisotropy and the magnetization process.

This FOMP also influences the magneto-elastic properties. It becomes visible as a huge jump in the magnetostriction at the same critical FOMP field along the $[111]$ axis. Along the easy $[100]$ axis remanent magnetostriction was found over the whole measured temperature range $[4.2 - 300$ K], which manifests itself in the magnetostriction of the polycrystalline sample as well. A special measurement routine was developed to consider remanent magnetostriction. A model for describing magnetostriction measurements as function of the applied external magnetic field was developed, which incorporates magnetic anisotropy. With the help of that model it is possible to determine the magnetostriction constants λ_{100} and λ_{111} together with the magnetic anisotropy from one magnetostriction measurement of a cubic, polycrystalline material. For the first time the two magnetostriction constants λ_{100} and λ_{111} of cobalt ferrite were measured over a broad temperature $[4.2 - 300$ K] and field range $[0 - 90$ kOe].

Protective note

The copying, distribution and utilisation of this dissertation as well as the communication of its contents to others without expressed authorisation is prohibited. Offenders will be held liable for the payment of damages. All rights reserved in the event of the grant of a patent, Utility model or ornamental design registration.

Schutzvermerk

Weitergabe sowie Vervielfältigung dieser Dissertation, Verwertung und Mitteilung ihres Inhalts sind verboten, soweit nicht ausdrücklich gestattet. Zuwiderhandlungen verpflichten zu Schadenersatz. Alle Rechte für den Fall der Patent-, Gebrauchsmuster- oder Geschmacksmustereintragung vorbehalten.

Bibliography

- [1] P. Mohn. *Magnetism in the Solid State: An Introduction*. Springer Series in Solid-State Sciences, Springer. ISBN 9783540293842 (2005), URL <http://books.google.at/books?id=BWVvii4WuE4C>
- [2] J. Smit, H. P. J. Wijn. *Ferrite: Die physikalischen Eigenschaften von Ferrimagnetischen Oxyden unter besonderer Berücksichtigung ihrer technischen Anwendung*. N. V. Philips' Gloeilampenfabrieken, Eindhoven (Holland) (1962)
- [3] R. Becker, W. Döring. *Ferromagnetismus*. Springer Verlag Berlin (1939)
- [4] R. Valenzuela. *Magnetic Ceramics*. Cambridge University Press, Cambridge. ISBN 9780511600296 (ebook) (1994), URL <http://dx.doi.org/10.1017/CB09780511600296>
- [5] S. Hilpert. *Genetische und konstitutive Zusammenhänge in den magnetischen Eigenschaften bei Ferriten und Eisenoxyden*. Berichte der deutschen chemischen Gesellschaft **42**, 2, pp. 2248–2261. ISSN 03659496 (1909), URL <http://doi.wiley.com/10.1002/cber.190904202121>
- [6] L. Néel. *Propriétés magnétiques des ferrites. Ferrimagnétisme et antiferromagnétisme*. Ann. Phys. **3**, pp. 137–198 (1948)
- [7] C. Shull, W. Strauser, E. Wollan. *Neutron Diffraction by Paramagnetic and Antiferromagnetic Substances*. Physical Review

- 83**, 2, pp. 333–345. ISSN 0031-899X (1951), URL
<http://link.aps.org/doi/10.1103/PhysRev.83.333>
- [8] R. Bozorth, J. Walker. *Magnetostriction of Single Crystals of Cobalt and Nickel Ferrites*. Physical Review **88**, 5, p. 1209–1209. ISSN 0031-899X (1952), URL
<http://link.aps.org/doi/10.1103/PhysRev.88.1209>
- [9] C. Guillaud. *Elementary Mechanisms of Magnetization in Mixed Oxides of Iron and Cobalt*. Reviews of Modern Physics **25**, 1, pp. 64–73. ISSN 0034-6861 (1953), URL
<http://link.aps.org/doi/10.1103/RevModPhys.25.64>
- [10] R. Bozorth, E. Tilden, A. Williams. *Anisotropy and Magnetostriction of Some Ferrites*. Physical Review **99**, 6, p. 1788–1798. ISSN 0031-899X (1955), URL
<http://link.aps.org/doi/10.1103/PhysRev.99.1788>
- [11] S. Foner. *Vibrating Sample Magnetometer*. Review of Scientific Instruments **27**, 7, p. 548. ISSN 00346748 (1956), URL
<http://link.aip.org/link/?RSI/27/548/1&Agg=doi>
- [12] S. Foner, J. O. Artman. *Magnetization Processes in Heat-Treated Single Crystal Cobalt Ferrite*. Journal of Applied Physics **29**, 3, p. 443. ISSN 00218979 (1958), URL
<http://link.aip.org/link/JAPIAU/v29/i3/p443/s1&Agg=doi>
- [13] S. Iida, H. Sekizawa, Y. Aiyama. *Origin of the Uniaxial Anisotropy in Iron-Cobalt Ferrites*. Journal of the Physical Society of Japan **10**, 10, p. 907–907. ISSN 0031-9015 (1955), URL
<http://jpsj.ipap.jp/link?JPSJ/10/907/>
- [14] A. Muhammad, R. Sato-Turtelli, M. Kriegisch, R. Grössinger, F. Kubel, T. Konegger. *Large enhancement of magnetostriction due to compaction hydrostatic pressure and magnetic annealing in CoFe_2O_4* . Journal of Applied Physics **111**, 1, p. 013918. ISSN 00218979 (2012), URL
<http://link.aip.org/link/JAPIAU/v111/i1/p013918/s1&Agg=doi>

- [15] H. J. Williams, R. D. Heidenreich, E. A. Nesbitt. *Mechanism by Which Cobalt Ferrite Heat Treats in a Magnetic Field*. Journal of Applied Physics **27**, 1, p. 85. ISSN 00218979 (1956), URL <http://link.aip.org/link/JAPIAU/v27/i1/p85/s1&Agg=doi>
- [16] R. Penoyer, L. Bickford. *Magnetic Annealing Effect in Cobalt-Substituted Magnetite Single Crystals*. Physical Review **108**, 2, p. 271–277. ISSN 0031-899X (1957), URL <http://link.aps.org/doi/10.1103/PhysRev.108.271>
- [17] J. Slonczewski. *Origin of Magnetic Anisotropy in Cobalt-Substituted Magnetite*. Physical Review **110**, 6, p. 1341–1348. ISSN 0031-899X (1958), URL <http://link.aps.org/doi/10.1103/PhysRev.110.1341>
- [18] P. Tannenwald. *Multiple Resonances in Cobalt Ferrite*. Physical Review **99**, 2, p. 463–464. ISSN 0031-899X (1955), URL <http://link.aps.org/doi/10.1103/PhysRev.99.463>
- [19] H. Shenker. *Magnetic Anisotropy of Cobalt Ferrite ($\text{Co}_{1.01}\text{Fe}_{2.00}\text{O}_{3.62}$) and Nickel Cobalt Ferrite ($\text{Ni}_{0.72}\text{Fe}_{0.20}\text{Co}_{0.08}\text{Fe}_2\text{O}_4$)*. Physical Review **107**, 5, p. 1246–1249. ISSN 0031-899X (1957), URL <http://link.aps.org/doi/10.1103/PhysRev.107.1246>
- [20] R. Perthel, G. Elbinger, W. Keilig. *Über die Anisotropie des magnetischen Momentes und die Kristallanisotropie bei Kobaltferrit*. physica status solidi (b) **17**, 1, p. 151–154. ISSN 03701972 (1966), URL <http://doi.wiley.com/10.1002/pssb.19660170119>
- [21] J. C. Slonczewski. *Anisotropy and Magnetostriction in Magnetic Oxides*. Journal of Applied Physics **32**, 3, p. S253. ISSN 00218979 (1961), URL <http://link.aip.org/link/JAPIAU/v32/i3/pS253/s1&Agg=doi>
- [22] K. P. Belov, A. N. Goryaga, A. N. Lyamzin. *Anomalous magnetic properties of CoFe_2O_4 ferrite*. Sov. Phys. Solid State (English Transl.) **31**, 2, p. 191 (1989)

- [23] S. D. Bhame, P. A. Joy. *Magnetic and magnetostrictive properties of manganese substituted cobalt ferrite*. Journal of Physics D: Applied Physics **40**, 11, pp. 3263–3267. ISSN 0022-3727 (2007), URL <http://stacks.iop.org/0022-3727/40/i=11/a=001?key=crossref.1c13511747924830639b54e152f1032f>
- [24] I. Nlebedim, N. Ranvah, Y. Melikhov, P. Williams, J. Snyder, A. Moses, D. Jiles. *Magnetic and Magnetomechanical Properties of $\text{CoAl}_x\text{Fe}_{2-x}\text{O}_4$ for Stress Sensor and Actuator Applications*. IEEE Transactions on Magnetics **45**, 10, pp. 4120–4123. ISSN 0018-9464 (2009), URL <http://ieeexplore.ieee.org/lpdocs/epic03/wrapper.htm?arnumber=5257208>
- [25] I. Nlebedim, J. Snyder, A. Moses, D. Jiles. *Dependence of the magnetic and magnetoelastic properties of cobalt ferrite on processing parameters*. Journal of Magnetism and Magnetic Materials **322**, 24, p. 3938–3942. ISSN 03048853 (2010), URL <http://linkinghub.elsevier.com/retrieve/pii/S0304885310005615>
- [26] M. Guillot, J. Ostorero, A. Marchand. *High magnetic field magnetization study in cadmium-cobalt ferrite single crystals*. Zeitschrift für Physik B Condensed Matter **71**, 2, p. 193–197. ISSN 0722-3277 (1988), URL <http://www.springerlink.com/index/10.1007/BF01312789>
- [27] S. Foner. *Versatile and Sensitive Vibrating-Sample Magnetometer*. Review of Scientific Instruments **30**, 7, p. 548. ISSN 00346748 (1959), URL <http://link.aip.org/link/RSINAK/v30/i7/p548/s1&Agg=doi>
- [28] S. Chikazumi, C. D. Graham. *Physics of ferromagnetism*. Oxford University Press, Oxford. ISBN 0198517769 (1997), URL <http://lccn.loc.gov/96027148>
- [29] T. Holstein. *Field Dependence of the Intrinsic Domain Magnetization of a Ferromagnet*. Physical Review **58**, 12, p. 1098–1113. ISSN

- 0031-899X (1940), URL
<http://link.aps.org/doi/10.1103/PhysRev.58.1098>
- [30] W. Brown. *Theory of the Approach to Magnetic Saturation*. Physical Review **58**, 8, p. 736–743. ISSN 0031-899X (1940), URL
<http://link.aps.org/doi/10.1103/PhysRev.58.736>
- [31] A. Kihal, G. Fillion, B. Bouzabata, B. Barbara. *High field surface magnetic study of Fe_3O_4 nanoparticles*. physica status solidi (b) **249**, 3, p. 604–614. ISSN 03701972 (2012), URL
<http://doi.wiley.com/10.1002/pssb.201147412>
- [32] N. S. Akulov. *Über den Verlauf der Magnetisierungskurve in starken Feldern*. Zeitschrift für Physik **69**, 11-12, p. 822–831. ISSN 1434-6001 (1931), URL
<http://www.springerlink.com/index/10.1007/BF01339465>
- [33] F. Bloch. *Zur Theorie des Ferromagnetismus*. Zeitschrift für Physik **61**, 3-4, p. 206–219. ISSN 1434-6001 (1930), URL
<http://www.springerlink.com/index/10.1007/BF01339661>
- [34] H. Polley. *Das Einmünden der Magnetisierung in die Sättigung bei Nickel zwischen + 135° C und -25° C. Temperaturabhängigkeit der Kristallenergie*. Annalen der Physik **428**, 7, p. 625–650. ISSN 00033804 (1939), URL
<http://doi.wiley.com/10.1002/andp.19394280705>
- [35] J. Hopkinson. *Magnetic and Other Physical Properties of Iron at a High Temperature*. Philosophical Transactions of the Royal Society A: Mathematical, Physical and Engineering Sciences **180**, 0, p. 443–465. ISSN 1364-503X (1889), URL <http://rsta.royalsocietypublishing.org/cgi/doi/10.1098/rsta.1889.0014>
- [36] P. Weiss. *L'hypothèse du champ moléculaire et la propriété ferromagnétique*. J. de Phys. **6**, p. 661–690 (1907)
- [37] A. R. Kaufmann. Phys. Rev. **55**, p. 1142 (1939)

- [38] M. R. D. Guire, R. C. O'Handley, G. Kalonji. *The cooling rate dependence of cation distributions in CoFe_2O_4* . Journal of Applied Physics **65**, 8, p. 3167. ISSN 00218979 (1989), URL <http://link.aip.org/link/JAPIAU/v65/i8/p3167/s1&Agg=doi>
- [39] S. Blundell. *Magnetism in condensed matter*. Oxford University Press, Oxford. ISBN 0198505914 (pbk.) (2001)
- [40] R. D. Shannon. *Revised effective ionic radii and systematic studies of interatomic distances in halides and chalcogenides*. Acta Crystallographica Section A **32**, 5, p. 751–767. ISSN 0567-7394 (1976), URL <http://scripts.iucr.org/cgi-bin/paper?S0567739476001551>
- [41] G. A. Sawatzky. *Cation Distributions in Octahedral and Tetrahedral Sites of the Ferrimagnetic Spinel CoFe_2O_4* . Journal of Applied Physics **39**, 2, p. 1204. ISSN 00218979 (1968), URL <http://link.aip.org/link/JAPIAU/v39/i2/p1204/s1&Agg=doi>
- [42] R. Piety. *Ferromagnetic Anisotropy of Iron Crystals at Various Temperatures*. Physical Review **50**, 12, p. 1173–1177. ISSN 0031-899X (1936), URL <http://link.aps.org/doi/10.1103/PhysRev.50.1173>
- [43] K. H. Stewart. *Ferromagnetic Domains*. Cambridge University Press (1954)
- [44] R. Bozorth. *Determination of Ferromagnetic Anisotropy in Single Crystals and in Polycrystalline Sheets*. Physical Review **50**, 11, p. 1076–1081. ISSN 0031-899X (1936), URL <http://link.aps.org/doi/10.1103/PhysRev.50.1076>
- [45] G. Asti, F. Bolzoni. *Irreversible rotation processes in uniaxial ferromagnetic crystals*. Journal of Applied Physics **50**, B11, p. 7725. ISSN 00218979 (1979), URL <http://link.aip.org/link/JAPIAU/v50/iB11/p7725/s2&Agg=doi>

- [46] A. Hubert, R. Schäfer. *Magnetic Domains: The Analysis of Magnetic Microstructures*. Springer Berlin Heidelberg. ISBN 978-3540641087 (1998)
- [47] A. S. Lagutin, A. V. Dmitriev. Sov. Phys. Solid State (English Transl.) **30**, p. 1705 (1988)
- [48] V. G. Bar'yakhtar, V. A. Borodin, V. D. Doroshev, N. M. Kovtun, R. Z. Levitin, E. P. Stefanovskii. *Experimental and theoretical investigation of spin-reorientation phase transitions in cubic ferromagnets and ferrimagnets in a magnetic field*. Journal of Experimental and Theoretical Physics **47**, p. 315 (1978), URL <http://www.jetp.ac.ru/cgi-bin/e/index/e/47/2/p315?a=list>
- [49] H. Takaki, Y. Nakamura. *The Magnetostriction Constants of Silicon Steel (I)*. Journal of the Physical Society of Japan **9**, 4, pp. 507–511. ISSN 0031-9015 (1954), URL <http://jpsj.ipap.jp/link?JPSJ/9/507/>
- [50] K. Honda, S. Kaya, Y. Masuyama. *On the Magnetic Properties of Single Crystals of Iron*. Nature **117**, 2952, pp. 753–754. ISSN 0028-0836 (1926), URL <http://www.nature.com/doifinder/10.1038/117753a0>
- [51] R. Gans, E. Czerlinski. Schr. Königsberg. gel. Ges., Naturwiss. Kl. **9**, p. 1 (1932)
- [52] R. Gans, E. Czerlinski. *Theory of magnetization curve of ferromagnetic single crystals*. Ann. Phys. **16**, pp. 625 – 635 (1933)
- [53] A. Aharoni. *Demagnetizing factors for rectangular ferromagnetic prisms*. Journal of Applied Physics **83**, 6, p. 3432. ISSN 00218979 (1998), URL <http://link.aip.org/link/JAPIAU/v83/i6/p3432/s1&Agg=doi>
- [54] A. del Moral. *Magnetostriction and Magnetostrictive Materials*. Del Moral Publisher. ISBN 978-84-612-0656-8 (2004)

- [55] A. Bienkowski, J. Kulikowski. *The dependence of Villari effect in ferrites on their magnetocrystalline properties and magnetostriction*. Journal of Magnetism and Magnetic Materials **26**, 1-3, p. 292–294. ISSN 03048853 (1982), URL <http://linkinghub.elsevier.com/retrieve/pii/0304885382901755>
- [56] D. C. Jiles, D. L. Atherton. *Theory of ferromagnetic hysteresis (invited)*. Journal of Applied Physics **55**, 6, p. 2115. ISSN 00218979 (1984), URL <http://link.aip.org/link/JAPIAU/v55/i6/p2115/s1&Agg=doi>
- [57] M. Sablik, D. Jiles. *Coupled magnetoelastic theory of magnetic and magnetostrictive hysteresis*. IEEE Transactions on Magnetics **29**, 4, p. 2113–2123. ISSN 00189464 (1993), URL <http://ieeexplore.ieee.org/lpdocs/epic03/wrapper.htm?arnumber=221036>
- [58] M. Rotter, H. Müller, E. Gratz, M. Doerr, M. Loewenhaupt. *A miniature capacitance dilatometer for thermal expansion and magnetostriction*. Review of Scientific Instruments **69**, 7, p. 2742. ISSN 00346748 (1998), URL <http://link.aip.org/link/RSINAK/v69/i7/p2742/s1&Agg=doi>
- [59] R. Becker, H. Polley. *Der Einfluß innerer Spannungen auf das Einmündungsgesetz bei Nickel*. Annalen der Physik **429**, 7, p. 534–540. ISSN 00033804 (1940), URL <http://doi.wiley.com/10.1002/andp.19404290705>
- [60] W. Wang, X. Ren. *Flux growth of high-quality CoFe_2O_4 single crystals and their characterization*. Journal of Crystal Growth **289**, 2, p. 605–608. ISSN 00220248 (2006), URL <http://linkinghub.elsevier.com/retrieve/pii/S0022024805014302>
- [61] D. B. Williams, C. B. Carter. *Transmission Electron Microscopy*. Springer, 2009 edition. ISBN 0387765026 (2009)
- [62] A. Muhammad. *Development and Investigation of New Magnetoelectric Composites*. Ph.D. thesis, Vienna University of Technology, Vienna (2011)

- [63] E. W. Pugh, B. E. Argyle. *Pyromagnetic Test of Spin Wave Theory in Metallic Nickel*. Journal of Applied Physics **33**, 3, p. 1178. ISSN 00218979 (1962), URL <http://link.aip.org/link/JAPIAU/v33/i3/p1178/s1&Agg=doi>
- [64] A. Franco, F. L. A. Machado, V. S. Zapf. *Magnetic properties of nanoparticles of cobalt ferrite at high magnetic field*. Journal of Applied Physics **110**, 5, p. 053913. ISSN 00218979 (2011), URL <http://link.aip.org/link/JAPIAU/v110/i5/p053913/s1&Agg=doi>
- [65] M. Kriegisch, W. Ren, R. Sato-Turtelli, H. Müller, R. Grössinger, Z. Zhang. *Field-induced magnetic transition in cobalt-ferrite*. Journal of Applied Physics **111**, 7, p. 07E308. ISSN 00218979 (2012), URL <http://link.aip.org/link/JAPIAU/v111/i7/p07E308/s1&Agg=doi>
- [66] J. Hopkinson. *Magnetic Properties of Alloys of Nickel and Iron*. Proceedings of the Royal Physical Society **48**, 0, p. 1–13 (1890), URL <http://www.jstor.org/stable/114967>
- [67] A. Arrott. *Criterion for Ferromagnetism from Observations of Magnetic Isotherms*. Physical Review **108**, 6, p. 1394–1396. ISSN 0031-899X (1957), URL <http://link.aps.org/doi/10.1103/PhysRev.108.1394>
- [68] K. P. Belov. *Magnetic Transitions*. Boston Technical Publishers, USA (1965)
- [69] B. M. Moskowitz. *High-Temperature Magnetostriction of Magnetite and Titanomagnetites*. Journal of Geophysical Research **98**, B1, pp. 359–371 (1993)
- [70] M. K. Fayek, A. A. Bahgat. *Fe57 Mössbauer study in cobalt substituted magnetite*. Zeitschrift für Physik B Condensed Matter **46**, 3, p. 199–205. ISSN 0722-3277 (1982), URL <http://www.springerlink.com/index/10.1007/BF01360294>
- [71] R. Persoons, E. D. Grave, P. de Bakker, R. Vandenberghe. *Mössbauer study of the high-temperature phase of Co-substituted magnetites*,

- $Co_xFe_{3-x}O_4$, $x \geq 0.1$. Physical Review B **47**, 10, p. 5894–5905. ISSN 0163-1829 (1993), URL
<http://link.aps.org/doi/10.1103/PhysRevB.47.5894>
- [72] N. L. Brühkatov, L. V. Kirensky. *Anisotropy of magnetic energy in single crystals of Ni as a function of temperature*. Physik. Z. Sowjetunion **12**, pp. 602 – 609 (1937)
- [73] N. L. Brühkatov, L. V. Kirensky. *Influence of temperature on magnetic anisotropy energy of ferromagnetic crystals*. Tech. Phys. (USSR) **5**, pp. 171 – 183 (1937)
- [74] N. Akulov. *Zur Quantentheorie der Temperaturabhängigkeit der Magnetisierungskurve*. Zeitschrift für Physik **100**, 3-4, p. 197–202. ISSN 1434-6001 (1936), URL
<http://www.springerlink.com/index/10.1007/BF01418601>
- [75] C. Zener. *Classical Theory of the Temperature Dependence of Magnetic Anisotropy Energy*. Physical Review **96**, 5, p. 1335–1337. ISSN 0031-899X (1954), URL
<http://link.aps.org/doi/10.1103/PhysRev.96.1335>
- [76] K. Yosida, M. Tachiki. *On the Origin of the Magnetic Anisotropy Energy of Ferrites*. Progress of Theoretical Physics **17**, 3, p. 331–359. ISSN 0033-068X (1957), URL
<http://ptp.ipap.jp/link?PTP/17/331/>
- [77] A. Franco, F. C. e Silva. *High temperature magnetic properties of cobalt ferrite nanoparticles*. Applied Physics Letters **96**, 17, p. 172505. ISSN 00036951 (2010), URL
<http://link.aip.org/link/APPLAB/v96/i17/p172505/s1&Agg=doi>
- [78] A. Seeger. *Moderne Probleme der Metallphysik: Band 2: Chemische Bindung in Kristallen und Ferromagnetismus*. Springer Berlin Heidelberg New York. ISBN 978-3540036180 (1965), URL
<http://books.google.at/books?id=GlxAAAAIAAJ>

- [79] E. J. W. Verwey. *Electronic Conduction of Magnetite (Fe_3O_4) and its Transition Point at Low Temperatures*. Nature **144**, 3642, pp. 327–328. ISSN 0028-0836 (1939), URL <http://www.nature.com/doi/10.1038/144327b0>
- [80] L. Bickford. *The Low Temperature Transformation in Ferrites*. Reviews of Modern Physics **25**, 1, pp. 75–79. ISSN 0034-6861 (1953), URL <http://link.aps.org/doi/10.1103/RevModPhys.25.75>
- [81] W. Hamilton. *Neutron Diffraction Investigation of the 119° K Transition in Magnetite*. Physical Review **110**, 5, pp. 1050–1057. ISSN 0031-899X (1958), URL <http://link.aps.org/doi/10.1103/PhysRev.110.1050>
- [82] E. J. W. Verwey, E. L. Heilmann. *Physical Properties and Cation Arrangement of Oxides with Spinel Structures I. Cation Arrangement in Spinel*. The Journal of Chemical Physics **15**, 4, p. 174. ISSN 00219606 (1947), URL <http://link.aip.org/link/JCPSA6/v15/i4/p174/s1&Agg=doi>
- [83] E. J. Verwey, P. W. Haayman, F. C. Romeijn. *Physical Properties and Cation Arrangement of Oxides with Spinel Structures II. Electronic Conductivity*. The Journal of Chemical Physics **15**, 4, p. 181. ISSN 00219606 (1947), URL <http://link.aip.org/link/JCPSA6/v15/i4/p181/s1&Agg=doi>
- [84] G. Rado, J. Ferrari. *Electric field dependence of the magnetic anisotropy energy in magnetite (Fe_3O_4)*. Physical Review B **12**, 11, pp. 5166–5174. ISSN 0556-2805 (1975), URL <http://link.aps.org/doi/10.1103/PhysRevB.12.5166>
- [85] K. Siratori, E. Kita, G. Kaji, A. Tasaki, S. Kimura, I. Shindo, K. Kohn. *Magnetoelectric Effect of Fe_3O_4 at 77 K. I. Crystal Symmetry*. Journal of the Physical Society of Japan **47**, 6, pp. 1779–1787. ISSN 0031-9015 (1979), URL <http://jpsj.ipap.jp/link?JPSJ/47/1779/>

- [86] K. Kato, S. Iida. *Magnetoelectric Effects of Fe_3O_4 at 4.2 K*. Journal of the Physics Society Japan **50**, 9, pp. 2844–2850. ISSN 0031-9015 (1981), URL <http://jpsj.ipap.jp/link?JPSJ/50/2844/>
- [87] S. Chikazumi. *Current understanding of low temperature phase transition of magnetite, particularly in relation to the behavior of magnetocrystalline anisotropy*. In *AIP Conference Proceedings*, pp. 382–387 (1976), URL <http://link.aip.org/link/APCPCS/v29/i1/p382/s1&Agg=doi>
- [88] J. Yoshida, S. Iida. *X-Ray Diffraction Study on the Low Temperature Phase of Magnetite*. Journal of the Physical Society of Japan **42**, 1, pp. 230–237. ISSN 0031-9015 (1977), URL <http://jpsj.ipap.jp/link?JPSJ/42/230/>
- [89] G. S. Parks, K. K. Kelley. *The Heat Capacities of Some Metallic Oxides*. Journal of Physical Chemistry **30**, 1, pp. 47–55. ISSN 0022-3654 (1926), URL <http://pubs.acs.org/cgi-bin/doilookup/?10.1021/j150259a005>
- [90] P. Weiss, R. Forrer. *Absolute Saturation of Ferromagnetic Substances and the Law of Approach as a Function of the Field and of the Temperature*. Annalen der Physik **12**, 10, pp. 279 – 374 (1929), URL http://www.fischer-tropsch.org/Bureau_of_Mines/abs_of_lit/lit-abs/3600/lit3642.htm
- [91] L. Bickford, J. Pappis, J. Stull. *Magnetostriction and Permeability of Magnetite and Cobalt-Substituted Magnetite*. Physical Review **99**, 4, pp. 1210–1214. ISSN 0031-899X (1955), URL <http://link.aps.org/doi/10.1103/PhysRev.99.1210>
- [92] V. Brabers, F. Walz, H. Kronmüller. *Impurity effects upon the Verwey transition in magnetite*. Physical Review B **58**, 21, pp. 14163–14166. ISSN 0163-1829 (1998), URL <http://link.aps.org/doi/10.1103/PhysRevB.58.14163>
- [93] E. D. Grave, R. Leyman, R. Vanleerberghe. *The coordination of Co^{2+} ions in Co substituted magnetites $\text{Co}_x\text{Fe}_{3-x}\text{O}_4$ with $x \leq 0.04$* .

- Physics Letters A **97**, 8, p. 354–356. ISSN 03759601 (1983), URL <http://linkinghub.elsevier.com/retrieve/pii/037596018390662X>
- [94] R. Leyman, C. Henriët-Iserentant. *The effect of Co^{2+} on the Verwey transition of $\text{Co}_x\text{Fe}_{3-x}\text{O}_4$ ($x \leq 0.04$) single crystals*. Physics Letters A **99**, 4, p. 180–182. ISSN 03759601 (1983), URL <http://linkinghub.elsevier.com/retrieve/pii/0375960183909726>
- [95] R. Leyman. *Magnetostriction and anisotropy of $\text{Co}_x\text{Fe}_{3-x}\text{O}_4$ ($x \leq 0.1$) single crystals*. Journal of Magnetism and Magnetic Materials **49**, 3, p. 337–348. ISSN 03048853 (1985), URL <http://linkinghub.elsevier.com/retrieve/pii/0304885385901672>
- [96] R. Leyman, C. Henriët-Iserentant, R. Vandenberghe. *Magnetostriction and anisotropy of $\text{Co}_x\text{Fe}_{3-x}\text{O}_4$ ($0.005 \leq x \leq 0.6$) single crystals*. Journal of Magnetism and Magnetic Materials **54-57**, pp. 913–914. ISSN 03048853 (1986), URL <http://linkinghub.elsevier.com/retrieve/pii/0304885386903112>
- [97] K. P. Belov, A. N. Goryaga. *On low-temperature phase transitions in the CoFe_2O_4 and MnFe_2O_4 spinel ferrites*. Moscow University Physics Bulletin **48**, 1, pp. 108–114 (1993)
- [98] H. P. Rooksby, B. T. M. Willis. *Crystal Structure and Magnetic Properties of Cobalt Ferrite at Low Temperatures*. Nature **172**, 4388, p. 1054–1055. ISSN 0028-0836 (1953), URL <http://www.nature.com/doi/10.1038/1721054c0>
- [99] S. Yang, X. Ren. *Noncubic crystallographic symmetry of a cubic ferromagnet: Simultaneous structural change at the ferromagnetic transition*. Physical Review B **77**, 1. ISSN 1098-0121 (2008), URL <http://link.aps.org/doi/10.1103/PhysRevB.77.014407>
- [100] G. F. Dionne. *Origin of the magnetostriction effects from Mn^{3+} , Co^{2+} , and Fe^{2+} ions in ferrimagnetic spinels and garnets*. Journal of Applied Physics **50**, 6, p. 4263. ISSN 00218979 (1979), URL <http://link.aip.org/link/JAPIAU/v50/i6/p4263/s1&Agg=doi>

- [101] G. F. Dionne. *Theory of Co^{2+} exchange isolation in ferrimagnetic spinels and garnets*. Journal of Applied Physics **64**, 3, p. 1323. ISSN 00218979 (1988), URL <http://link.aip.org/link/JAPIAU/v64/i3/p1323/s1&Agg=doi>
- [102] N. Akers, A. Pointon. *The magnetostriction due to Co^{2+} ions in ferrites: The effect of excited states*. Journal of Magnetism and Magnetic Materials **15-18**, p. 547–548. ISSN 03048853 (1980), URL <http://linkinghub.elsevier.com/retrieve/pii/0304885380906575>
- [103] D. Fritsch, C. Ederer. *First-principles calculation of magnetoelastic coefficients and magnetostriction in the spinel ferrites CoFe_2O_4 and NiFe_2O_4* . Physical Review B **86**, 1. ISSN 1098-0121 (2012), URL <http://link.aps.org/doi/10.1103/PhysRevB.86.014406>

Curriculum Vitae

not available in online version!